Development of a microstructural model for braided medical stents

Tax, R.

Award date:
2021

Development of a microstructural model for braided medical stents

MSc Thesis

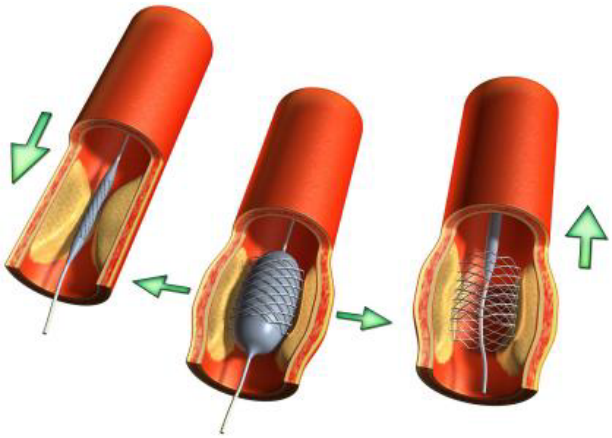

Master:	Mechanical Engineering
Research Group:	Mechanics of Materials

Student:	R. Tax
Student number:	0914930
Thesis supervisor:	O. Rokoš (TU/e)
Second supervisor:	R. Peerlings (TU/e)
	O. van der Sluis (TU/e and Philips)

Eindhoven, October 4, 2021

This report was made in accordance with the TU/e Code of Scientific Conduct for the Master thesis.

Preface

This document is my Master's thesis to complete the Master's degree in Mechanical engineering. The project is a collaboration between Philips Research and the Mechanics of Materials group of the Eindhoven University of Technology. A very interesting opportunity came along to help Philips with improving healthcare: the personalization of medical stent placement to restore the blood flow in clogged blood vessels. This intriguing use case really motivated me to contribute something to this field. This report describes the development and implementation of a numerical unit cell model of a braided stent.

I would like to thank my supervisors Ondrej Rokoš, Ron Peerlings, and Olaf van der Sluis for their support during the project. Their valuable feedback during the bi-weekly meetings certainly helped me moving forward throughout the project. A special thanks to Ondrej, who always took the time to review my work and help me with technical issues. I would also like to thank Philips scientists Rene Ubachs and Ruud Voncken for their valuable input during the project. Last but not least, I would like to thank my girlfriend, Ilse van Hulst, for her support and textual reviews of this thesis report.

Finally, I would like to thank Philips for providing a good work environment, despite the Covid-19 situation. Working twice a week on-site at the High Tech Campus together with other Master students, instead of alone at home, really added value to my experience of the project.

Eindhoven, October 2021

Rogier Tax

Abstract

Lots of development on computational models to predict the mechanical behaviour of braided stents, which are used to restore the blood flow in coronary arteries, has been reported in the literature. These models often rely on simplifying assumptions such as infinitely long geometry or ideally cylindrical shape of the blood vessel. Further, the most advanced models existing have a high computational time. When tailoring the care to a patient's needs, these limitations become an issue.

In this research, the possibility to capture the mechanical behaviour of a braided stent in a more computationally efficient manner, without compromising on accuracy, is studied. A multi-scale computational homogenization approach is considered, based on the previous work of Coenen, Geers, and Kouznetsova. This method relies on the fact that the microstructural features are much smaller than the overall dimensions of the stent. This study shows promising results on the homogenized properties of the representative volume element (RVE). Further work is required to prove whether a fully coupled FE^2 model, using shell elements at the macroscale, can capture all relevant stent mechanics.

The developed RVE is studied thoroughly to investigate the microstructural behaviour and verify the accuracy of existing beam models in the literature using more detailed, solid elements. In addition, the use of linear and non-linear material models is investigated, as is the use of a hinge or contact description at the wire crossings. The findings suggest that the beam models used in the literature, both for linear and non-linear material models, can accurately represent the mechanical behaviour of the stent, even in more complex load cases such as torsion, bending, and large diameter reductions. Using a hinge description at the wire crossings showed reduced performance compared to the contact model.

Contents

1 Introduction

1.1 Industrial relevance

With over a century of history in engineering and over ninety years of experience in medical systems and healthcare, Royal Philips is one of the leading innovators in the field of medical products and services. Philips' main focus is to create meaningful solutions to increase the quality of patient care. Among these solutions, there is a focus on the so-called 'personalized medicine' applications, which aim to tailor medical interventions to a patient's needs. Current research in this field aims to personalize stent placement interventions.

Stent placement to restore the opening of the blood vessel after clogging is one of the most performed interventions worldwide. In the Netherlands alone, approximately 35,000 stents are placed every year [11]. The stent placement procedure is performed using a catheter in combination with an inflatable balloon, or using a catheter and self-expanding stent. The latter type of procedure, as shown in Figure 1.1, applies to the stents studied in this thesis.

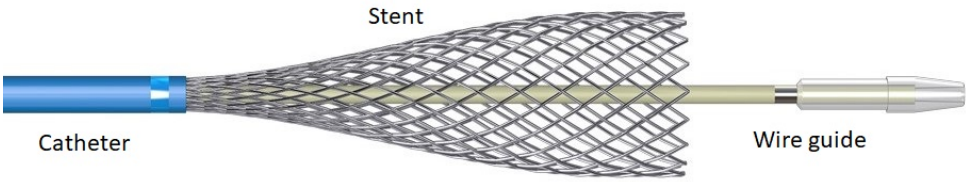

Figure 1.1: Deployment of a self-expandable stent from a catheter [8].

Numerous different stent geometries exist in the literature. To narrow down the scope of the project, this study focuses on self-expanding open-ended braided stents, as shown in Figure 1.1. Open-ended means that the wires are not welded or connected by any other means at the ends of the stents, only interwire contact holds the individual wires in place. While there are numerous promising materials and geometries, this type of stent is selected for this project, mainly because of its high flexibility that makes it suitable for narrow and curved arteries [30]. The stents considered in this study are made of a nickel-titanium alloy, better known as nitinol. Since nitinol is a metal, and blood vessel tissue is a relatively soft material, placing the stent without damaging the tissue can be challenging, especially in narrow or curved arteries.

To personalize stent placement interventions, data on stent performance should be collected. The stent's geometrical parameters as well as the configuration, such as bent or straight, are important for the mechanical behaviour. Since it is not possible from a practical, ethical and economical perspective to perform in vivo experiments on each stent placement, highly accurate numerical models are essential to gather this data and to predict the behaviour. Such data then can be used to optimize the stent's geometry and in vivo performance.

1.2 Previous work

A lot of development in stent material and geometry has been achieved since the first placed stent in 1986. Among the materials used are polymers such as shape memory polyurethane (SMPU), biodegradable polymers such as polydioxanone (PDO), and shape memory alloys such as nitinol [13, 20, 29]. Recent work is investigating drug-eluting stents to reduce the risk of in-stent thrombosis [31]. Regarding the geometry of the stent, different manufacturing techniques are creating a range of geometries. The most advanced manufacturing techniques rely on braiding technology or cutting by electrical discharge machining [19, 22]. As mentioned previously, this study focuses on self-expanding open-ended braided stents made of nitinol.

In attempts to capture the mechanical behaviour of these braided stents in a numerical model, the most often used method in the literature is a beam model. Nearly all models in the literature use linear Timoshenko beam elements to model the stent's wires. Where the models do differ, is the method of modelling the cross-over points, see Figure 1.2. A frequently used method is to prescribe a hinge at the cross-over point, also referred to as the 'join' method [6, 28]. When using this method, the weaving of the wires at the cross-over points is usually neglected. Individual wires are defined as perfect cylindrical springs and pass through each other as depicted in Figure 1.2a. Since a hinge is prescribed at the cross-over point, sliding of the wires is not possible. Three translational degrees of freedom (DOFs) are fixed, while the rotational DOFs are unconstrained.

(a) Join method.

(b) Weave Method.

Figure 1.2: A close up of two cross-over points in a beam element model using the join method (a) and the weave method (b).

The second frequently used method is using a contact definition to define the interaction at the cross-over points [19, 32]. In the literature, this method is typically referred to as the 'weave' method. In this method, the weaving of the wires is not neglected and the geometry of the model as shown in Figure 1.2b represents the actual geometry of the stent more accurately. In this definition, contact is defined between the wires with an interwire friction coefficient of 0.2 [14].

Usually, studies use either the join or the weave method, without comparing both methods. Recently, Kelly et al. have made a comparison between the two methods for an open-ended braided stent made of nitinol [18]. In terms of computational time, the join method has an advantage over the weave method since prescribing a hinge requires less computational effort than prescribing a contact definition. In terms of capturing the reaction forces while being compressed, little difference was observed between both methods and experimental results. However, a notable difference is the variety in deformation pattern as shown in Figure 1.3. The bunching together of the wires at the stent's ends shown in the weave method corresponds with the deformation observed in experimental settings [18]. In the literature, this effect is also referred to as the 'fishmouth configuration' or 'fish mouthing effect'. In the join method, bunching together is constrained by the hinge. Instead of bunching together, strain concentrations are observed close to the stent ends.

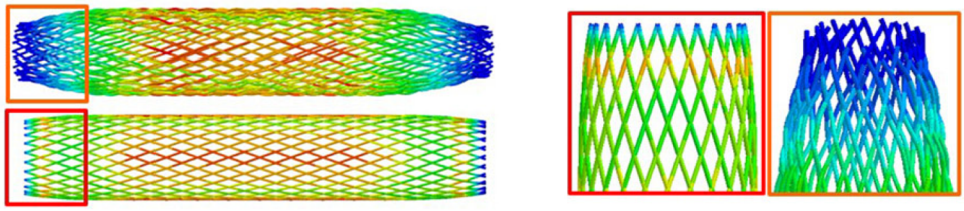

Figure 1.3: A stent beam model using the weave method (orange square) or join method (red square). Radial compression is applied to both models, reducing the diameter from 15.8 mm to 7.5 mm. The colors indicate the maximum principal strain on the scale from 0 (blue) to 0.0042 (red) [18].

Although a beam model in combination with the weave method can capture the mechanical behaviour of a stent, the computational time, which is in the range of hours, is considerable. In addition, doubts remain about the accuracy of the model. In nearly all the literature, the load case that is applied to the numerical model and validated with experiments is uniform radial compression. More complex load cases have, to date, not been validated. More complex deformations might be captured more accurately by 3D solid elements than by beam elements. However, a full solid model of the stent would be computationally too expensive.

Though not frequently used because of the high computational time, Frost et al. have built a numerical model using solid elements [13]. Two single wires of the stent were modelled, made up by a fairly fine mesh of 23.000 elements each. The simulations were performed on this single wire couple, which kept the computational time acceptable. Macroscopic properties and deformation were calculated by using the geometric symmetry of the stent. In this model, weaving of the wires and contact was neglected, as is done in the join method. A visual representation of the model is depicted in Figure 1.4. The resulting deformation and properties matched well with the beam models using the join method. In this work, the use of solid elements instead of beam elements is interesting. However, more complex deformations and contact behaviour have not been investigated.

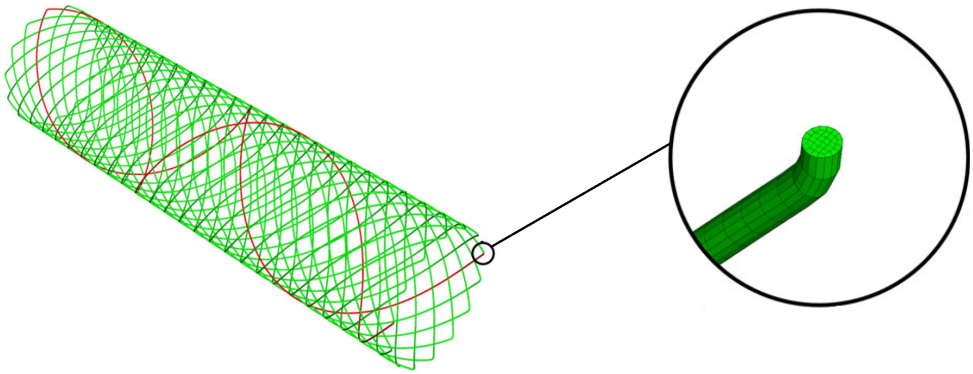

Figure 1.4: A stent model of a wire couple (red) of 8-node brick elements. The full stent geometry of 14 identical couples (green) is created by using symmetry operations [13].

Another approach to predict the mechanical behaviour of braided stents is through a mathematical model. Jedwab and Clerc developed a model based on independent parallel helical springs [17]. Later work showed that the expressions of Jedwab and Clerc contained an error, which was corrected in an erratum [5]. The model takes the stent's geometrical parameters such as length, diameter, and wire thickness as input. As output, it provides the required forces to deform the stent to a prescribed diameter, and the stent's radial and axial stiffness at that diameter. Another property that the model can calculate is the maximum possible diameter reduction, which can be used for calculating the required catheter size.

The mathematical model shows good agreement with experimental results for a radial compression load case. However, the model is validated with only one stent geometry. For different geometries, the expressions might be less accurate, especially since the model assumes elastic deformation only and neglects both weaving of the wires and friction. An advantage of the mathematical model is the computational time required to calculate the output, which is in the order of milliseconds. A detailed description of the mathematical model, including all expressions, can be found in Appendix A.

1.3 Objective

The aim of this study in the long term is to develop a modelling strategy that can capture the mechanical behaviour of a braided stent in a more computationally efficient manner, without compromising on simplifying assumptions such as infinite stent length, perfect cylindrical shape of the blood vessel, and simplified stent-tissue contact [1, 7, 9]. An improvement of existing beam models using a more advanced contact description is one of the methods considered. Since the microstructural features are much smaller than the overall dimensions of the stent, more advanced multi-scale techniques that rely on computational homogenization or the quasicontinuum method are considered as well [25, 33].

To decide which technique is the most suitable, a thorough understanding of the stent mechanics at the microscale is essential. Within the scope of this thesis, the goal is to develop a detailed single-scale unit cell model using solid elements to capture the stent mechanics as detailed as possible. The validity of the beam models used in the literature is investigated by comparing their results to the detailed unit cell model. The multi-scale homogenization approach is kept in mind while developing the single-scale model, i.e., the unit cell model is developed in such a way that it can be implemented in a fully coupled multi-scale model [21]. Next to the development of the microscale model, semi-periodic models using multiple unit cells are developed.

1.4 Report outline

The geometry of a braided stent, including the chosen material model, is described in section 2.1. The rationale behind the selected method is explained in section 2.2, together with a brief explanation of the homogenization method and the choice of RVE. The implementation and verification of the unit cell are explained in section 2.3. The simulation approaches for the unit cell and the semi-periodic model are described in section 2.4 and 2.5. The results of the simulations, including a description of the applied load cases, are provided and discussed in Chapter 3. Finally, conclusions and recommendations for future work are made in Chapter 4.

1.5 Notation

Throughout this report, the following notation will be used

- scalars a,
- vectors $\vec{a}$,
- second order tensors $\mathbf{A} = A_{ij}\vec{e}_i\vec{e}_j$,
- matrix notation of second-order tensors $\underline{\mathbf{A}}$,
- third order tensors ${}^3\mathbf{A} = A_{ijk}\vec{e}_i\vec{e}_j\vec{e}_k$,
- gradient operator $\vec{\nabla} = \sum_{i=1}^{n} \vec{e}_i \frac{\partial}{\partial x_i}$,
- time derivative $\dot{a} = \frac{\partial a}{\partial t}$.

2 Methodology

2.1 Full-scale stent model, geometry and material

The first step in developing the numerical model is to generate the geometry in a computational environment. An analytical description of the stent geometry is used, based on the expressions in the work of Kim et al. [19]. The full geometry of the braided stent can be described using only five parameters, see Figure 2.1a. Besides the depicted length L, braiding angle α, average diameter D, and wire thickness t, the number of clockwise (cw) wires n completes all required parameters to define the geometry. Since the number of cw wires is equal to the number of counterclockwise (ccw) wires, the total number of wires is equal to $2n$.

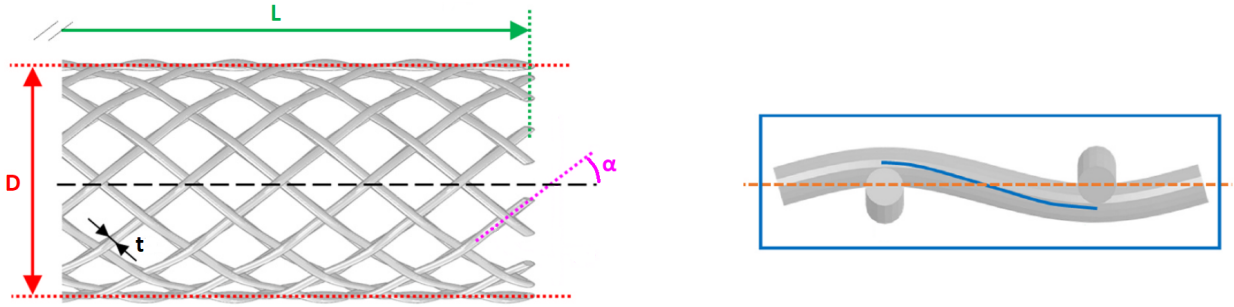

(a) Stent geometrical parameters L, D, α and t.

(b) Oscillation around the average diameter.

Figure 2.1: A visual representation of the braided stent's geometrical description [36].

As shown in Figure 2.1b, the stent's individual wires oscillate around the average diameter with a sinusoidal wave. The external diameter of the stent D_e can be calculated with $D + 2t$. The number of revolutions of an individual wire, denoted by n_{rev}, is calculated as

$$n_{rev} = \frac{L \tan(\alpha)}{\pi D}. \tag{2.1}$$

The geometry of individual wires is best expressed in polar coordinates, using radial distance r, angle θ, and axial coordinate z : $\{r, \theta, z\}$. The wire's centerline coordinates are expressed as a function of axial coordinate z, with $z \in [0, L]$. The z-axis coincides with the stent's central axis. Additionally, the wire number i is defined, with $i = \{1, ..., n\}$. The centerline coordinates in θ can be expressed as a function of axial coordinate z and wire number i as

$$\theta(z, i) = c\frac{2\pi z n_{rev}}{L} + \frac{2\pi(i-1)}{n}. \tag{2.2}$$

In this equation, the constant c is equal to 1 for cw wires and -1 for ccw wires. The radial distance r of the wire's centerline is expressed as a function of the angular coordinate θ as

$$r(\theta) = \frac{D}{2} + \frac{t}{2}\cos(\theta n). \tag{2.3}$$

Material model

The next step in the model development is to select a material model that accurately represents the behaviour of the highly non-linear nitinol material. Nitinol is a nickel-titanium alloy that exists in two different solid phases: austenite and martensite. Both phases have different atomic structures and different Young's moduli. When loaded, the austenite can transform to martensite and vice-versa. This allows the nitinol material

to recover from high strains, without being plastically deformed. This pseudoelasticity, also known as superelasticity, makes nitinol an interesting material in cases where high strains apply.

In the literature, the Auricchio model has been widely used to describe the non-linear superelastic behaviour of shape-memory alloys. One of the most striking features of the Auricchio model is the limited number of material parameters involved. The mechanical evolution from austenite to martensite and vice-versa requires the specification of just seven parameters, assuming a constant temperature [16]. These seven parameters can be effectively identified from tensile tests. Performing experiments is essential because the properties of nitinol highly depend on the manufacturing process. In the model, the start and end point of the austenite to martensite transformation (AS), denoted by subscript s and f respectively, are defined by transformation stresses σ_{s}^{AS} and σ_{f}^{AS}. The start and end transformation stresses from martensite to austenite (SA) are defined by σ_{s}^{SA} and σ_{f}^{SA}. Note that these stresses are temperature dependent, as depicted in Figure 2.2b.

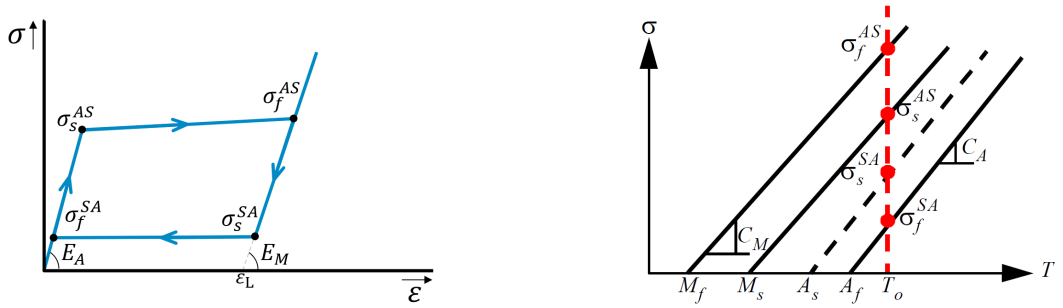

(a) Stress-strain curve of nitinol.

(b) Temperature dependence of nitinol.

Figure 2.2: The Auricchio material model. The nitinol stress-strain curve, defined by transformation stresses σ_{s}^{AS}, σ_{f}^{AS}, σ_{s}^{SA} and σ_{f}^{SA} (a). The temperature dependence of the transformation stresses (b) [24].

As can be observed from Figure 2.2a, the stress values of the SA transformation are significantly lower than the AS transformation, which creates a hysteresis loop in the stress-strain curve. Next to σ_{s}^{AS}, σ_{f}^{AS}, σ_{s}^{SA}, and σ_{f}^{SA}, Young's moduli E_{A}, E_{M}, and transformation strain ε_{L} complete the input parameters for the Auricchio material model. The transformation strain is the strain that is reached during the phase transformation, as depicted in Figure 2.2a. All parameters used in this study are experimentally derived and are provided in Table 1. The mathematical implementation of the model is provided in Appendix B.

Table 1: Experimentally obtained material parameters of the nitinol stent [23].

Parameter	Value	Unit
E_{A}	42.1	[GPa]
E_{M}	31.4	[GPa]
σ_{s}^{AS}	366	[MPa]
σ_{f}^{AS}	402	[MPa]
σ_{s}^{SA}	85	[MPa]
σ_{f}^{SA}	80	[MPa]
ε_{L}	0.0665	[-]

It has to be noted that the values in Table 1 are measured at a temperature of 295 Kelvin. To map the temperature dependence of nitinol, the temperature coefficients C_{A} and C_{M} should be established by performing the experiments at multiple temperatures. For now, the values at 295 K are used. When C_{A} and C_{M} are known, the material parameters at body temperature (310 K) should be used instead.

2.2 Choice of method

Using the mathematical expressions for the braided stent geometry and Auricchio's material model, a full-scale model using hexahedral elements is created in a numerical environment, see Figure 2.3.

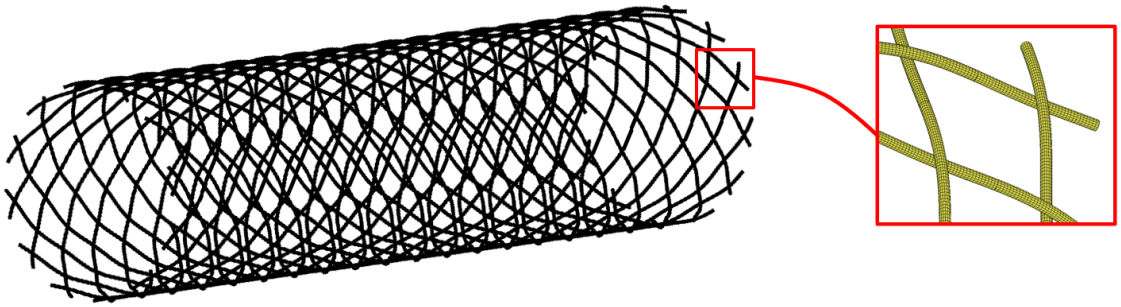

Figure 2.3: Trimetric view of the full-scale stent model made of 806,400 3D 8-node hexahedral elements.

A non-linear numerical simulation of this full-scale model is computationally too expensive, if not impossible. Even when beam elements are used instead of hexahedral elements, resulting in a full-scale mesh of only 4,320 elements, the computational time is still in the order of hours, which is considered too high. This is mainly caused by the high number of contact points in the model. The first considered approach to reduce the computational time is an improvement of the existing beam model. An improvement of the interwire contact description could result in a significant reduction in computational effort. Since the microstructural features are smaller than the overall dimensions of the stent, more advanced multi-scale techniques are considered to capture the stent's mechanical behaviour.

One of the considered multi-scale strategies relies on the quasicontinuum method (QC). This method, as depicted in Figure 2.4b, has proven to capture the behaviour of stent-like structures accurately in the form of carbon nanotubes [35]. There are two main principles of the QC method that result in a computational cost advantage, reducing the number of DOFs by applying interpolation, and ensuring that a subset of points is visited instead of all points to construct the governing equations [4].

The second considered multi-scale method is based on computational homogenization. This method, as depicted in Figure 2.4c, is used in the literature to homogenize the behaviour of repeating heterogeneous patterns [26]. Since the braided stent geometry can also be described by a repeating pattern, homogenizing a representative volume element (RVE) and using its effective properties is a promising and computationally efficient method.

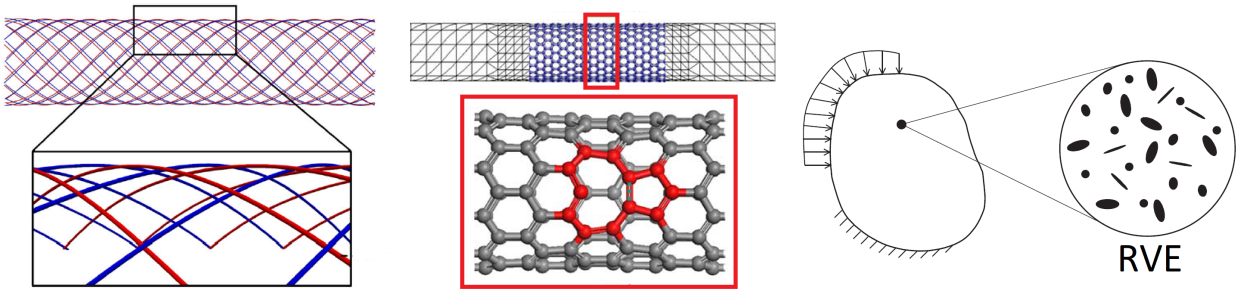

(a) Beam model [30]. (b) Quasicontinuum method [35]. (c) Computational homogenization [21].

Figure 2.4: The considered methods to capture the stent mechanics in a computationally efficient manner: improving the beam model by redefining the contact description between beams (a), the quasicontinuum method (b), and computational homogenization (c).

To decide which approach is the most suitable, a thorough understanding of the stent mechanics at the microscale is essential. For the computational homogenization approach, a detailed RVE has to be developed,

which is valuable in two ways: it provides detailed information on the local microstructural behaviour as well as on effective macroscopic material properties [21]. For this reason, this is the selected method for now, with a focus on RVE development. An explanation of the principles of computational homogenization is provided in section 2.2.1, including a brief explanation of the selected second-order framework. The choice of the RVE is detailed in section 2.2.2.

2.2.1 Computational homogenization

The general idea of computational homogenization, as depicted in Figure 2.5, is to replace the heterogeneous material at the macroscale with a homogeneous problem, with the effective material properties obtained from the heterogeneous microstructure [21]. In this method, at each macroscopic integration point i_g, the deformation gradient tensor $\mathbf{F}_\mathrm{M}$ is calculated. This tensor is then used to formulate the boundary conditions on the RVE. The non-linear RVE problem is solved, and the first Piola-Kirchhoff stress tensor $\mathbf{P}_\mathrm{M}$ and tangent ${}^4\mathbf{C}_\mathrm{M}$ are obtained by averaging the resulting stress field over the volume of the RVE. These values are transferred to the macroscale, where they enter a macroscopic equilibrium problem. The numerical implementation of this first-order framework, including a computational example, is detailed in Appendix D.1.

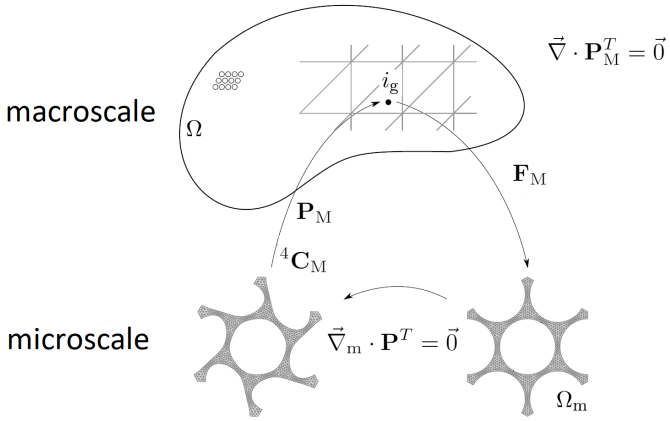

Figure 2.5: Sketch of a computational homogenization framework. At each integration point i_g of the macroscopic domain Ω, a representative volume element (RVE) with domain Ω_m is considered, inside which the microfluctuation field is computed. Homogenized properties are transferred back to the macroscale [26].

In the case of a stent, the element thickness at the macroscale approaches the microstructural scale. Geers, Coenen, and Kouznetsova developed a fully coupled multi-scale (FE^2) computational homogenization framework where this is addressed properly, using shell elements at the macroscale [15]. Based on this method, a multi-scale model for the stent is proposed as shown in Figure 2.6.

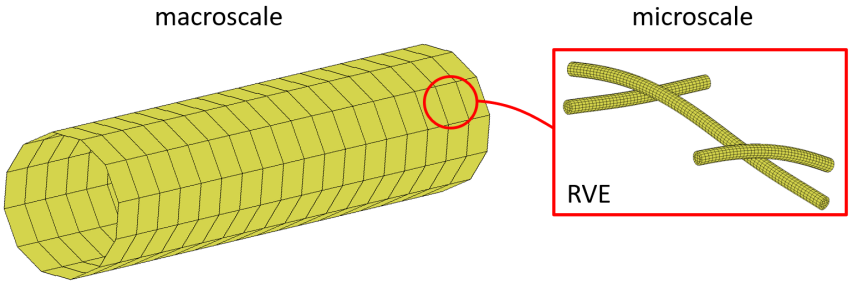

Figure 2.6: Trimetric view of the proposed FE^2 model of a braided stent with Kirchhoff-Love thin shell elements at the macroscale. Effective macroscopic properties are calculated based on the underlying microstructure of the stent, represented by the RVE.

Numerical implementation of the second-order framework

By using the framework as depicted in Figure 2.5, first-order deformations such as tension, compression, and shear can be applied to the RVE. However, for localized deformations, such as indentation of the stent, first-order type of deformations at the RVE level might not be capable of capturing the overall stent mechanics accurately. Prescribing higher-order deformation modes, such as bending, provides richer kinematics at the RVE level, which results in more accurate macroscopic properties. Besides that, bending at the RVE level is an interesting load case to study the microstructural behaviour. A higher-order scheme is provided below, using a planar cubic unit cell. The extension to the curved stent unit cell is detailed in section 2.3

A computational homogenization scheme with second-order kinematics at the microscale is developed by Geers et al. [10,15]. This framework is used and carefully implemented to create the RVE of the stent. With respect to the first-order framework, there are a number of key differences, which are explained here briefly. A more elaborate description is provided in Appendix D.2. The RVE, as depicted in Figure 2.7, is defined as a 3D heterogeneous unit cell with eight corner nodes. In this framework, the deformation of the RVE is split into an in-plane and an out-of-plane component, denoted by a superimposed $\hat{}$ and $\tilde{}$, respectively. The in-plane component is defined as the projection onto the $(\vec{e}_1^c,\vec{e}_2^c)$-plane. The out-of-plane component is the projection along the $\vec{e}_3^c$-direction.

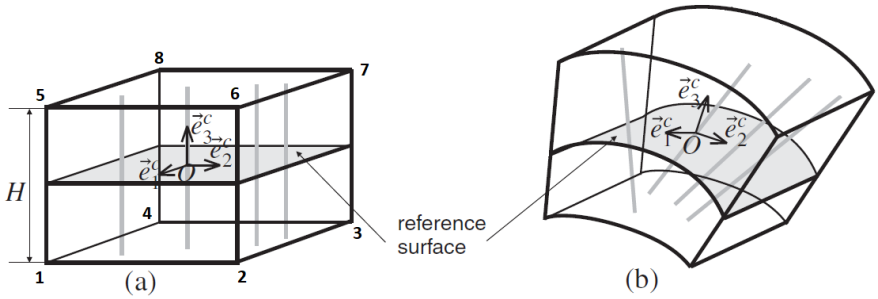

Figure 2.7: An example of an RVE in the reference (a) and deformed (b) configuration [10].

In addition to the deformation gradient tensor $\mathbf{F}_\mathrm{M}$, the curvature tensor $\mathbf{K}_\mathrm{M}$, which is related to the gradient of $\mathbf{F}_\mathrm{M}$ as explained in Appendix D, is used to prescribe a second-order deformation. Since the RVE is represented by a Kirchhoff-Love thin shell element at the macroscale, plane stress is assumed in the out-of-plane direction. To ensure there are no resulting stresses in the out-of-plane direction, only in-plane constraints are applied. Five in-plane displacements are prescribed as

$$\begin{aligned}
\hat{\tilde{u}}^i_\mathrm{m} &= (\hat{\tilde{\mathbf{F}}}_\mathrm{M} - \hat{\tilde{\mathbf{I}}} + \zeta^1 \hat{\tilde{\mathbf{K}}}_\mathrm{M}) \cdot \hat{\tilde{\vec{X}}}^i_\mathrm{m}, \qquad i = 1,2,4, \\
\hat{\tilde{u}}^{56}_\mathrm{m} &= \hat{\tilde{u}}^6_\mathrm{m} - \hat{\tilde{u}}^5_\mathrm{m} = (\hat{\tilde{\mathbf{F}}}_\mathrm{M} - \hat{\tilde{\mathbf{I}}} + \zeta^5 \hat{\tilde{\mathbf{K}}}_\mathrm{M}) \cdot (\hat{\tilde{X}}^6_\mathrm{m} - \hat{\tilde{X}}^5_\mathrm{m}), \\
\hat{\tilde{u}}^{58}_\mathrm{m} &= \hat{\tilde{u}}^8_\mathrm{m} - \hat{\tilde{u}}^5_\mathrm{m} = (\hat{\tilde{\mathbf{F}}}_\mathrm{M} - \hat{\tilde{\mathbf{I}}} + \zeta^5 \hat{\tilde{\mathbf{K}}}_\mathrm{M}) \cdot (\hat{\tilde{X}}^8_\mathrm{m} - \hat{\tilde{X}}^5_\mathrm{m}).
\end{aligned} \tag{2.4}$$

In this equation, $\hat{\tilde{\mathbf{I}}}$ is the second-order unit tensor, and ζ is the out-of-plane component along $\vec{e}_3^c$, with $\zeta \in [-H/2, H/2]$. Note that $\hat{\tilde{u}}^{56}_\mathrm{m}$ and $\hat{\tilde{u}}^{58}_\mathrm{m}$ are not prescribing the displacement of a single node, but a relative displacement of two nodes. To complete the RVE, periodic boundary conditions for the in-plane and out-of-plane components are prescribed to ensure correct application of the macroscopic deformation, and to ensure equal microfluctuations on opposite sides. The numerical implementation of these periodic boundary conditions in MSC Marc/Mentat is done using servo links, as shown in the work of Drach et al., see also Appendix D [12].

Now that the RVE is constructed and deformations can be applied, the effective macroscopic properties can be calculated. In this second-order framework for shells, macroscopic properties are described by the engineering stress resultant tensor $\hat{\tilde{\mathbf{N}}}_\mathrm{M}$ and the couple-stress resultant tensor $\hat{\tilde{\mathbf{M}}}_\mathrm{M}$. After running the simulation, in-plane reaction forces $\hat{\tilde{f}}_\mathrm{m}$ in the prescribed nodes with the undeformed position vectors $\hat{\tilde{X}}_\mathrm{m}$ are used to calculate

these macroscopic stress resultants as

$$\hat{\hat{\mathbf{N}}}_{\mathrm{M}} = \frac{1}{A_{\mathrm{m}}} \sum_i \hat{\hat{f}}^i_{\mathrm{m}} \hat{\vec{X}}^{i\star}_{\mathrm{m}}, \qquad i = 1, 2, 4, \hat{56}, \hat{58}, \tag{2.5}$$

$$\hat{\hat{\mathbf{M}}}_{\mathrm{M}} = \frac{1}{A_{\mathrm{m}}} \sum_i \zeta^i \hat{\hat{f}}^i_{\mathrm{m}} \hat{\vec{X}}^{i\star}_{\mathrm{m}}, \quad i = 1, 2, 4, \hat{56}, \hat{58}, \tag{2.6}$$

2.2.2 Choice of RVE

The RVE is defined as the smallest repeating unit representing the full geometry of the stent, also known as a unit cell. The terms RVE and unit cell are used interchangeably in this report. In the literature, only one recent study that uses a unit cell of a braided stent has been found. However, this study only used the unit cell to identify the stent's minimum and maximum diameter, the microstructural behaviour was not investigated thoroughly, and no macroscopic properties were calculated [36]. In the research field of textiles and braided composites, developing a unit cell is a more common approach [27, 37]. Ayranci and Carey proposed a curved unit cell model to predict the macroscopic properties of braided tubular composites [3]. Their proposed model is depicted in Figure 2.8.

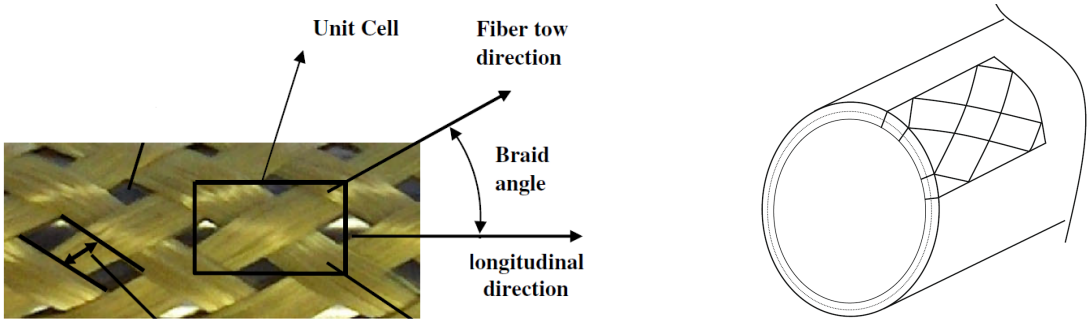

(a) (b)

Figure 2.8: The proposed unit cell by Ayranci and Carey for a braided tubular structure [3].

The geometry of this braided tube holds similarities with the geometry of a braided stent. Based on this work, a similar unit cell is developed for the stent, see Figure 2.9a.

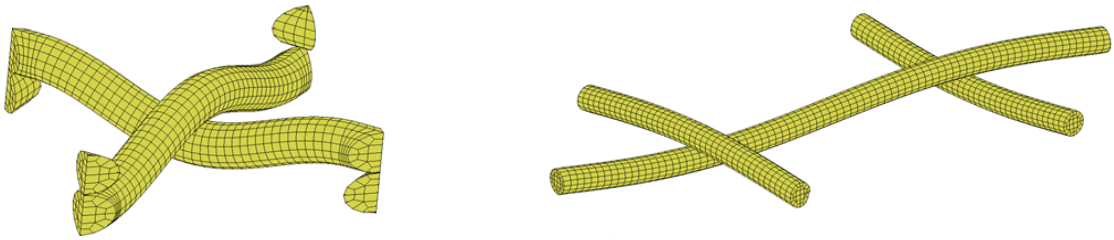

(a) The first design of the unit cell. (b) The updated unit cell design.

Figure 2.9: The planar unit cell based on the work of Ayranci and Carey (a) [3]. The updated planar unit cell with the wire crossings not at the corners of the RVE (b).

Although successfully used in the literature for an analytical study [3], issues arise when implementing this unit cell in a numerical environment. In case the wires start sliding, interwire contact is lost at the corners of the unit cell. For this reason, a different unit cell is chosen, as shown in Figure 2.9b.

At first, the chosen unit cell is implemented in a 3D planar case. This is done to verify the numerical implementation first, before moving on to the more complex curved unit cell. However, when performing

simulations on the updated planar unit cell, multiple issues occurred with convergence and contact. The issues were mainly caused by the separation of the wires during the simulation. Since in the curved unit cell, separation of the wires is prevented naturally by the curvature of the unit cell as a whole, it is decided to directly study the curved RVE, without investigating the simpler planar geometry first. The curved stent unit cell is depicted in Figure 2.10.

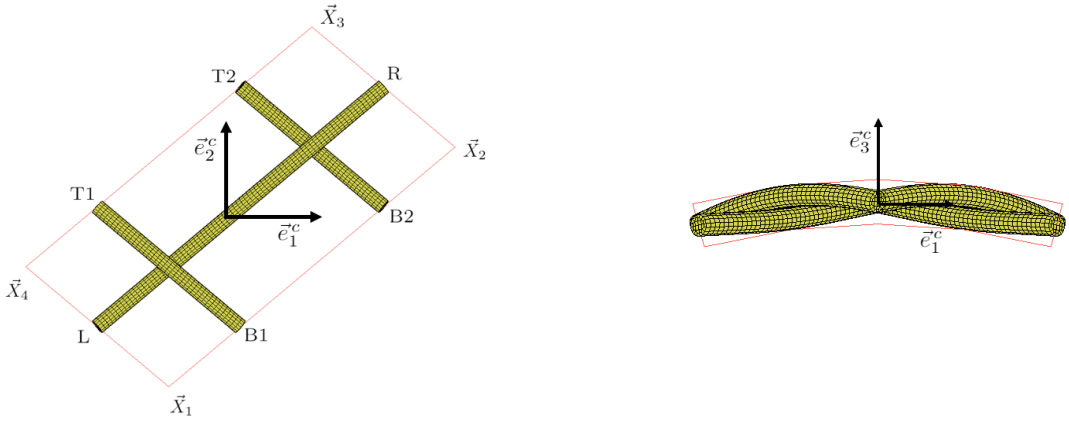

(a) Top view.

(b) Side view.

Figure 2.10: Top view (a) and side view (b) of the defined unit cell, including the position vectors $\vec{X}_1$ till $\vec{X}_4$, and local coordinate system $\{\vec{e}_1^c, \vec{e}_2^c, \vec{e}_3^c\}$.

A local cylindrical coordinate system is defined by $\{\vec{e}_1^c, \vec{e}_2^c, \vec{e}_3^c\}$, corresponding with the tangential, axial and radial direction respectively. Position vectors $\vec{X}_5$ till $\vec{X}_8$, which only differ in the $\vec{e}_3^c$-coordinate from $\vec{X}_1$ till $\vec{X}_4$, are not depicted for clarity. The position vectors expressed in normalized local coordinates are provided in Table 2.

Table 2: The position vectors of the stent unit cell, expressed in normalized local coordinates $\{\xi_1, \xi_2, \xi_3\}$.

Position vector	Normalized local coordinates $\{\xi_1, \xi_2, \xi_3\}$
$\vec{X}_1$	$\{-\frac{1}{3}, -1, -1\}$
$\vec{X}_2$	$\{1, \frac{1}{3}, -1\}$
$\vec{X}_3$	$\{\frac{1}{3}, 1, -1\}$
$\vec{X}_4$	$\{-1, -\frac{1}{3}, -1\}$
$\vec{X}_5$	$\{-\frac{1}{3}, -1, 1\}$
$\vec{X}_6$	$\{1, \frac{1}{3}, 1\}$
$\vec{X}_7$	$\{\frac{1}{3}, 1, 1\}$
$\vec{X}_8$	$\{-1, -\frac{1}{3}, 1\}$

A Python script is developed to generate each node and element of the unit cell mesh, ensuring that the mesh is perfectly congruent. The input parameters of the script are the geometrical parameters L, D, α, t, and n, as explained in section 2.1. Additionally, material properties, friction coefficient, mesh size, and prescribed deformation can be specified. A detailed description of the script is provided in Appendix C.

The Python output serves as input for the selected FE environment, MSC Marc/Mentat. This software package is chosen because of its implicit solver and its ability to implement the periodicity by using servo links [12]. In the beam model currently developed in the literature, an explicit solver is used. It is expected that a computational time advantage can be achieved when using an implicit solver. Because of the high number of contact points, the current beam model does not converge with an implicit solver. Since the unit cell is a far simpler model with only two wire crossings, its convergence behaviour is expected to be better.

2.3 RVE implementation and verification

The framework described in the previous section is implemented to create the stent RVE. Since the framework is based on a rectangular RVE in a Cartesian coordinate system and the stent's RVE is parallelepiped shaped and has a polar coordinate system, the implementation should be done carefully. Furthermore, the limitations of applying curvature to the RVE are investigated. A more elaborate description of this limitation study is provided in Appendix E.

2.3.1 Framework implementation

Application of curvature

Though prescribing bending at the RVE level is possible using the developed framework, the curvature that can be applied is limited [10]. This might restrict the investigation of localized deformations, like stent indentation. To investigate eventual side effects and the ability of the framework to calculate the bending moment, a 2D homogeneous sample is created and bent to various angles. Plane strain is assumed in the third direction. In-plane displacements are used to apply the deformation. Periodic boundary conditions are applied, coupling the left and right edge of the sample. The deformed sample is depicted in Figure 2.11.

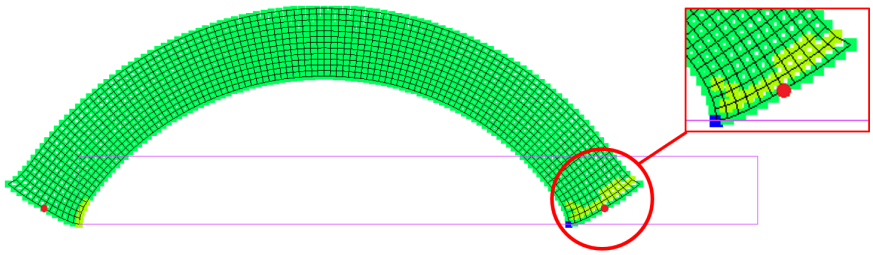

Figure 2.11: The deformed 2D homogeneous sample with a length-to-height ratio of 10:1. The bending angle is 120°, prescribed by in-plane displacements. The contour of the undeformed mesh is depicted in purple.

As can be observed, the deformations near the corners of the sample are irregular. The root cause of this anomaly is that the in-plane length change of the sample is not taken into account when calculating the prescribed displacements $\hat{\vec{u}}_{\mathrm{m}}$. In other words, it is assumed that the horizontal distance between the red dots in Figure 2.11 is constant. As can be observed in the figure, this distance is undoubtedly shorter than in the undeformed sample. To take this into account in the boundary conditions, the equations to calculate the in-plane displacements $\hat{\vec{u}}_{\mathrm{m}}$ are updated by introducing $\hat{\bar{\mathbf{F}}}_{\mathrm{M}}$ (highlighted in blue) as follows:

$$\begin{aligned}
\hat{\vec{u}}^{i}_{\mathrm{m}} &= (\hat{\bar{\mathbf{F}}}_{\mathrm{M}} - \hat{\bar{\mathbf{I}}} + \hat{\bar{\mathbf{F}}}_{\mathrm{M}} \cdot \zeta^{1}\hat{\bar{\mathbf{K}}}_{\mathrm{M}}) \cdot (\hat{\vec{X}}^{i}_{\mathrm{m}} - \hat{\vec{X}}^{1}_{\mathrm{m}}), \qquad i = 1, 2, 4, \\
\hat{\vec{u}}^{56}_{\mathrm{m}} &= \hat{\vec{u}}^{6}_{\mathrm{m}} - \hat{\vec{u}}^{5}_{\mathrm{m}} = (\hat{\bar{\mathbf{F}}}_{\mathrm{M}} - \hat{\bar{\mathbf{I}}} + \hat{\bar{\mathbf{F}}}_{\mathrm{M}} \cdot \zeta^{5}\hat{\bar{\mathbf{K}}}_{\mathrm{M}}) \cdot (\hat{\vec{X}}^{6}_{\mathrm{m}} - \hat{\vec{X}}^{5}_{\mathrm{m}}), \\
\hat{\vec{u}}^{58}_{\mathrm{m}} &= \hat{\vec{u}}^{8}_{\mathrm{m}} - \hat{\vec{u}}^{5}_{\mathrm{m}} = (\hat{\bar{\mathbf{F}}}_{\mathrm{M}} - \hat{\bar{\mathbf{I}}} + \hat{\bar{\mathbf{F}}}_{\mathrm{M}} \cdot \zeta^{5}\hat{\bar{\mathbf{K}}}_{\mathrm{M}}) \cdot (\hat{\vec{X}}^{8}_{\mathrm{m}} - \hat{\vec{X}}^{5}_{\mathrm{m}}).
\end{aligned} \tag{2.7}$$

The deformed sample, using the updated displacement prescription, is depicted in Figure 2.12.

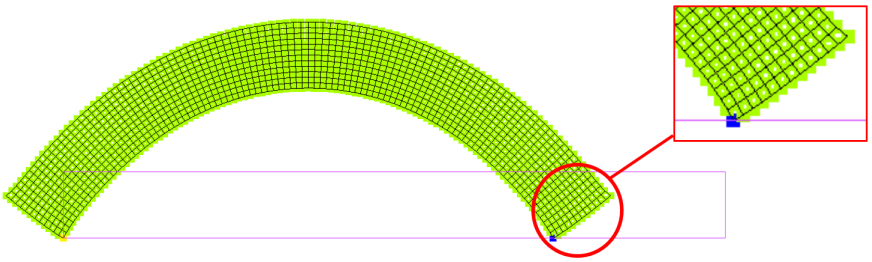

Figure 2.12: The deformed sample using the formulation of equation 2.7 to apply the bending angle of 120°.

As can be observed, the side effects are still present, but are less severe than in the previous simulation. It can be concluded that the updated formulation results in a more realistic deformation at the edges of the sample. Furthermore, it can be concluded that the couple-stress resultant $\hat{\mathbf{M}}_{\mathrm{M}}$ is more accurately represented for the updated formulation, as shown in Appendix E. This is especially true for samples with a large length-to-height ratio. The simulation is repeated for a 3D homogeneous sample and yields the same results, which is shown as well in Appendix E.

Despite the improvement of the equations, large curvatures still show edge effects. It is suggested to limit the applied curvature, $\kappa \ll 1$ mm^{-1}, since the severity of the edge effects for the stent unit cell is uncertain. The question is whether the curvatures needed to describe the stent deformation are in a range that is suitable for the described method. Based on images from models and experiments in the literature, the typical curvature due to the fish mouthing effect at the stent ends is low, $\kappa \leq 0.05$ mm^{-1}. A typical example of another deformation mode that requires the application of curvature is the bending of the stent as a whole. In the case of bending the stent 90°, the curvature κ would be $\frac{1}{r}$ with $r = \frac{L}{\frac{90}{360} * 2\pi}$. For a typical stent length of 60 mm, the curvature κ would be equal to 0.026 mm^{-1}, which is an acceptable value. Deformation due to indentation might be a problem because the deformation is highly localized, resulting in high local curvatures. In this case, the undesired by-products might dominate the solution.

Curved parallelepiped shaped unit cell

As shown, the stent's unit cell is parallelepiped shaped and has a polar coordinate system, and thus the implementation requires care. As depicted in Figure 2.13b, the adjacent unit cell is shifted with respect to its neighbour. This means that the wire end labelled 'T1' should be coupled to 'B2' and 'T2' should be coupled to 'B1'. In this thesis, this coupling is referred to as 'brick periodicity', because the stacking is similar to the stacking of building bricks.

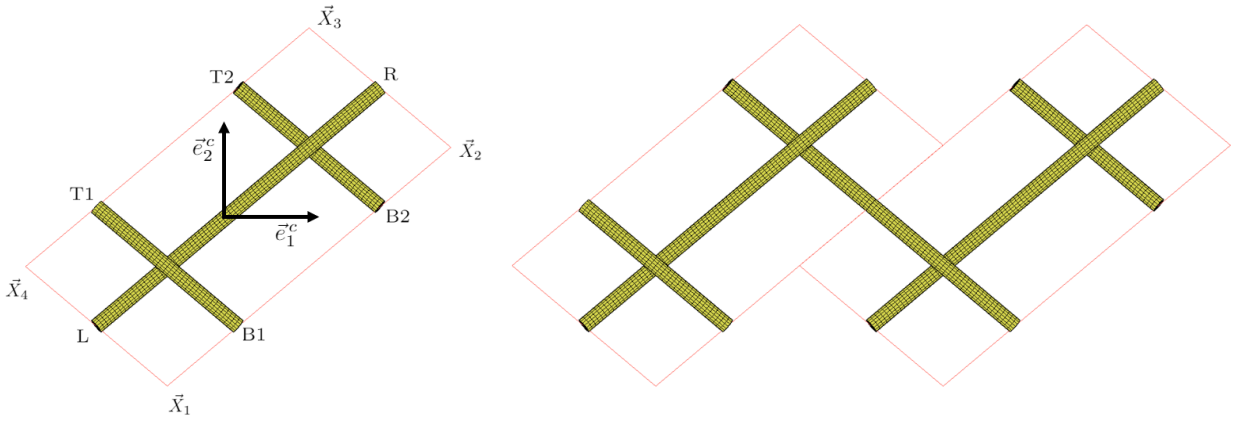

(a) (b)

Figure 2.13: Top view of the defined unit cell (a). Two adjacent stent unit cells (b).

To correctly implement the brick periodicity, the tying equations should be modified carefully. Together with the second-order type of deformations, polar coordinate system, and parallelepiped unit cell shape, the tying equations for the in-plane and out-of-plane component become as

$$\begin{aligned}
\hat{\vec{u}}_{\mathrm{m}}^{T1} &= \hat{\vec{u}}_{\mathrm{m}}^{B2} + (1-\eta)(\frac{1}{2}\hat{\vec{u}}_{\mathrm{m}}^{4} - \frac{1}{4}\hat{\vec{u}}_{\mathrm{m}}^{2} - \frac{1}{4}\hat{\vec{u}}_{\mathrm{m}}^{1}) + (1+\eta)(\frac{1}{2}\hat{\vec{u}}_{\mathrm{m}}^{58} - \frac{1}{4}\hat{\vec{u}}_{\mathrm{m}}^{56}),\\
\hat{\vec{u}}_{\mathrm{m}}^{T2} &= \hat{\vec{u}}_{\mathrm{m}}^{B1} + (1-\eta)(\frac{1}{2}\hat{\vec{u}}_{\mathrm{m}}^{4} + \frac{1}{4}\hat{\vec{u}}_{\mathrm{m}}^{2} + \frac{3}{4}\hat{\vec{u}}_{\mathrm{m}}^{1}) + (1+\eta)(\frac{1}{2}\hat{\vec{u}}_{\mathrm{m}}^{58} - \frac{1}{4}\hat{\vec{u}}_{\mathrm{m}}^{56}),\\
\hat{\vec{u}}_{\mathrm{m}}^{R} &= \hat{\vec{u}}_{\mathrm{m}}^{L} + \frac{1}{2}(1-\eta)(\hat{\vec{u}}_{\mathrm{m}}^{2} - \hat{\vec{u}}_{\mathrm{m}}^{1}) + \frac{1}{2}(1+\eta)\hat{\vec{u}}_{\mathrm{m}}^{56},
\end{aligned} \tag{2.8}$$

$$\begin{aligned} \tilde{\tilde{u}}_{\mathrm{m}}^{T1} &= \tilde{\tilde{u}}_{\mathrm{m}}^{B2}, \\ \tilde{\tilde{u}}_{\mathrm{m}}^{T2} &= \tilde{\tilde{u}}_{\mathrm{m}}^{B1}, \\ \tilde{\tilde{u}}_{\mathrm{m}}^{R} &= \tilde{\tilde{u}}_{\mathrm{m}}^{L}. \end{aligned} \tag{2.9}$$

where η is the normalized out-of-plane coordinate of the congruent node pair. The tying equations are implemented in a cylindrical coordinate system by transforming the nodes to a local Cartesian coordinate system and connecting the local x, y, and z direction. A complete derivation of these equations is provided in Appendix F. In addition to the second-order equations, a first-order implementation is provided in this appendix.

2.3.2 Verification of macroscopic response and microfluctuations

To verify the implementation of the second-order framework, using the derived tying equations (2.8) and (2.9), a homogeneous curved parallelepiped-shaped unit cell is created as depicted in Figure 2.14a. The dimensions of the unit cell are chosen such that they are comparable with the dimensions of the stent RVE. Using a homogeneous unit cell, the macroscopic response can be compared to the analytical solution by using a linear-elastic isotropic material model and running the simulation with a linear-elastic solver. The engineering stress resultant $\hat{\hat{\mathbf{N}}}_{\mathrm{M}}$ is verified by applying axial strain and torsion to the model. Since no analytical solution is available for bending the curved unit cell, a planar parallelepiped unit cell, as depicted in Figure 2.14b, is used to verify the macroscopic couple-stress $\hat{\hat{\mathbf{M}}}_{\mathrm{M}}$.

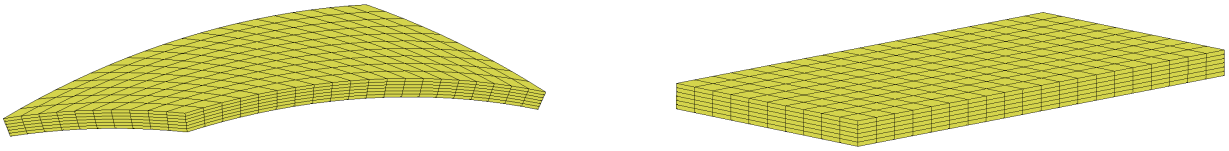

(a) Curved homogeneous parallelepiped unit cell.

(b) Planar homogeneous parallelepiped unit cell.

Figure 2.14: Two homogeneous unit cells used to verify $\hat{\hat{\mathbf{N}}}_{\mathrm{M}}$ (a) and $\hat{\hat{\mathbf{M}}}_{\mathrm{M}}$ (b). The dimensions of the curved unit cell are 3, 2, and 0.22 mm in the tangential, axial, and radial direction, respectively. The dimensions for the planar unit cell are the same, but in a Cartesian coordinate system.

A Young's modulus $E = 70$ GPa and Poisson's ratio $\nu = 0$ are chosen for the material. The prescribed deformations are an axial strain $\varepsilon_{22} = 0.1$, a torsional strain $\gamma_{12} = 0.05$, and a curvature $\kappa_{22} = 0.05$ mm^{-1}. This leads to the analytical solutions for the engineering stresses σ and reaction moment M as

$$\sigma_{22} = E\varepsilon_{22} = 70 \cdot 10^3 \cdot 0.1 = 7.0 \cdot 10^3 \text{ N/mm}^2, \tag{2.10}$$

$$\sigma_{12} = \sigma_{21} = G\gamma_{12} = \frac{E}{2+2\nu} \cdot 0.05 = 1.75 \cdot 10^3 \text{ N/mm}^2, \tag{2.11}$$

$$M = \frac{EI}{r} = EI\kappa_{22} = 70 \cdot 10^3 \cdot \frac{3 \cdot 0.22^3}{12} \cdot 0.05 = 9.32 \text{ Nmm}. \tag{2.12}$$

Note that γ_{12} is a torsional strain, related to the radius, angular twist, and unit cell length by $\gamma_{12} = \frac{r\theta}{L}$. The load cases are defined by the deformation gradient tensor $\hat{\hat{\mathbf{F}}}_{\mathrm{M}}$ and curvature tensor $\hat{\hat{\mathbf{K}}}_{\mathrm{M}}$ as shown below for the tension, torsion, and bending load case:

$$\underline{\hat{\hat{\mathbf{F}}}}_{\mathrm{M}} = \begin{bmatrix} 1 & 0 \\ 0 & 1.1 \end{bmatrix}, \quad \underline{\hat{\hat{\mathbf{K}}}}_{\mathrm{M}} = \begin{bmatrix} 0 & 0 \\ 0 & 0 \end{bmatrix}, \qquad \underline{\hat{\hat{\mathbf{F}}}}_{\mathrm{M}} = \begin{bmatrix} 1 & 0.05 \\ 0 & 1 \end{bmatrix}, \quad \underline{\hat{\hat{\mathbf{K}}}}_{\mathrm{M}} = \begin{bmatrix} 0 & 0 \\ 0 & 0 \end{bmatrix}, \qquad \underline{\hat{\hat{\mathbf{F}}}}_{\mathrm{M}} = \begin{bmatrix} 1 & 0 \\ 0 & 0.9996 \end{bmatrix}, \quad \underline{\hat{\hat{\mathbf{K}}}}_{\mathrm{M}} = \begin{bmatrix} 0 & 0 \\ 0 & 0.05 \end{bmatrix}.$$

Note that component $\hat{\hat{\underline{\mathbf{F}}}}_{\mathrm{M}(22)}$ is slightly lower than 1 for the bending load case, which is explained in more detail in appendix E. After running the simulations, the stress resultants are calculated using the expressions for $\hat{\hat{\mathbf{N}}}_{\mathrm{M}}$ and $\hat{\hat{\mathbf{M}}}_{\mathrm{M}}$ as provided in equation (2.5) and (2.6). Note that for the deformations of first-order type, only the engineering stress resultant is calculated:

$$\hat{\hat{\underline{\mathbf{N}}}}_{\mathrm{M}} = \begin{bmatrix} 0 & 0 \\ 0 & 1539.5 \end{bmatrix}, \qquad \hat{\hat{\underline{\mathbf{N}}}}_{\mathrm{M}} = \begin{bmatrix} 0.48 & 385.3 \\ 384.9 & 0.004 \end{bmatrix}, \qquad \hat{\hat{\underline{\mathbf{N}}}}_{\mathrm{M}} = \begin{bmatrix} 0.004 & 0.004 \\ 0.006 & 1.790 \end{bmatrix},$$
$$\hat{\hat{\underline{\mathbf{M}}}}_{\mathrm{M}} = \begin{bmatrix} -0.004 & -0.022 \\ -0.021 & 3.168 \end{bmatrix}.$$

Since $\hat{\hat{\underline{\mathbf{N}}}}_{\mathrm{M}}$ is integrated over the unit cell height, the analytical solutions from equation (2.10) and (2.11) should be multiplied by the height to compare them to their numerical counterparts. For tension, $7 \cdot 10^3 \cdot 0.22$ results in 1540 N/mm. For torsion, $1.75 \cdot 10^3 \cdot 0.22$ results in 385 N/mm. These analytically calculated values are in good agreement with the stress resultants found by the numerical simulations. The slight differences can be explained by discretization. For the bending case, the analytical solution of equation (2.12) should be divided by the unit cell size parallel to the bending axis to make a fair comparison. This results in $9.32/3.0 = 3.11$ N, which is close to the value of $\hat{\hat{\underline{\mathbf{M}}}}_{\mathrm{M}(22)}$. It has to be noted that, to achieve this result, simplified assumptions are made for the out-of-plane microfluctuations. This is detailed in Appendix E.

Microfluctuations

In addition to the stress resultants, the microfluctuations of the RVE are verified to ensure the tying equations are implemented correctly. Verification is done by applying deformations to the heterogeneous unit cell as depicted in Figure 2.15a. The applied deformations are $\varepsilon_{22} = 1.0$ and $\gamma_{12} = 0.25$. The large deformations are chosen on purpose, to ensure the periodicity still holds for extreme, non-linear, deformations. The microfluctuations when applying curvature are not verified, since it is known that the microfluctuations are not geometrically periodic in this load case, as explained in Appendix E.

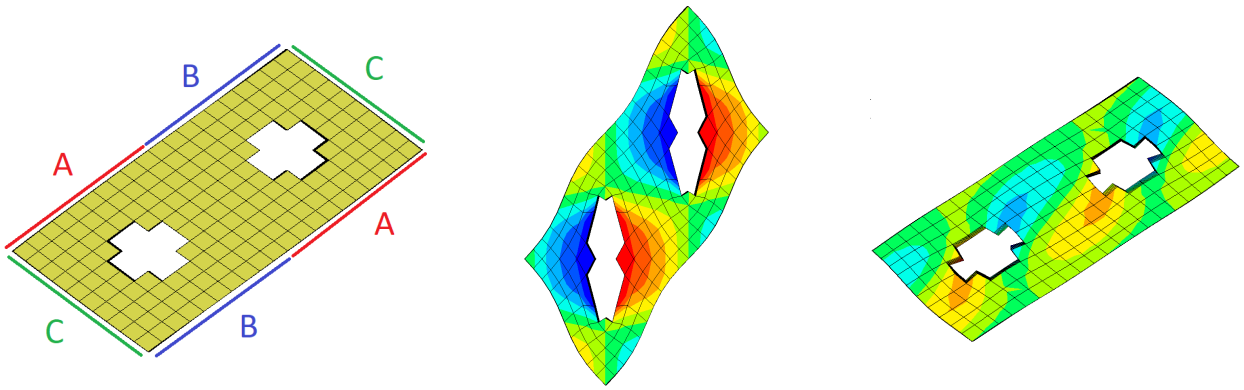

(a) Top view heterogeneous unit cell. (b) $\varepsilon_{22} = 1.0$. (c) $\gamma_{12} = 0.25$.

Figure 2.15: Top view of the curved heterogeneous parallelepiped-shaped unit cell. The connected boundaries are depicted by the matching colored lines and letters (a). The contours in (b) and (c) represent the tangential and axial displacement, respectively.

When the periodic boundary conditions are applied correctly, the microfluctuations of the corresponding sides as depicted with the colored lines in Figure 2.15a should match exactly. This is verified by plotting the microfluctuations and confirming that these are equal for all congruent nodes. An example of the microfluctuation in the tangential direction along edge 'A' of Figure 2.15a is shown in Figure 2.16.

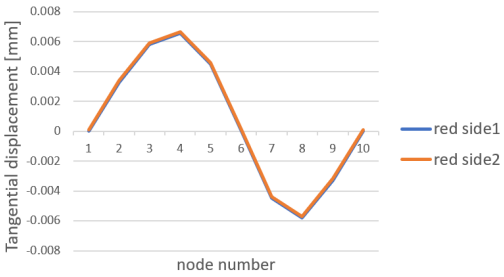

Figure 2.16: The microfluctuation in the tangential direction for an applied axial deformation $\varepsilon_{22} = 1.0$.

Since no differences in microfluctuations were observed for all DOFs, it can be concluded that brick periodicity is implemented correctly.

2.3.3 Additional macroscopic properties

To fully understand the stent's mechanics, additional properties are collected next to engineering stress resultant $\hat{\hat{\mathbf{N}}}_{\mathrm{M}}$ and couple-stress resultant $\hat{\hat{\mathbf{M}}}_{\mathrm{M}}$. An explanation of these properties and the rationale behind them are provided below.

Tensile force

For the axial elongation load case, the tensile force is calculated to compare the simulation results to tensile tests in the literature. The tensile force F is related to the axial component of the stress resultant, $\hat{\hat{\mathbf{N}}}_{\mathrm{M}(22)}$, as

$$F = n\frac{A_{\mathrm{m}}}{z_{\mathrm{m}}}\hat{\hat{\mathbf{N}}}_{\mathrm{M}(22)}. \tag{2.13}$$

The constant $\frac{A_{\mathrm{m}}}{z_{\mathrm{m}}}$ ensures that the axial component of the stress resultant is integrated correctly. The variable n is the number of clockwise stent wires, which equals the number of unit cells along the stent's circumference.

The derived equation is validated using the curved homogeneous unit cell. The analytical solution of the tensile force for one unit cell ($n = 1$) is expressed by $F = E\varepsilon_{22}A_{\mathrm{p}}$, where A_{p} is the area perpendicular to the tensile direction. The tensile force for an applied strain of $\varepsilon_{22} = 0.1$ is equal to $F = 4620$ N and $F = 4618.5$ N for the analytical and numerical solution, respectively.

Radial pressure

The radial pressure and its derivative, the radial stiffness, are important properties of the stent. These are measures of the stent's ability to keep the blood vessel open under external loading. The radial pressure should be balanced carefully. Excessive pressure can result in damage to the artery, whereas insufficient pressure might not be able to keep the blood vessel open.

In the literature, experimental studies are performed on radial stiffness by using an iris-mechanism to compress the stent [18]. Using this mechanism, the radial force of the stent can be measured, and the radial pressure and stiffness can be calculated. Besides the experimental data, a validated analytical model to calculate the stent's radial pressure exists, see Appendix A [17].

Since only in-plane boundary conditions are prescribed in the unit cell model, the reaction forces in the control nodes in the radial (out-of-plane) direction are zero by definition. A separate load case is developed that switches the constraints from the prescribed nodes $\hat{\bar{u}}_{\mathrm{m}}$ to three nodes in the unit cell mesh when the target diameter is reached. By constraining the displacement in the radial direction at these three nodes, as depicted in Figure 2.17, the reaction forces will be in the radial direction instead of in the axial direction.

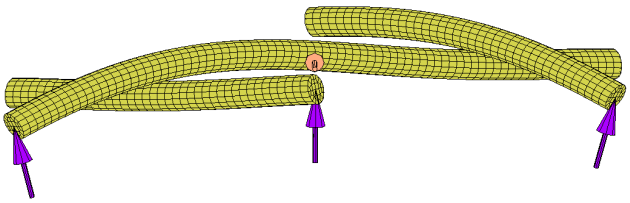

Figure 2.17: Radial constraints $u_{\mathrm{r}} = 0$, depicted by the purple arrows, applied to wire ends after axial deformation.

To find the total radial force F_{r} the stent exerts on the artery, the reaction forces f_{r} in the three unit cell nodes are summed as

$$F_{\mathrm{r}} = n\frac{L_0}{z_{\mathrm{m}}} \sum_{i=1,2,3} f_{\mathrm{r}}^i. \tag{2.14}$$

In this equation, the integer $\frac{L_0}{z_{\mathrm{m}}}$ represents the number of unit cells that fit in the undeformed stent length L_0. The constant $n\frac{L_0}{z_{\mathrm{m}}}$ is thus the total number of unit cells to create the complete stent geometry. Using the reaction force, the radial pressure can be calculated by dividing the force over the stent area as

$$P = \frac{F_{\mathrm{r}}}{\pi D L}. \tag{2.15}$$

Note that D and L are the diameter and length in the deformed configuration.

Amount of sliding

To gain more insight into the local microstructural behaviour, the amount of sliding is evaluated by comparing the displacement vectors of the stent wire nodes at the crossing point, denoted by $\vec{u}_{\mathrm{s1}}$ and $\vec{u}_{\mathrm{s2}}$. The sliding will be calculated for both crossing points in the unit cell. In the 3D solid model, the node at the center of the cross-section is selected to make an equal comparison with the beam model. The sliding vector $\vec{u}_{\mathrm{s}}$ is defined as

$$\vec{u}_{\mathrm{s}} = \vec{u}_{\mathrm{s1}} - \vec{u}_{\mathrm{s2}}. \tag{2.16}$$

2.4 Braided stent RVE, simulation approach

The curved unit cell, including all tying equations, boundary conditions, and job properties is implemented in MSC Marc/Mentat, see Figure 2.18. Two types of unit cell models are created, using hexahedral solid elements and beam elements. Because of the different element types, it is expected that the models show different microstructural behaviour. It is valuable information to map these differences and to analyze what causes them. The tying equations are implemented as in equation (2.8) and (2.9), including the brick periodicity. Rigid body modes are constrained at the center of the RVE by constraining the axial and tangential displacement. This point coincides with the origin of the local coordinate system $\{\vec{e}_1^c, \vec{e}_2^c, \vec{e}_3^c\}$, and is defined as $\{r, 0, 0\}$ in the global cylindrical coordinate system, with r the average stent radius.

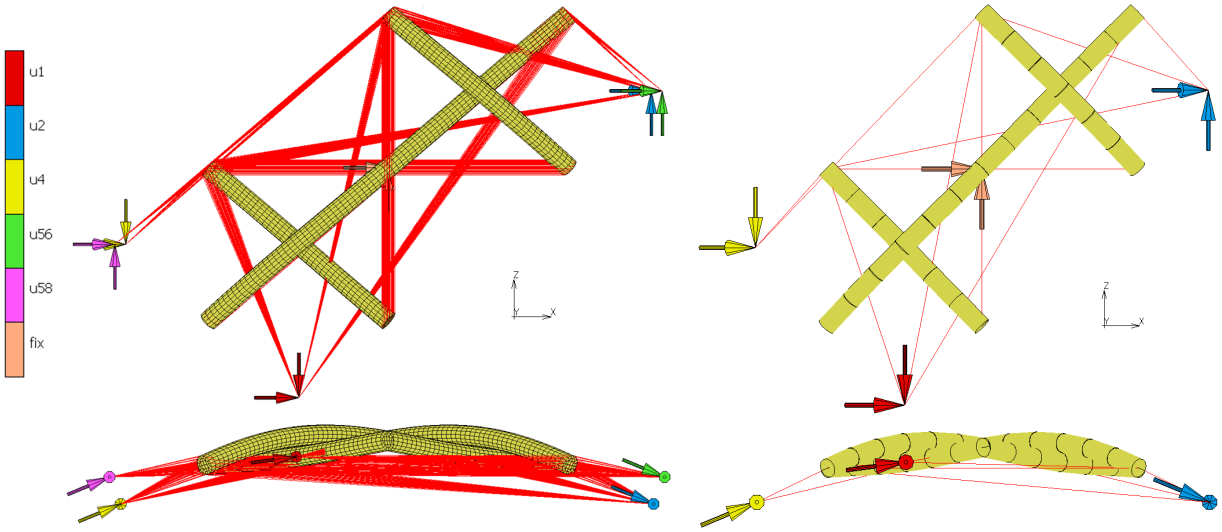

(a) Hexahedral elements.

(b) Beam elements.

Figure 2.18: Numerical implementation of the stent unit cell in MSC Marc/Mentat for solid elements (a) and beam elements (b). The five in-plane displacements that are applied to the control nodes, $\hat{\vec{u}}_1$ till $\hat{\vec{u}}_{58}$, are depicted by the colored arrows. The tying constraints (red lines) ensure equal microfluctuations and correct application of the boundary conditions. Note that for beam elements, $\hat{\vec{u}}_{56}$ and $\hat{\vec{u}}_{58}$ are not applied.

The in-plane tying equations in (2.8) are only suitable for the unit cell with 3D solid elements. Since for beam elements only one node exists at the wire ends, the curvature cannot be applied using in-plane displacements. The first-order equations, as provided in Appendix F, are implemented for the beam model. To ensure a fair comparison between the models, the first-order equations are also used for the solid model when first-order deformations are applied. Besides that, the first-order implementation has a computational time advantage over the second-order implementation. The second-order equations are only used in the case of bending. To apply curvature to the beam unit cell, rotations are prescribed at the control nodes.

Three different load cases are applied to the stent unit cell: axial deformation, torsion, and bending. Each load case is implemented as a function of time. A more detailed description of these load cases is provided in section 3. A reference stent is chosen based on stents found in the literature; its geometrical parameters are provided in the upper row of Table 3. Eight additional stents are designed with varying geometries to investigate the influence of individual parameters on the stent mechanics, as summarized in Table 3.

Table 3: The chosen stent geometries for the parameter study. The number of clockwise wires n, wire thickness t, external diameter D_e and braiding angle α are varied individually.

Stent property	L [mm]	D_e [mm]	α [deg]	t [mm]	n [-]
reference stent	60	16	45	0.25	12
large n	60	16	45	0.25	20
small n	60	16	45	0.25	4
large t	60	16	45	0.5	12
small t	60	16	45	0.1	12
large D	60	32	45	0.25	12
small D	60	4	45	0.25	12
large α	60	16	70	0.25	12
small α	60	16	20	0.25	12

Stent length L is not varied since this parameter does not influence the unit cell geometry. Besides the variation in geometrical parameters, the friction coefficient will be varied from 0 to 1 in increments of 0.2. Since the influence of the friction coefficient might depend on the geometrical properties of the stent, the friction is varied for each geometry. For example, the influence of friction might be more significant with a larger wire diameter t.

Furthermore, the difference between an elastic isotropic material and the non-linear nitinol material will be investigated. Unfortunately, it is not possible to apply the nitinol material model to beam elements in MSC Marc/Mentat. An elastoplastic material model with plastic deformation at a Von Mises stress of 366 MPa will be used instead, unless otherwise specified. This value is comparable with the start of the phase transformation in the nitinol model, $\sigma_s^{AS} = 366$ MPa. The linear material is defined with a Young's modulus of 42.1 GPa, corresponding with the modulus of austenite. Whether the phase transformation from austenite to martensite takes place, depends on the stress and strain values in the stent. Since these values depend on the stent's geometry, the comparison between nitinol and the elastic material is done for each design.

Beam models in the literature typically use either the join or the weave method, where the join method prescribes a hinge at the crossover point, and the weave method prescribes interwire contact, as explained in section 1. The difference between these methods is investigated for the unit cell, both for the solid model as for the beam model. The hinge for the join method is prescribed using an RBE2 link, constraining the total distance between two nodes, see Figure 2.19. Using this link type, rigid body rotation is still possible, which would not be the case when tying the individual DOFs. Note that this approach differs from the approach typically used in the literature, where the weaving of the wires is usually neglected. In this approach, the geometry is the exact same as in the weave method, only sliding is constrained.

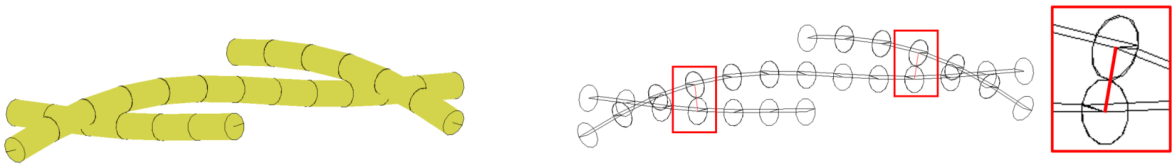

(a) (b)

Figure 2.19: The unit cell using beam elements (a). A schematic of the implementation of RBE2 links in the beam model at the wire crossing points (b), constraining relative displacement of the nodes. Relative rotation is allowed, creating a hinge mechanism.

2.5 Semi-periodic models

So far, only explicit numerical solvers have been able to solve the deformation of a full-scale stent model. Implicit solvers have not been able to solve this, especially due to the high number of contact points in a full-scale stent model. Two models are proposed, which aim to replicate the behaviour of a full-scale stent by modelling one slice of the stent. In these models, periodicity is applied in either the axial or tangential direction, whereas in the other direction the full geometry is modeled. This is referred to as semi-periodic. Since the number of contact points is less in this type of model, it might be possible to run the simulation using an implicit solver. The implicit solver is expected to have an advantage in computational time compared to the explicit solver, which is a desired improvement. Besides investigating the possibility of using an implicit solver, local microstructural behaviour in a bent configuration can be investigated, without the side effects caused by the brick periodicity.

2.5.1 Tangentially periodic model

A tangentially periodic model is created, modeling multiple unit cells in the axial direction, see Figure 2.20. Only deformations that are repetitive in the tangential direction can be simulated with this model. It is expected that the fish mouthing effect can be captured.

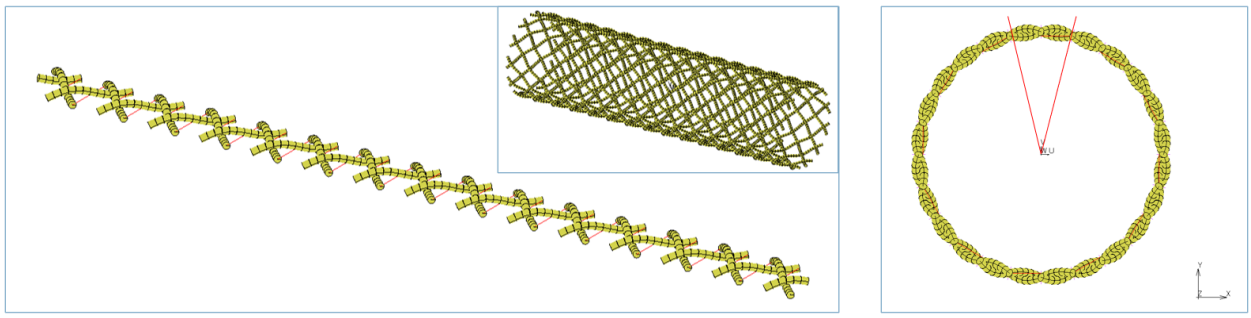

Figure 2.20: A tangentially periodic slice of a full-scale stent using beam elements.

The model is created by repeating the unit cell in the axial direction $\frac{L_0}{z_m}$ times, where z_m is the unit cell size in the axial direction. In the tangential direction, periodicity is applied by nodal ties, tying all six degrees of freedom. Simplified assumptions are made on the boundary conditions, constraining the model in the tangential direction at all wire ends. This is done to investigate the ability of the model to capture the fish mouthing effect in the most computationally efficient manner. For the same reason, only beam elements are used. The model, including boundary conditions, is depicted in Figure 2.21.

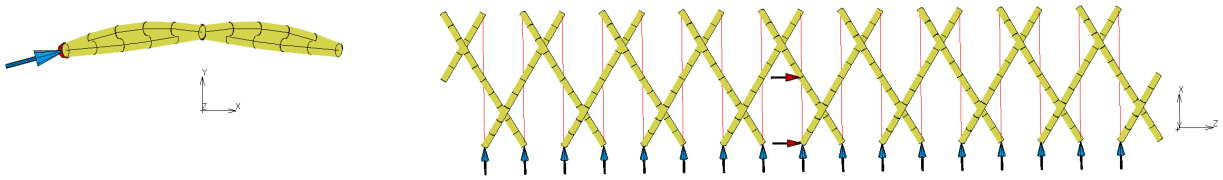

Figure 2.21: Side view (left) and top view (right) of the proposed tangentially periodic model. Displacement is constrained in the axial direction at the center (red arrows) and in the tangential direction along the length (blue arrows). Tangential periodicity is implemented by nodal ties, connecting all six degrees of freedom (red lines).

2.5.2 Axially periodic model

In addition to the tangentially periodic model, an axially periodic model is developed. This model is developed to study the behaviour when applying localized, tangentially nonperiodic deformations. Since the model is periodic in the axial direction, only axially periodic deformations can be applied. The proposed model is a slice of the full-scale stent, see Figure 2.22.

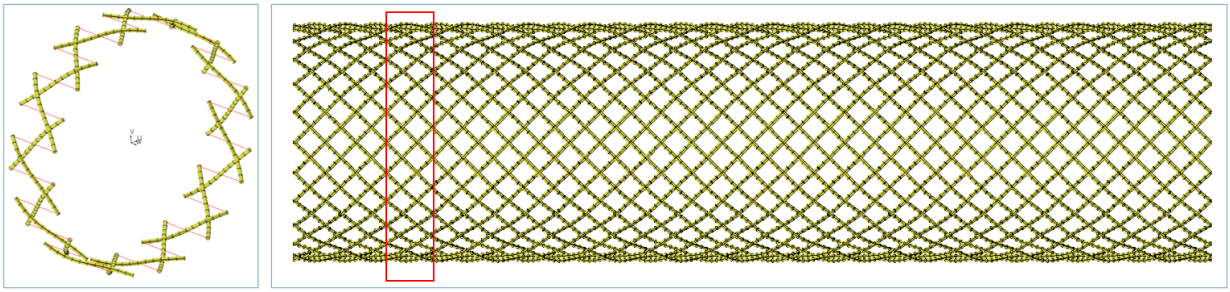

Figure 2.22: An axially periodic slice of a full-scale stent using beam elements.

The model is created by repeating the unit cell n times in the tangential direction. Two models are created, using solid or beam elements, to investigate whether different behaviour occurs when using different element types. Simplified assumptions are made for the boundary conditions, constraining the axial displacement in each wire to achieve convergence for the solid model. Nodal ties are applied in the axial direction to ensure periodicity, see Figure 2.23.

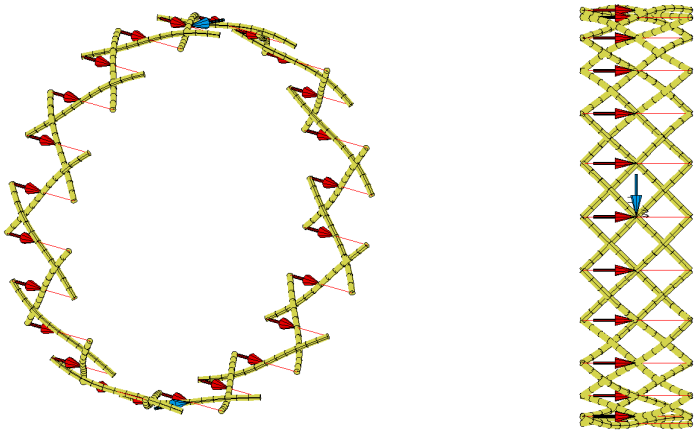

Figure 2.23: Trimetric view (left) and top view (right) of the proposed axially periodic model. Tangential displacement is constrained at two nodes (blue arrow), whereas axial displacement is constrained at all wires (red arrows). Periodicity in the axial direction is implemented by nodal ties (red lines).

3 Numerical simulations and results

In this chapter, a selection of the simulation outcomes is provided and discussed. All results provided are for the reference stent geometry unless stated differently. For example, the results on the axial deformation load case are for the stent with thicker wires, since the results are more interesting than for the reference stent. A brief motivation and explanation of each applied load case are provided, after which the results are shown and discussed.

In each load case, four different models are used for the simulation. An overview is provided in Table 4. The reference model consists of solid elements, a contact description at the wire crossings, and a linear material model. For each of the other models used, either the element type, description at the wire crossings, or the material model is varied. From now on, these models are referred to as the reference model, beam model, hinge model, and nitinol model. In case a different combination is used, e.g. beam elements and a hinge, this is mentioned in the text explicitly.

Table 4: Overview of the models used for the simulations.

model name	**element type**	**wire crossings**	**material model**
'reference model'	hexahedral	contact	linear-elastic / elastoplastic*
'beam model'	beam	contact	linear-elastic / elastoplastic*
'hinge model'	hexahedral	hinge	linear-elastic
'nitinol model'	hexahedral	contact	Auricchio shape-memory

* The elastoplastic material model is only used for the comparison between the reference model and the beam model to investigate the ability of the beam model to capture the mechanical behaviour when a non-linear material model is used. Using the Auricchio model is not possible for beam elements. Which material model is used is stated in the text explicitly.

3.1 RVE simulations

3.1.1 Axial elongation

Axial elongation is essential to compress the stent in the catheter. In this load case, the stent is elongated to the length at which the minimum stent diameter is reached. This maximum elongation, $\varepsilon_{\max}$, is calculated using the analytical expressions by Jedwab and Clerc, as described in Appendix A [17]. For the 'large t' stent geometry in Table 3, the maximum axial elongation is $\varepsilon_{22} = 0.408$. The boundary conditions to apply this deformation to are provided in Table 5. Since axial elongation is a first-order deformation, the first-order tying equations are used, using only three in-plane displacements instead of five. The deformation gradient tensor is defined as

$$\underline{\hat{\mathbf{F}}}_{\mathrm{M}} = \begin{bmatrix} 1 & 0 \\ 0 & 1.408 \end{bmatrix}. \tag{3.1}$$

Table 5: Applied boundary conditions corresponding to the generalized strain $\varepsilon_{22} = 0.408$ for the 'large t' stent.

	y [mm]	z [mm]
$\hat{\vec{u}}^1_{\mathrm{m}}$	0	-1.2017
$\hat{\vec{u}}^2_{\mathrm{m}}$	0	0.4006
$\hat{\vec{u}}^4_{\mathrm{m}}$	0	-0.4006

When applying the load case as described, using equation (A.15) in Appendix A to calculate $\varepsilon_{\max}$, mechanical locking of the wires is observed. This locking results in excessively high forces for $\varepsilon_{22} > 0.37$, as depicted in Figure 3.1. Requiring high loads is undesirable in a practical situation since the force to compress the stent in a catheter has to be excessively high in this case.

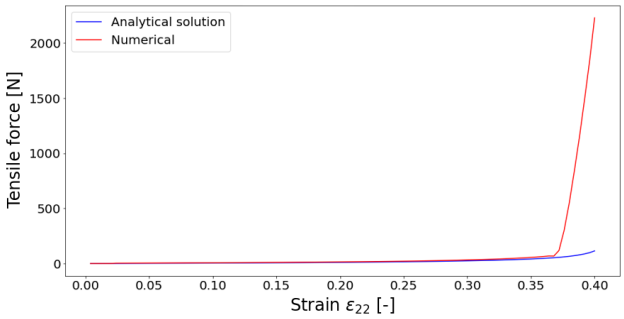

Figure 3.1: Tensile force, $\varepsilon_{\max} = 0.408$.

When investigating the cause of this locking phenomenon, it turns out that the interwire contact points change at a certain diameter, depicted in red in Figure 3.2. This happens before the theoretically minimum diameter, which for this stent is 1.92 mm at an elongation of $\varepsilon = 0.408$.

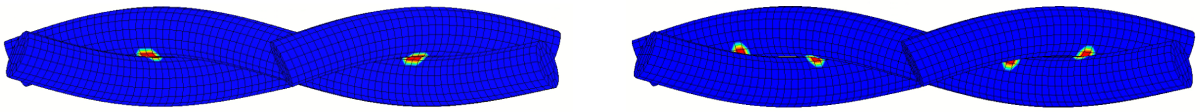

(a) $D = 6.3$mm, $\varepsilon_{22} = 0.35$.

(b) $D = 4.6$mm, $\varepsilon_{22} = 0.38$.

Figure 3.2: Side view of the stent unit cell loaded in the axial direction before locking (a) and after locking (b). The colors depict the contact status.

It can be concluded that the reference model, which uses solid elements, can be used to find the minimum stent diameter before locking, which is valuable information when designing the catheter for the stent. Compared to finding this diameter by simulation of a full-scale beam model, this unit cell model shows more detail on the local microstructural behaviour. Studying this detailed information would not have been possible with a full-scale beam model. Further, this method has an advantage in computational time; simulation of the reference model takes 2 minutes, compared to $\pm$ 1 hour for the full-scale beam model.

For the comparison between the reference model and beam model, the axial elongation is limited to the point where 95% of the maximum diameter reduction is reached. This maximum reduction is the diameter where the locking occurs, which is determined by the simulation. The resulting tensile force, both for the beam model and the reference model, is depicted in Figure 3.3a. Since the stress in this simulation does not exceed 366 MPa, a yield stress of 100 MPa is selected for the elastoplastic material model. The differences between the analytical model, reference model, and beam model are depicted in Figure 3.3b.

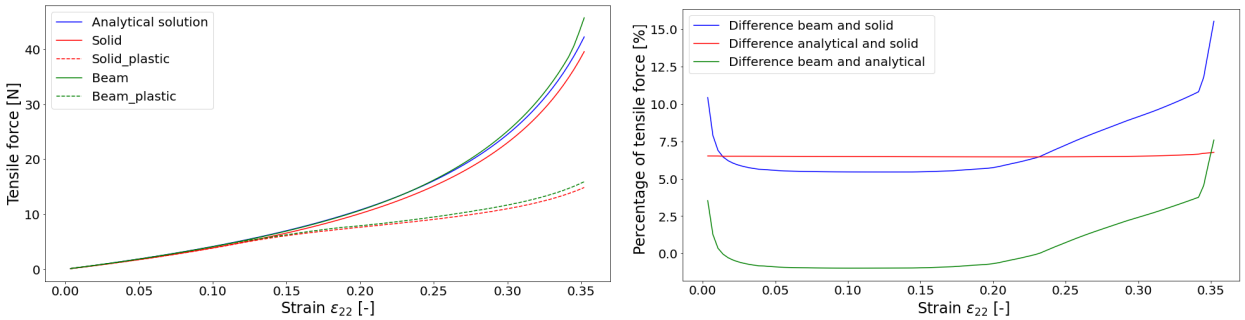

(a)

(b)

Figure 3.3: The resulting tensile force for a maximum strain of $\varepsilon_{22} = 0.352$ (a). The difference in tensile force between the methods (b).

As can be observed from Figure 3.3b, the relative difference between the analytical model and the reference model, is around 6.5% for all increments. Similar results are obtained for the radial force. This result means the analytical solution overestimates the stiffness of the stent compared to the reference model. The analytical model neglects the weaving of the wires and describes the stent as perfect cylindrical springs in parallel, which are expected to be stiffer than cylindrical springs with a weave in them. Hence, it is logical that the analytical model overestimates the stiffness. This theory is also consistent with the fact that for the reference stent with thinner wires, where D/t is larger and the 'waviness' is less, the difference between the analytical and numerical solution is only 3%.

When looking at the difference between the beam model and the reference model for the linear material, the beam model also overestimates the reference model by at least 5.4%. For the non-linear material, similar results are obtained: the average difference is 5.5%, and the largest offset is 7.1%. The source of the larger difference at low strains is not further investigated. Interestingly, for the linear material, the difference starts to increase around a strain of 0.20. In addition, the beam model even overestimates the analytical model at high elongations. To investigate whether these phenomena depend on element size, the beam model mesh is refined, using 24 beam elements per wire instead of 12. The result is depicted in Figure 3.4.

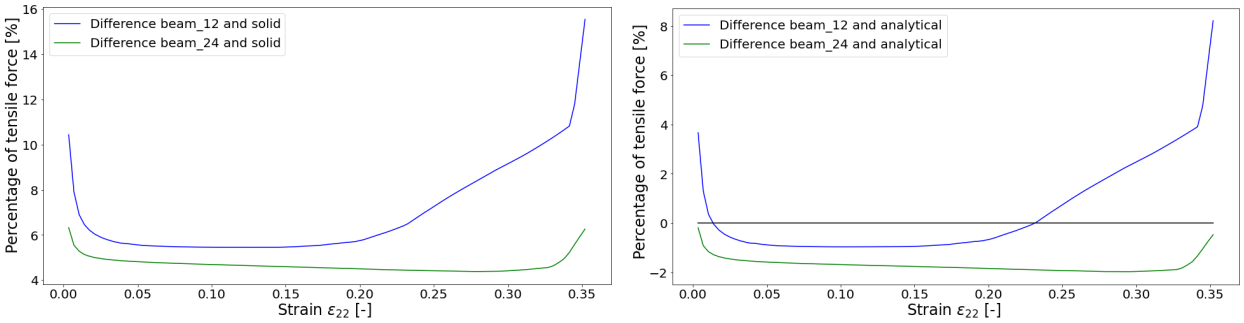

(a) (b)

Figure 3.4: The difference in tensile force compared to the reference model (a) and the analytical solution (b) for both beam models, using 12 and 24 elements per wire respectively.

When looking at Figure 3.4a, it can be concluded that the refined mesh has a smaller difference to the reference model. Further, the increased difference after a strain of 0.2 is notably reduced for the refined model, leaving just a minor increase after a strain of 0.33. Hence, there is a locking mechanism if the beam element mesh is not fine enough. When comparing the beam model to the analytical solution in Figure 3.4b, the refined beam model provides a lower response for all increments, which is expected. The refined beam model also does not overestimate the analytical solution anymore at high elongations.

The results show that the unit cell can be used to determine the number of beam elements that should be used for a certain stent geometry. In addition, the accuracy of using beam elements instead of solid elements for an axial elongation load case can be judged by investigating the simulation results.

When comparing the reference model and the hinge model, a perfect match is observed, see Figure 3.5a. When using beam elements in combination with the hinge, more significant offsets were observed, as depicted in Figure 3.5b. Again, a locking mechanism is observed when using the unrefined beam model, leading to excessively high forces at high elongations. When using the refined model with 24 beam elements, the locking is not present anymore.

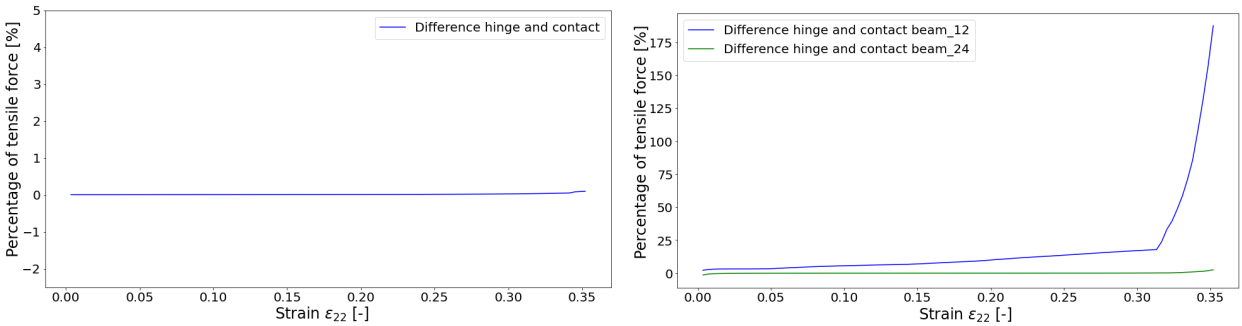

(a) Solid elements.

(b) Beam elements.

Figure 3.5: The difference in tensile force between the hinge and contact description for the solid model (a) and the beam model (b).

Furthermore, the amount of sliding and the effect of the friction coefficient are investigated. The amount of sliding is negligible in this load case; the same holds for the amount of friction. This is consistent with the perfect match between the contact and hinge model. When there is no sliding, the hinge model can perfectly describe the stent mechanics.

3.1.2 Torsion

In the literature, not many studies have focused on torsional stiffness. This is partially because it is complex to apply torsion to a braided stent in an experimental setting. Recently, it has been demonstrated that the torsional stiffness of a braided stent is high compared to its axial stiffness [34]. In this load case, a torsional strain of $\varepsilon_{12} = 0.05$ is applied. Next, the loading is reversed to return to the undeformed configuration. The boundary conditions to apply this deformation to the reference stent are provided in Table 6. The deformation gradient tensor is defined as

$$\hat{\underline{\mathbf{F}}}_{\mathrm{M}} = \begin{bmatrix} 1 & 0.05 \\ 0 & 1 \end{bmatrix}. \tag{3.2}$$

Table 6: Applied boundary conditions corresponding to the generalized strain $\varepsilon_{12} = 0.05$ for the reference stent.

	y [mm]	z [mm]
$\hat{\vec{u}}^1_{\mathrm{m}}$	-0.15217	0
$\hat{\vec{u}}^2_{\mathrm{m}}$	0.05072	0
$\hat{\vec{u}}^4_{\mathrm{m}}$	-0.05072	0

In Figure 3.6a, the deformed configuration of the reference model is depicted. When looking at the undeformed wire ends compared to the deformed geometry, it can be observed that the stent moves downwards. In this figure, the direction downwards is equivalent to a reduction in stent diameter. This diameter reduction is also observed in experimental results in the literature [34]. Further, it can be observed that one crossing point separates, whereas the other is pushed together. When looking at the individual wires, the wire without the blue regions is elongated, while the other two are compressed.

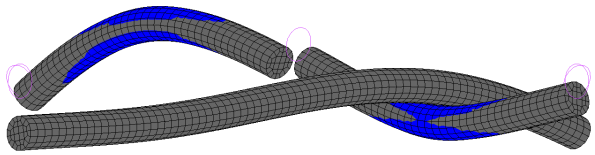

(a) Deformed unit cell under torsional load.

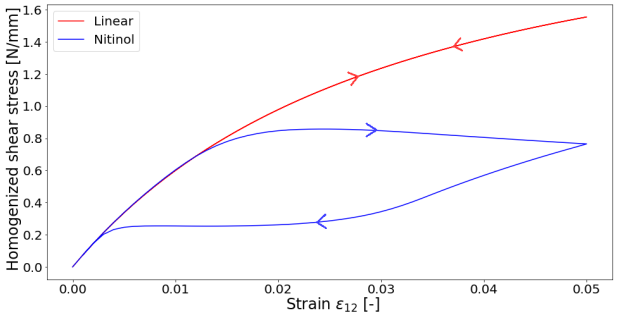

(b) Homogenized response of the unit cell.

Figure 3.6: The deformed unit cell under a torsional strain of $\varepsilon_{12} = 0.05$. Regions with $\sigma_{vm} > 366$ MPa are depicted in blue. The location of the undeformed wire ends are depicted as purple circles (a). Component $\hat{\underline{\mathbf{N}}}_{\mathrm{M}(12)}$ of the homogenized response of the RVE for a linear and nitinol material model as a function of the applied shear (b).

The compressed wire shows Von Mises stresses (σ_{vm}) above 366 MPa in the regions depicted in blue, which is the transformation stress of nitinol. When comparing the simulation using the reference model and the nitinol model, the homogenized response as depicted in Figure 3.6b is found. As can be observed, the loading and unloading curve is the exact same for the linear material. For the nitinol material, a hysteresis loop is observed, corresponding with the material model provided in section 2.1.

Besides the comparison between the material models, a comparison between solid and beam elements is made. The result is shown in Figure 3.7a. Further, the difference between the reference and the hinge model is investigated, see Figure 3.7b.

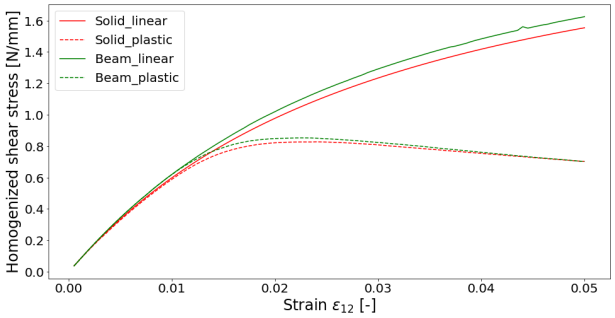

(a) Response of the reference model and beam model.

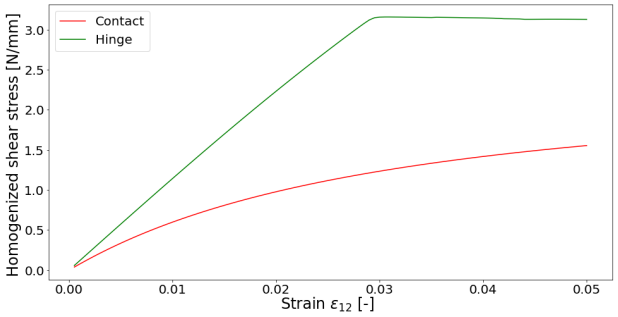

(b) Response of the reference model and hinge model.

Figure 3.7: The component $\hat{\underline{\mathbf{N}}}_{\mathrm{M}(12)}$ of the homogenized response as a function of the applied torsion for the beam model as compared to the reference model (a), and for the reference model and the hinge model (b).

As can be observed, the beam model closely matches the reference model; the maximum difference is 4.5% for the linear material and 5.2% for the non-linear material. Between the contact and the hinge model, a significant difference is observed. Since the hinge prevents the wires from separating, which happens in the reference model, it makes sense that the stent unit cell with the hinge is stiffer. In addition, the homogenized stress does not increase any more after a torsional strain of 0.03 for the hinge model. In the simulation, this corresponds to a buckling mode.

It can be concluded that the reference model provides detailed information on the microstructural behaviour for this load case. The local austenite to martensite transition is clearly visible. Whether the obtained kinematics and homogenized stress values do match reality should be validated by experiments. Furthermore, it can be concluded that the beam model can accurately describe torsion, both for a linear and non-linear material model. Further, it can be concluded that the hinge model is not able to describe torsion accurately.

3.1.3 Bending

As explained in section 2.3.1, bending of the unit cell is possible, but the significance of by-products in the stent unit cell remains uncertain. In the bending load case considered, bending in one direction will be applied. Only the κ_{22} component of the curvature tensor $\hat{\hat{\mathbf{K}}}_{\mathrm{M}}$ will be non-zero. Its chosen to focus on this curvature since it is comparable with the deformations shown at the stent ends in the fish mouthing effect. The κ_{12} and κ_{21} components are 0, so no twisting is prescribed. Since the significance of side effects increases with the curvature as shown in Appendix E, the applied curvature is limited to $\kappa_{22} = 0.05$. The boundary conditions to apply this deformation to the reference stent are provided in Table 7. The applied deformation gradient tensor, where the $\underline{\hat{\hat{\mathbf{F}}}}_{\mathrm{M}(22)}$ component is slightly lower than 1 as explained in Appendix E, and curvature tensor for the bending case are defined as

$$\underline{\hat{\hat{\mathbf{F}}}}_{\mathrm{M}} = \begin{bmatrix} 1 & 0 \\ 0 & 0.9983 \end{bmatrix}, \qquad \underline{\hat{\hat{\mathbf{K}}}}_{\mathrm{M}} = \begin{bmatrix} 0 & 0 \\ 0 & 0.05 \end{bmatrix}. \tag{3.3}$$

Table 7: The boundary conditions to apply curvature $\kappa_{22} = 0.05$.

	y [mm]	z [mm]
$\vec{u}_1$	0	0.0242
$\vec{u}_2$	0	-0.0081
$\vec{u}_4$	0	0.0081
$\vec{u}_{56}$	0	0.0183
$\vec{u}_{58}$	0	0.0091

In Figure 3.8a, the deformed mesh of the stent is depicted. As can be observed, the stresses are the highest at the wire ends. Hence, edge effects are, unfortunately, definitely present. When looking at the strains, neglecting the strains at the wire ends, positive and negative strains are observed at the wire's top and bottom side, respectively. This is as expected when bending is applied. When looking at the deformation compared to the undeformed wire ends, the wire ends in the middle move upwards, and the ends at the left and right side downwards, which is also as expected.

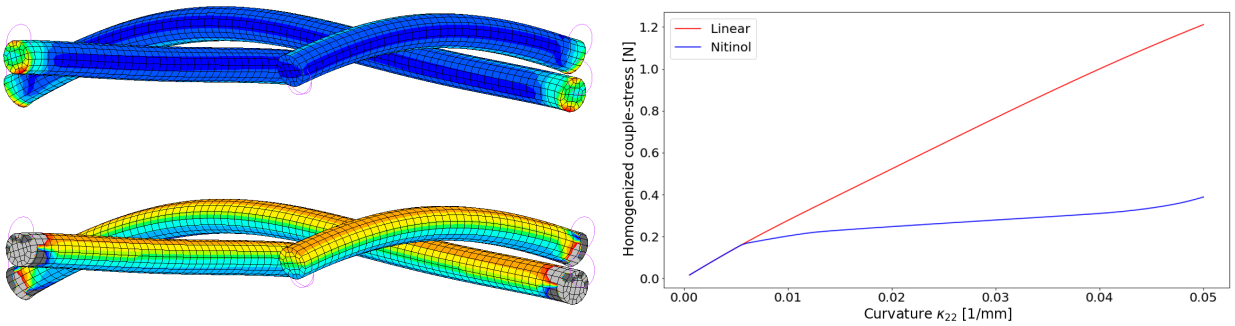

(a) The deformed unit cell under bending load.

(b) Response to bending for linear and nitinol material.

Figure 3.8: The deformed unit cell with an applied curvature $\kappa_{22} = 0.05$. The contours depict the Von Mises stress (top) and major strain value, neglecting the strains at the wire ends (bottom). The undeformed wire ends are depicted as purple circles (a). The $\underline{\hat{\hat{\mathbf{M}}}}_{\mathrm{M}(22)}$ component of the homogenized response as a function of the applied curvature for a linear and nitinol material model.

To investigate the severity of the by-products, the reference model is compared with the nitinol model. Since the stresses only exceed the transformation stress of 366 Mpa at the wire ends, all the difference in the results is due to the edge effects. As can be observed from Figure 3.8b, the difference is high, and edge effects do, unfortunately, dominate the solution.

Since the source of the edge effects is in the tying equations, as explained in Appendix E, simplified assumptions are made on these equations to reduce the effects. This is done by removing the out-of-plane equations, as provided in equation (2.9), for all nodes, except for the nodes in the centre of the wire ends. By doing this, the out-of-plane displacement of the wire ends as a whole is periodic, but microfluctuations are not connected, and thus neglected. The result is provided in Figure 3.9b.

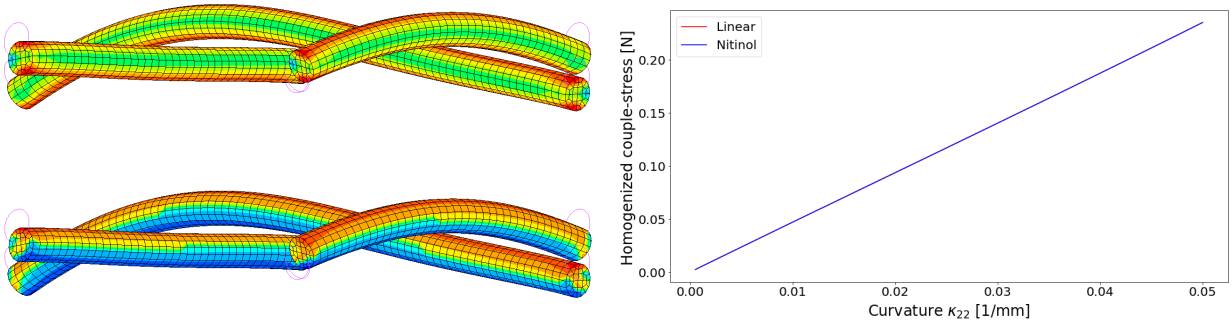

(a) The deformed unit cell under bending load.

(b) Response to bending for linear and nitinol material.

Figure 3.9: The result for the unit cell neglecting the out-of-plane microfluctuations.

When prescribing the updated tying equations, no local stress and strain concentrations are observed at the wire ends. When comparing the reference and nitinol model, an exact match is observed. The homogenized stress resultant decreased significantly for the updated tying equations, from 1.21 N to 0.24 N at a curvature of 0.05 mm^{-1}. The unrealistic stiffness created as a by-product by the out-of-plane constraints does not influence the solution anymore in the updated simulation. Regarding the kinematics, the unit cell deforms the same as with the previous tying equations. Since the maximum stress in the simulation is 340 MPa, transformation is not happening. Therefore, Figure 3.9b shows an exact match between nitinol and the linear material. Using this updated model, comparisons are made between the reference and the hinge model, and solid and beam elements, see Figure 3.10a and 3.10b.

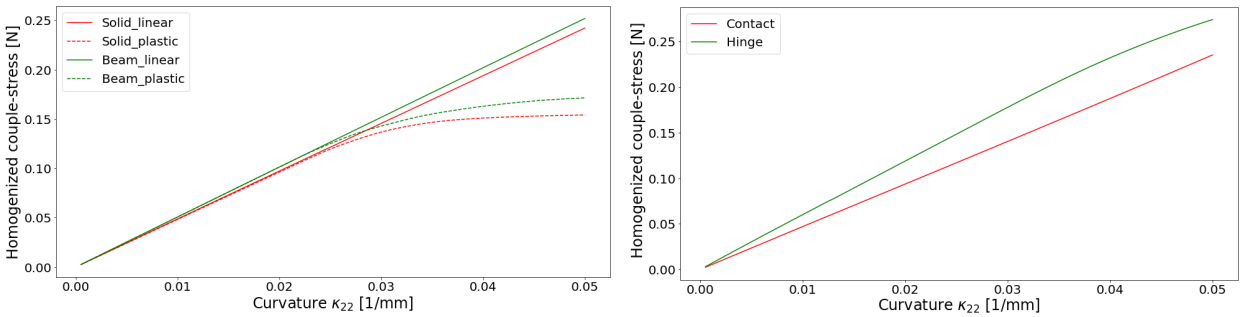

(a)

(b)

Figure 3.10: The component $\underline{\hat{\mathbf{M}}}_{\mathrm{M}(22)}$ of the homogenized response to the applied curvature for the beam model and the reference model (a), and for the reference model and the hinge model (b).

For the non-linear material used to obtain the results in Figure 3.10a, plastic deformation at $\sigma_{vm} = 70$ MPa is prescribed. The difference between the reference and beam model at a curvature of $\kappa = 0.05$ is 11% for the non-linear material, compared to 4% for the linear material. It can be concluded that for a linear material, the beam model can capture the bending mechanics. For the non-linear material, reduced performance is observed when the plastic deformation starts contributing.

From Figure 3.10b it can be concluded that the hinge model differs significantly from the reference model; the homogenized couple-stress is 17% higher at a curvature of 0.05. Since the hinge model prevents sliding at the crossing points, this is stiffening the unit cell. When looking at the amount of sliding $\vec{u}_{\mathrm{s}}$ in both

crossing points in the reference model, sliding indeed occurs. For both crossing points, the absolute values in each direction are $[0.0012, 0.0255, 0.0405]$ and $[0.0006, 0.0251, 0.0407]$ respectively, expressed in cylindrical coordinates $\{r, \theta, z\}$. Since the wires constrain each other in the radial direction, most of the sliding is in the tangential and axial direction.

3.2 Semi-periodic model simulations

3.2.1 Radial compression

Radial compression is applied to the tangentially periodic model, reducing the diameter to 50% of the undeformed diameter, $D = 0.5D_0$. An undeformable solid body is used to compress the stent, representing the catheter wall. Since an iris mechanism with eight flat surfaces is used in experiments to compress the stent, it is chosen to use a flat solid body [18]. In the practical situation of compression in a catheter, the compressing body is of circular shape.

Frictionless contact between the wires and the catheter wall is prescribed. For interwire friction, a friction coefficient of 0.2 is prescribed. Only beam elements are used for this load case. Besides investigating the fish mouthing effect, observing whether it can be captured using this implicit solver, the difference between prescribing a hinge and contact at the crossing points is investigated. The starting configuration of the simulation is depicted in Figure 3.11.

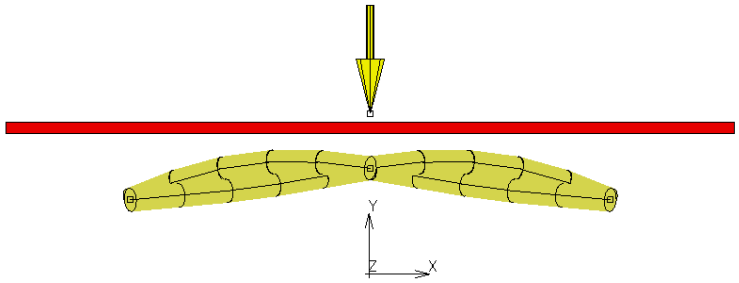

Figure 3.11: Side view of the starting configuration of the radial compression simulation.

To verify the ability of the model to capture the fish mouthing effect, the result is compared with the literature. Fu et al. expressed the fish mouthing effect in a minimum and maximum radial deformation ΔD_{min} and ΔD_{max}, where the minimum reduction is at the centre of the stent, and the maximum reduction at the stent ends [14]. The same deformation is applied to the semi-periodic model, using the same geometrical parameters as Fu et al., resulting in the deformation as shown in Figure 3.12.

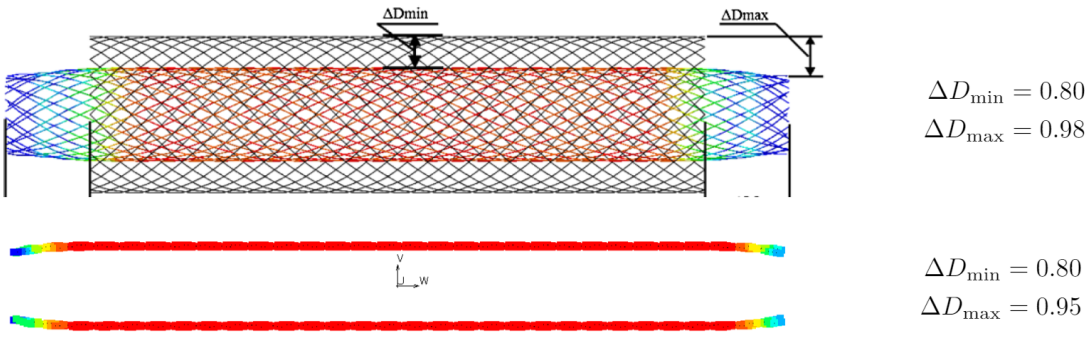

Figure 3.12: The fish mouthing effect demonstrated and quantified by Fu et al. (top) [14]. The fish mouthing effect by the semi-periodic beam model in MSC Marc/Mentat (botttom). The mesh is copied and rotated around the z-axis by 180° for visualization purposes. The colors depict the displacement in the radial direction.

As shown in Figure 3.12, the deformation of the developed model at the stent ends is in the same order of magnitude as that of the full-scale beam model in the literature, 0.98 mm compared to 0.95 mm. Since the model by Fu et al. is not described in detail, the difference might be caused by a difference in boundary conditions, or by discretization effects.

Regarding the hinge and contact description for the reference stent, both models showed similar results. The same radial deformation at the stent's ends was observed, with $\Delta D_{\max} = 4.8$ mm and 4.9 mm for the contact and hinge model respectively, see Figure 3.13a. Note that here, the reference geometry is used as provided in Table 3, using a stent diameter of 16 mm. The minimum radial deformation, $\Delta D_{\min}$, is 3.875 mm in this load case. Whereas the radial deformation is the same for both models, the underlying mechanics to achieve this deformation are different. For the contact description, sliding occurs at the end of the stent, whereas for the hinge model, the radial deformation is obtained without sliding. The difference in deformation is depicted in Figure 3.13b. Instead of sliding, the diameter reduction is achieved by an increased torsional rotation of the wires. This results in a torsional moment in the wires that is 50% higher for the hinge than for the contact description.

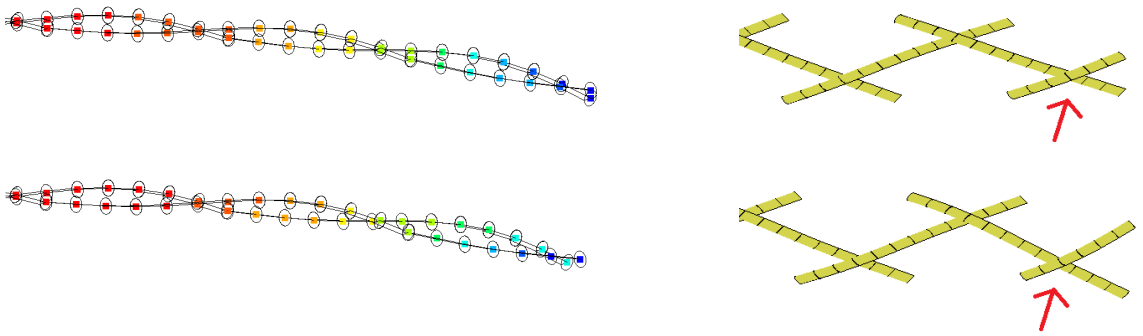

(a) (b)

Figure 3.13: Side view (a) and top view (b) of the deformed wire ends for the hinge description (top) and contact description (bottom). The colors in (a) depict the displacement in radial direction.

The results on the semi-periodic model show the potential of using this type of model instead of a full-scale beam model to capture the fish mouthing effect. The computational time advantage is significant, with 5 minutes for the semi-periodic model, compared to $\pm$ 1 hour for the full-scale model. The comparison with Fu et al. shows that this type of model, for this specific geometry, can capture the fish mouthing effect rather accurately. However, it is too early to conclude that this is generally true.

The ability of the hinge model to capture the fish mouthing is surprising, especially since Kim et al. have shown that the join method is not able to capture the effect accurately [19], see also Figure 1.3 in the introduction of this report. The difference between the methods, neglecting the weaving of the wires, likely causes the difference. The simulation is repeated for a join method model of the reference stent to investigate this, neglecting the weaving of the wires. The maximum radial deformation, $\Delta D_{\max}$, was 4.3 mm in this case, which is less than the 4.9 mm for the hinge model.

3.2.2 Indentation

Indentation by an undeformable cylindrical-shaped body is simulated for the axially periodic model, indenting the stent locally. This load case is chosen to investigate the behaviour of solid and beam elements in a more complex load case than for the unit cell. In a practical, in vivo situation, this load case can be compared with indentation by an adjacent blood vessel or a muscle. The diameter of the stent is 16 mm. The resulting deformation for an indentation of 5.5 mm is depicted in Figure 3.14.

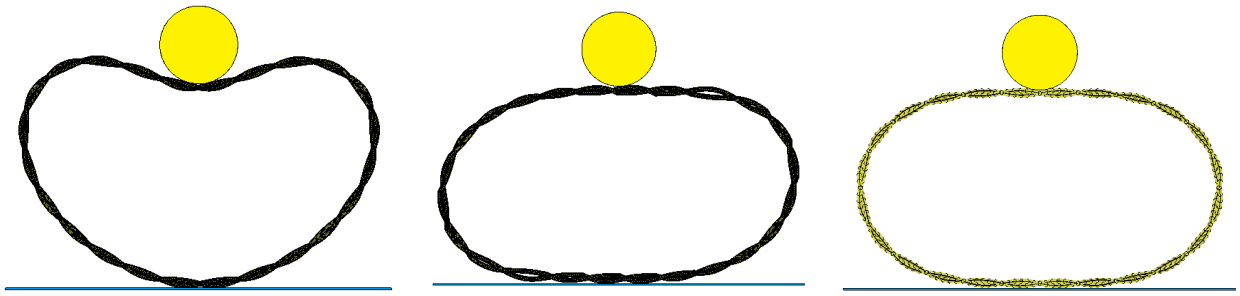

(a) (b) (c)

Figure 3.14: The deformed axially periodic model using solid elements constraining individual nodes (a) and constraining centre nodes using nodal ties (b). The deformed model using beam elements (c).

As can be observed, the deformation of the beam model differs significantly from the model in Figure 3.14a, which uses solid elements. A more thorough investigation showed that the source of this different behaviour is in the applied boundary conditions. In the solid model, each node on the wire end is tied to its congruent node on the opposite side, constraining all three translational DOFs. In the beam model, the periodicity is applied by constraining the node at the wire ends centre to the opposite side, constraining all six DOFs. When the latter tying method is applied to the solid model, the deformations are in good agreement. It is unclear why constraining each congruent node pair results in different deformation than constraining six DOFs for the centre node. Further research is required to investigate this.

3.3 Discussion of results

Three different load cases, axial elongation, torsion, and bending, have been studied in-depth to understand the microstructural behaviour of a braided stent. In addition to the three load cases, combinations of load cases have been studied, but did not result in new insights. Based on the performed studies, conclusions can be drawn on using beam elements instead of solid elements, using the contact or hinge description, and the differences using a linear or non-linear material model.

Regarding the use of beams compared to solid elements, good performance is observed for the beam elements. The largest difference between the models was 11% for the bending load case and a non-linear material model. For the other load cases, the deviations were around 5%. The 11% is not negligible. However, this difference is still considered acceptable, especially considering the advantage in computational time compared to the reference model. The only case where the results of beams differed significantly from solid elements was for indentation of the axially periodic model. Further research should clarify whether beam elements fall short in this more complex load case.

When comparing the results on the hinge and contact description, notable differences were observed. For a simple load case where little to no sliding occurs, such as axial elongation, the hinge model has proven to capture the mechanics accurately. However, for more complex load cases, the hinge model shows significant differences. For the torsion load case, the hinge model prevents separation of the wires, which results in stiffening of the stent. This results in totally different microstructural behaviour as in the reference model. This stiffening is also observed when applying curvature, where the hinge model overestimates the bending stiffness by 17%. For the reasons above, it is recommended to use a contact description to capture the mechanics accurately.

Looking at the comparison between a linear and non-linear material model, the non-linear shape-memory model shows enhanced detail at the microscale. Especially the local transformation of austenite to martensite and vice-versa when applying torsion is an exemplary case that shows the benefits of using the shape-memory material model. When using a non-linear model in combination with beam elements, similar performance as for the linear model is observed. Reduced performance is observed for the bending load case, but the differences are considered acceptable. Since it was not possible to apply the Auricchio shape-memory model to beam elements, it is recommended to verify its use with a different software package.

4 Conclusions and outlook

To improve healthcare and personalize stent placement interventions, a fundamental understanding of the mechanical behaviour of braided stents is essential. In this thesis, a detailed single-scale unit cell model to study this behaviour has been developed successfully. The results obtained with the unit cell are in good agreement with the literature, where usually a computationally expensive full-scale beam model is used. This reduction in computational time and the enhanced detail on the microscale are a step forward to personalized care. Furthermore, the RVE is developed such that it allows for implementation in a fully coupled FE^2 model.

Detailed microstructural behaviour (the locking mechanism at high elongations and the local nitinol transformation when applying torsion) is captured with the unit cell model using solid elements. Studying this detailed information would not have been possible with a full-scale beam model, or a beam unit cell model. Regarding the macroscopic properties, the beam unit cell model has proven to yield accurate results, even when using a non-linear material model. The use of the Auricchio shape-memory material model in combination with beam elements should still be verified. Further, it has to be noted that reduced performance is observed when not enough beam elements are used, which is something to keep in mind when designing a beam model. The solid unit cell model can serve as a verification tool for the number of beam elements that should be used. Using a hinge instead of a contact description has proven to fall short in capturing the microstructural behaviour, which is consistent with the results in the literature.

In addition to the unit cell, two semi-periodic models have been developed, being periodic in either the tangential or axial direction. The tangentially periodic model has proven to be able to capture the fish mouthing effect in a computationally effective manner, requiring only five minutes to solve, compared to one hour for a full-scale beam model. The axially periodic model has shown that, in a more complex indentation load case, the different element types and tying equations show contrasting behaviour. When identical tying equations are used, the behaviour is in good agreement. Further work is needed to investigate the source of this contrasting behaviour.

Regarding the use of a fully coupled FE^2 model to capture the stent mechanics, further research is required to investigate its potential. Since using solid elements for the unit cell did not result in significantly different homogenized macroscopic properties compared to using beam elements, using the solid RVE at the microscale is not expected to provide increased accuracy compared to a full-scale beam model. However, if using shell elements at the macroscale yields promising results, there might be a computational time advantage in using an FE^2 model.

The main advantage of the developed solid unit cell model is the enhanced detail, which allowed for a thorough study of the microstructural behaviour. In future work, this enhanced detail can be used to

- calculate the required catheter size for stent delivery, using the axial elongation load case to investigate at which point the stiffness increases due to the switch in contact points.
- perform a thorough study on stent-tissue contact. The results of this study can then be used to optimize the stent's geometrical parameters to the artery size, personalizing the intervention and increasing the quality of patient care.
- judge the ability of the quasicontinuum method to capture local behaviour such as stent indentation by comparing a QC model to the developed unit cell.
- investigate the possibility of using a fully coupled FE^2 model. Especially for flow-diverting stents, which have a high number of wires, this method might have a significant improvement in computational time.

References

[1] F. Auricchio, A. Constantinescu, M. Conti, and G. Scalet. A computational approach for the lifetime prediction of cardiovascular balloon-expandable stents. *International Journal of Fatigue*, 75:69 – 79, 2015.

[2] F. Auricchio and E. Sacco. A one-dimensional model for superelastic shape-memory alloys with different elastic properties between austenite and martensite. *International Journal of Non-Linear Mechanics*, 32(6):1101 – 1114, 1997.

[3] C. Ayranci and J.P. Carey. Predicting the longitudinal elastic modulus of braided tubular composites using a curved unit-cell geometry. *Composites Part B: Engineering*, 41(3):229–235, 2010.

[4] L.A.A. Beex, R.H.J. Peerlings, and M.G.D. Geers. A multiscale quasicontinuum method for dissipative lattice models and discrete networks. *Journal of the Mechanics and Physics of Solids*, 64:154 – 169, 2014.

[5] M. De Beule. Finite element stent design. *PhD Thesis Ghent university*, 2008.

[6] M. De Beule, S. Van Cauter, P. Mortier, D. Van Loo, R. Van Impe, P. Verdonck, and B. Verhegghe. Virtual optimization of self-expandable braided wire stents. *Medical Engineering and Physics*, 31(4):448–453, 2009. Finite Element Modelling of Medical Devices.

[7] A. Bonfanti, S. Syngellakis, and A. Bhaskar. Structural analysis of cyclically periodic rings and its application to the mechanics of balloon expandable stents. *International Journal of Solids and Structures*, 185-186:46 – 56, 2020.

[8] Boston Scientific. Wallstent endoprosthesis stent, 2021. `https://www.bostonscientific.com/en-US/products/stents--vascular/wallstent-endoprosthesis.html`, last checked on 10.08.2021.

[9] M.S. Cabrera, C.W.J. Oomens, and F.P.T. Baaijens. Understanding the requirements of self-expandable stents for heart valve replacement: Radial force, hoop force and equilibrium. *Journal of the Mechanical Behavior of Biomedical Materials*, 68:252 – 264, 2017.

[10] E.W.C. Coenen, V.G. Kouznetsova, and M.G.D. Geers. Computational homogenization for heterogeneous thin sheets. *International Journal For Numerical Methods In Engineering*, 83:1180–1205, 2010.

[11] J. Daemen, R.J. van Geuns, and F. Zijlstra. Meer dan 25 jaar coronaire stents. *Nederlands Tijdschrift Geneeskunde*, 156, 09 2012.

[12] B. Drach, I. Tsukrov, and A. Trofimov. Comparison of full field and single pore approaches to homogenization of linearly elastic materials with pores of regular and irregular shapes. *International Journal of Solids and Structures*, 96:48 – 63, 2016.

[13] M. Frost, P. Sedlák, A. Kruisová, and M. Landa. Simulations of self-expanding braided stent using macroscopic model of niti shape memory alloys covering r-phase. *Journal of Materials Engineering and Performance*, 23:2584–2590, 2014.

[14] W. Fu, Q. Xia, R. Yan, and A. Qiao. Numerical investigations of the mechanical properties of braided vascular stents. *Bio-medical materials and engineering*, 29(1):81–94, 2017.

[15] M.G.D. Geers, E.W.C. Coenen, and V.G. Kouznetsova. Multi-scale computational homogenization of structured thin sheets. *Modelling and Simulation in Materials Science and Engineering*, 15(4):S393–S404, may 2007.

[16] D. Grandi and U. Stefanelli. The souza-auricchio model for shape-memory alloys. *Discrete & Continuous Dynamical Systems - S*, 8(4):723, 2015.

[17] M.R. Jedwab and C.O. Clerc. A study of the geometrical and mechanical properties of a self-expanding metallic stent–theory and experiment. *Journal of Applied Biomaterials*, 4(1):77–85, 1993.

[18] N. Kelly, D.J. McGrath, C.A. Sweeney, K. Kurtenbach, J.A. Grogan, S. Jockenhoevel, B.J. O'Brien, M. Bruzzi, and P.E. McHugh. Comparison of computational modelling techniques for braided stent analysis. *Computer Methods in Biomechanics and Biomedical Engineering*, 22(16):1334–1344, 2019. PMID: 31502888.

[19] J.H. Kim, T.J. Kang, and W.R. Yu. Mechanical modeling of self-expandable stent fabricated using braiding technology. *Journal of Biomechanics*, 41(15):3202–3212, 2008.

[20] J.H. Kim, T.J. Kang, and W.R. Yu. Simulation of mechanical behavior of temperature-responsive braided stents made of shape memory polyurethanes. *Journal of Biomechanics*, 43(4):632–643, 2010.

[21] V. Kouznetzova. Homogenization methods. *Lecture notes for the course 4MM00*, 2020.

[22] D. Lappin, A.R. Mohammadi, and K. Takahata. An experimental study of electrochemical polishing for micro-electro-discharge-machined stainless-steel stents. *Journal of Materials Science: Materials in Medicine*, 23:349–356, 2012.

[23] R. Mestriner. Material characterization of nitinol stents. *Internship report, Eindhoven University of Technology and Philips*, page 18, 2021.

[24] MSCsoftware. Msc marc 2012 user documentation. volume a: theory and user information. *Technical report, MSC Software, Santa Ana, CA, USA*, 2012.

[25] O. Rokoš, M.M. Ameen, R.H.J. Peerlings, and M.G.D. Geers. Micromorphic computational homogenization for mechanical metamaterials with patterning fluctuation fields. *Journal of the Mechanics and Physics of Solids*, 123:119–137, 2019. The N.A. Fleck 60th Anniversary Volume.

[26] O. Rokoš, M.M. Ameen, R.H.J. Peerlings, and M.G.D. Geers. Extended micromorphic computational homogenization for mechanical metamaterials exhibiting multiple geometric pattern transformations. *Extreme Mechanics Letters*, 37:100708, 2020.

[27] K. Rouf, X. Liu, and W. Yu. Multiscale structural analysis of textile composites using mechanics of structure genome. *International Journal of Solids and Structures*, 136-137:89–102, 2018.

[28] C. Shanahan, P. Tiernan, and S.A.M. Tofail. Looped ends versus open ends braided stent: A comparison of the mechanical behaviour using analytical and numerical methods. *Journal of the Mechanical Behavior of Biomedical Materials*, 75:581–591, 2017.

[29] C. Shanahan, S.A.M. Tofail, and P. Tiernan. Viscoelastic braided stent: Finite element modelling and validation of crimping behaviour. *Materials & Design*, 121:143–153, 2017.

[30] S. Shiozaki, T. Otani, S. Fujimura, H. Takao, and S. Wada. Computational modeling of braided-stent deployment for interpreting the mechanism of stent flattening. *International Journal for Numerical Methods in Biomedical Engineering*, 1:14, 2020.

[31] J.R. Stevens, A. Zamani, J.I.A. Osborne, R. Zamani, and M Akrami. Critical evaluation of stents in coronary angioplasty: a systematic review. *BioMedical Engineering OnLine*, 20:46, 2021.

[32] T. Suzuki, H. Takao, S. Fujimura, C. Dahmani, T. Ishibashi, H. Mamori, N. Fukushima, Y. Murayama, and M. Yamamoto. Relationships between geometrical parameters and mechanical properties for a helical braided flow diverter stent. *Technology and Health Care*, 25(4):611–623, 2017.

[33] E.B. Tadmor, M. Ortiz, and R. Phillips. Quasicontinuum analysis of defects in solids. *Philosophical Magazine A*, 73(6):1529–1563, 1996.

[34] P. Velvaluri, J. Hensler, F. Wodarg, O. Jansen, and E. Quandt. Torsional characterization of braided flow diverter stents. *Clinical Neuroradiology*, 2021.

[35] J. Youn Park, C. Park, J. Shin Park, K. Kong, H. Chang, and S. Im. Multiscale computations for carbon nanotubes based on a hybrid qm/qc (quantum mechanical and quasicontinuum) approach. *Journal of the Mechanics and Physics of Solids*, 58(2):86 – 102, 2010.

[36] A. Zaccaria, G. Pennati, and L. Petrini. Analytical methods for braided stents design and comparison with fea. *Journal of the Mechanical Behavior of Biomedical Materials*, 119:104560, 2021.

[37] J. Zhai, T. Zeng, G. Xu, Z. Wang, S. Cheng, and D. Fang. A multi-scale finite element method for failure analysis of three-dimensional braided composite structures. *Composites Part B: Engineering*, 110:476–486, 2017.

A Mathematical model of a braided stent

As explained in section 2.1, the geometry of the braided stent can be described using only five parameters: length L, braiding angle α, average diameter D, wire thickness t and number of clockwise wires n. The mathematical model developed by Jedwab et al. uses these five parameters to calculate the stent's mechanical properties [17]. Important to note is that the length, diameter, and braiding angle change when the stent is compressed. The starting values of these parameters, so for an undeformed stent, are denoted as L_0, D_0 and α_0. The number of revolutions that an individual wire makes around the central axis is calculated as

$$n_{\text{rev}} = \frac{L_0 \tan(\alpha_0)}{\pi D_0}. \tag{A.1}$$

In the work of Jedwab et al., a change in braiding angle is prescribed, which results in a change in diameter and length. For implementation purposes, it is more convenient to prescribe a change in length, since deformations of the stent RVE are prescribed as in-plane displacements. The equations are rewritten to allow for prescribing a length change as

$$L = (1 + \varepsilon_{22})L_0. \tag{A.2}$$

In this equation, the length change is prescribed by $\varepsilon_{22}L_0$, with ε_{22} the strain in the axial direction. The diameter and braiding angle at the new length L are calculated as

$$\alpha = \cos^{-1}\left(\frac{L\cos(\alpha_0)}{L_0}\right), \tag{A.3}$$

$$D = D_0 \frac{\sin(\alpha)}{\sin(\alpha_0)}. \tag{A.4}$$

Using the values of L, α, and D after deformation, the axial load on the stent can be calculated as

$$F = 4n\left[\frac{GI_P}{C_3}\left(\frac{2\cos(\alpha)}{C_3} - C_1\right) - \frac{EI}{C_3\tan(\alpha)}\left(\frac{2\sin(\alpha)}{C_3} - C_2\right)\right]. \tag{A.5}$$

This equation includes the erratum made by de Beule et al., leaving out a $\sin(\alpha)$ term [5]. I and I_P are the moment of inertia and polar moment of inertia of the wire respectively, given by $I = \pi t^4/64$ and $I_P = \pi t^4/32$. Constants C_1, C_2 and C_3 are given by

$$C_1 = \frac{\sin(2\alpha_0)}{D_0}, \tag{A.6}$$

$$C_2 = \frac{2\sin^2(\alpha_0)}{D_0}, \tag{A.7}$$

$$C_3 = \frac{D_0}{\sin(\alpha_0)}. \tag{A.8}$$

Using the same constants, radial force R_F, radial pressure P, axial stiffness K_L and radial stiffness K_P can be calculated as follows

$$R_F = 2\pi F n_{\text{rev}} \tan(\alpha), \tag{A.9}$$

$$P = \frac{R_F}{\pi DL} = \frac{2F n_{\text{rev}} \tan(\alpha)}{DL}, \tag{A.10}$$

$$K_L = \frac{4n}{\pi C_3 n_{\text{rev}} \sin(\alpha)} \left[\frac{GI_P}{C_3} \left(\frac{2\sin(\alpha)}{C_3} \right) - \frac{EI}{C_3} \left(\frac{2\sin(\alpha)}{C_3} - C_2 \csc^2(\alpha) \right) \right], \tag{A.11}$$

$$\begin{aligned} K_P = & \frac{2n_{rev}}{C_3 \cos(\alpha)(DL\cot(\alpha))^2} \left\{ 2nDL\cot(\alpha) \left[\frac{GI_P}{C_3} \left(\frac{2\sin(\alpha)}{C_3} \right) - \frac{EI}{C_3} \left(\frac{2\sin(\alpha)}{C_3} - C_2 \csc^2(\alpha) \right) \right] \right. \\ & \left. -F \left[C_3 \cos(\alpha)(\pi t D - L\cot(\alpha)) + \frac{DL}{\sin^2(\alpha)} \right] \right\}. \end{aligned} \tag{A.12}$$

Another feature of the mathematical model is that the minimum possible diameter, $D_{\min}$, and the maximum elongation, $\varepsilon_{\max}$ can be calculated as

$$\alpha_{\min} = \frac{1}{2} \sin^{-1} \left(\frac{nt \sin(\alpha_0)}{\pi D_0} \right), \tag{A.13}$$

$$D_{\min} = \frac{nt}{\pi \cos(\alpha_{\min})}, \tag{A.14}$$

$$\varepsilon_{\max} = \frac{\cos(\alpha_{\min})}{\cos(\alpha_0)} - 1 \tag{A.15}$$

B Auricchio material model

The implementation described in this appendix is based on the work of Auricchio et al. [2]. It is checked carefully that the implementation in the selected software environment, Marc Mentat, is the same [24].

The model makes a distinction between elastic strain ε^{el}, and strain related to the phase transformation ξ:

$$\varepsilon = \varepsilon^{el} + \xi. \tag{B.1}$$

The transformation strain ξ depends on the fraction of martensite present in the sample, denoted by ζ as

$$\xi = \zeta \varepsilon_{\mathrm{L}} \mathrm{sgn}(\varepsilon). \tag{B.2}$$

The material parameter ε_L is the maximum transformation strain, and sgn() is the sign function. The stress σ is related to the elastic strain by elastic modulus E as

$$\sigma = E\varepsilon^{el}. \tag{B.3}$$

The effective elastic modulus E also depends on ζ, which can be obtained by using the Voigt averaging method. This method uses the moduli of austenite E_{A}, martensite E_{S}, and the martensite fraction ζ as in equation B.4. The effective Poisson's ratio can be calculated the same way.

$$E = E_{\mathrm{A}}(1-\zeta) + E_{\mathrm{S}}\zeta \tag{B.4}$$

$$\nu = \nu_{\mathrm{A}}(1-\zeta) + \nu_{\mathrm{S}}\zeta \tag{B.5}$$

The transformation stresses are required to obtain the martensite volume fraction ζ. While transforming from austenite to martensite, ζ can be obtained by solving

$$\dot{\zeta} = -(1-\zeta)\frac{|\dot{\sigma}|}{|\sigma| - \sigma_{\mathrm{f}}^{AS}}. \tag{B.6}$$

To calculate the volume fraction while transforming from martensite to austenite, the equation that should be solved is

$$\dot{\zeta} = \zeta\frac{|\dot{\sigma}|}{|\sigma| - \sigma_{\mathrm{f}}^{SA}}. \tag{B.7}$$

C Python script stent unit cell

In this appendix, the script to generate the stent RVE is explained. At first, the main file, 'createUC2.py' is presented and explained. Next, the files in the background are explained briefly, including an explanation of the functions in each file.

Main file

The code of the main file, called 'createUC2.py' is as follows:

```
from iolib import ( inputCheck, writeInputUC2,
                    writeReadfiles )
from modelslib import ( createMesh_UC2, createSineNodes_UC2,
                        calcU, createMesh_Beam )
from analytical import deBeule
from classes import JobParams, Basemesh, Stent

# Stent initialization
s = Stent(
    "C",            # Stent geometry, C for curved, P for planar
    60,             # Stent target length L [mm]
    16,             # Stent external diameter De [mm]
    45,             # Stent braiding angle alpha [deg]
    0.25,           # Stent wire diameter t [mm]
    12              # Stent number of CW wire n [-]
    )
s.calcUCsize()

# Job parameter initialization
p = JobParams(
    [[ 1 , 0] ,
     [ 0 , 1.1]],   # Deformation tensor F
    0,              # Curvature k22
    0.2,            # Friction coefficient fc
    42,             # Youngs modulus E [GPa]
    0.33,           # Poissons ratio v
    6.450,          # Material density [g/cm^3]
    "Lin",          # "Ni" for Nitinol. "Lin" for linear elastic
    s.zUC
    )

# Mesh initialization
m = Basemesh( "M" ) # Mesh refinement, M for medium, F for fine
nref    = 36        # Refinement factor UC solid model
nref_b  = 6         # Refinement factor UC beam model

# Checking input parameters
inputCheck( s, nref, nref_b )

# Creating unit cell mesh
sinecoords = createSineNodes_UC2( s, nref )
coords, connect = createMesh_UC2( s, m, sinecoords, nref )
beamcoords, connectbeam = createMesh_Beam( m, nref, nref_b, coords )

# Calculating boundary conditions
u, Xp, cnodes = calcU( s, p )

# Creating MM input and read files
writeInputUC2( s, m, p, u, nref, nref_b, coords, connect, beamcoords, connectbeam, cnodes )
writeReadfiles( s, p )

# Calculating analytical values
Rf, F, P, Kl, Kp = deBeule( s, p )
print('long. load F      : {0:8.3f}    N'      .format(F))
print('Radial force      : {0:8.3f}    N'      .format(Rf))
print('rad. pressure P:  : {0:8.3f}    N/mm^2'.format(P))
print('longit. stiffness : {0:10.5f}  N/mm'    .format(Kl))
print('radial  stiffness : {0:10.5f}  N/mm^3' .format(Kp))
```

Explanation main file

In lines 1 till 6, functions from other files are imported. In lines 8 till 17, the stent geometry is defined, using the geometrical parameters as provided in Section 2.1. In addition to the geometry, a planar or curved geometry can be chosen in line 10. In lines 19 till 30, the job parameters can be set. These parameters include the matrix representation of deformation tensor $\mathbf{F}_{\mathrm{M}}$, component κ_{22} of curvature tensor $\mathbf{K}_{\mathrm{M}}$, the friction coefficient, and material parameters E, ν and ρ. In line 28, using the nitinol or linear material model can be specified. Additional job parameters can be specified in the JobParams class in classes.py or in the Marc Mentat model itself. The mesh refinement can be specified in lines 32-35.

After defining the stent's geometry, job parameters, and mesh refinement, and after checking the input parameters in line 38, the mesh for both the solid model and beam model is calculated in lines 40-43. After calculating the boundary conditions in lines 45-56, the input files are written in line 49. Files to read the reaction forces are written in line 50. Lines 52-58 provide insight on the values for axial load F, radial load F_{R}, radial pressure P, axial stiffness K_{l}, and radial stiffness K_{p}, which are calculated using the analytical model of appendix A.

File structure

For this overview, the Python files are separated into two file types, front-end files and back-end files, listed in Table 8 and 9, respectively. The front-end files are the files where the user's input is required, e.g. to specify the stent's geometrical parameters. The back-end files do not require input from the user and should only be opened when changes have to be made to the background functions.

Table 8: Overview of front-end files. In these files, input is required from the user.

Front-end	Coupled to	Description
createUC1.py*	modelslib.py, analytical.py, classes.py, iolib.py	File used to generate the unit cell geometry as depicted in the left of Figure 2.9, denoted by UC1. The unit cell geometry is based on the work of Ayrenci et al. [3]. It turned out that this geometry was not practical to use. Works only for the planar unit cell.
createUC2.py	modelslib.py, analytical.py, classes.py, iolib.py	File used to generate the unit cell geometry as depicted in the right of Figure 2.9, denoted by UC2. A more elaborate description is provided in the section above.
calcResults.py	createUC2.py, proceslib.py, modelslib.py, analytical.py, iolib.py	File used to read the reaction forces of the MM output files. After the reaction forces are read, macroscopic homogenized properties are calculated. The results can be visualized using the matplotlib library.

* This file has become obsolete and hasn't been used since halfway the project. An update is needed to run this file again.

Table 9: Overview of back-end files. In these files, no input is required from the user.

Back-end	Functions	Description
modelslib.py		File containing all functions needed to generate the unit cell mesh.
	createMesh_UC1()	(obsolete) Creating and positioning the 2D mesh of the wire cross-section for the UC1 geometry. The mesh is completed by using the UC1 proc file, extruding the 2d mesh along a sinusoidal curve.
	createMesh_UC2_P()	Creating the mesh of the UC2 geometry using solid elements for the planar unit cell.

	createMesh_UC2_C()	Creating the mesh of the UC2 geometry using solid elements for the curved unit cell.
	createMesh_Beam	Creating the mesh of the UC2 geometry using beam elements, planar or curved, depending on input parameter.
	createSineNodes_UC1()	(obsolete) Creating the sine curve for the 'extrude along curve' function in MM to create the UC1 mesh.
	createSineNodes_UC2_P()	Creating the sine curve of the UC2 wires in the planar geometry, used for positioning of the nodes and elements in the createMesh() function.
	createSineNodes_UC2_C()	Creating the sine curve of the UC2 wires in the curved geometry, used for positioning of the nodes and elements in the createMesh() function.
	meshCircle()	Function to create and position the 2D wire cross-section mesh.
	meshSemiCircle()	(obsolete) Function to create and position half of the 2D wire cross-section mesh, used only for the UC1 geometry.
	basicCosine()	(obsolete) Function to discretize a cosine wave into n points, used for UC1 only.
	basicSine()	Function to discretize a sine wave into n points.
	basichalfSine()	Function to discretize half of a sine wave into n points.
	calcU()	Calculating boundary conditions, based on the deformation and curvature tensor.
	rotX()	Function to apply a rotation around the x-axis to a mesh.
	rotY()	Function to apply a rotation around the y-axis to a mesh.
	rotZ()	Function to apply a rotation around the z-axis to a mesh.
iolib.py		File containing all relevant functions to write the input and output files for MSC Marc/Mentat.
	inputCheck()	Checking the validity of the input parameters on stent geometry.
	writeInputUC1()	Write all MM input files for UC1 geometry.
	writeInputUC2()	Write all MM input files for UC2 geometry.
	writeReadfiles()	Write all files to read MM output.
	addTable()	Add a table with 1 time variable.
	addMaterial()	Add linear material for all elements.
	addNitinol()	Add Nitinol material model for all elements.
	addTransform()	Add cylindrical coordinate system by transforming each node to a local Cartesian coordinate system.
	addContact()	Add default touch contact with the specified friction coefficient.
	addLoadcase()	Add load case with fixed time interval, as specified in the JobParams class.
	addJob()	Add job, using the updated Lagrangian solver for large strain and segment to segment contact.
	addNodes()	Add all nodes and elements of the generated mesh.
	moveStent()	Move stent to the position where the node in the center of the RVE is located at $[r, 0, 0]$.
	writeDAT_UC2()	Writing the .DAT file for the UC2 geometry to import the nodes and elements. Use the .DAT file for increased speed for MM2020 and below. for MM2021, only the .PROC file should be used.

	writePROC_UC2()	Writing the .PROC file to input the UC2 unit cell using solid elements, including tying equations, boundary conditions, and job parameters, in MM.
	editBC()	Write a file to quickly edit the boundary conditions of a MM model in case a new load case should be prescribed.
	editLinks_k22()	Writing a file to edit the servo links to allow for applying curvature, by default, the first order tying equations are applied.
	writePROC_Beam()	Writing the .PROC file to input the UC2 unit cell using beam elements, including tying equations, boundary conditions, and job parameters, in MM.
	writePROC_macro()	Writing the .PROC file for the macroscopic model, as depicted in Figure 2.6 in section 2.2.1.
	writePROC_sptan_beam()	Writing the .PROC file to generate the semi-periodic model, periodic in tangential direction, using beam elements.
	writePROC_sptan()	Writing the .PROC file to generate the semi-periodic model, periodic in tangential direction, using solid elements.
	writePROC_spaxial_beam()	Writing the .PROC file to generate the semi-periodic model, periodic in axial direction, using beam elements.
	writePROC_spaxial()	Writing the .PROC file to generate the semi-periodic model, periodic in axial direction, using solid elements.
	readForces()	Writing the .PROC file to read the reaction forces for the unit cell with solid elements.
	readRadforces()	Writing the .PROC file to read the reaction forces in radial direction, for the radial force load case.
	readForces_step()	Writing the .PROC file to read the reaction forces for the unit cell with solid elements for a number of steps in the simulation.
	readForces_step_beam()	Writing the .PROC file to read the reaction forces for the unit cell with beam elements for a number of steps in the simulation.
	readMoments_step()	Writing the .PROC file to read the reaction moments in the case curvature is applied to the beam model.
	writeDAT_UC1()	(obsolete) Writing the .DAT file for the UC1 geometry to import the nodes and elements. Use the .DAT file for increased speed for MM2020 and below. for MM2021, only the .PROC file should be used.
	writePROC_UC1()	(obsolete) Writing the .PROC file to import the UC1 unit cell geometry in MM.
proceslib.py		File containing all relevant functions to process results and calculate macroscopic properties.
	storeForces()	Store reaction forces from the MM output file.
	storeMoments()	Store reaction moments from the MM output file. Only in the case when bending is applied to the beam model.
	calcStress()	Calculate homogenized engineering stress and couple-stress tensors $\mathbf{N}_{\mathrm{M}}$ and $\mathbf{N}_{\mathrm{M}}$.
	calcMoment()	Calculate the $\mathbf{M}_{\mathrm{M}(22)}$ component when bending is applied to the beam model, using the reaction moments of the simulation.

	calcRadforce()	Calculate the total radial force when the radial force load case is applied.
analytical.py		File containing the mathematical model to calculate stent properties.
	jedwab()	Mathematical model to calculate F, F_{R}, P, K_{l}, and K_{p} [17].
	deBeule()	Mathematical model to calculate F, F_{R}, P, K_{l} ,and K_{p}, including erratum made by deBeule et al. [5].
baseMesh.py		File containing coordinate and connectivity data of a basic 2D circular mesh. A medium and a fine mesh is included.
classes.py		File containing all classes of the script.
	class Stent	This class contains the geometrical parameters of the stent.
	class JobParams	This class contains the job parameters.
	class Basemesh	This class contains the 2D circular mesh of the wire's cross-section.

D Homogenization

D.1 First-order homogenization

As mentioned in section 2.2, the general idea of computational homogenization methods is to replace the heterogeneous material at the macroscale with a homogeneous problem, with the effective material properties obtained from the heterogeneous microstructure [21]. For convenience, Figure 2.5 of section 2.2.1 is depicted in this appendix as well.

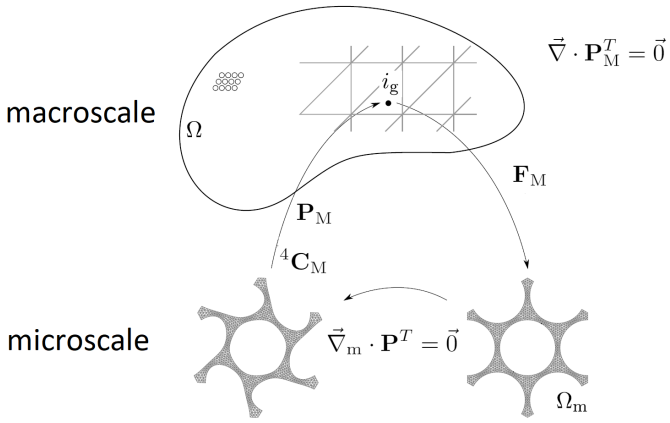

Figure D.1: Sketch of a computational homogenization framework. At each integration point i_g of the macroscopic domain Ω, a representative volume element (RVE) with domain Ω_{m} is considered, inside which the microfluctuation field is computed. Homogenized properties are transferred back to the macroscale [26].

The applied deformation gradient tensor $\mathbf{F}_{\mathrm{M}}$ can be represented by a matrix as

$$\underline{\mathbf{F}}_{\mathrm{M}} = \begin{bmatrix} 1+\varepsilon_{11} & \varepsilon_{12} \\ \varepsilon_{21} & 1+\varepsilon_{22} \end{bmatrix}, \tag{D.1}$$

where ε_{11}, ε_{12}, ε_{21}, and ε_{22} are the generalized macroscopic strains. The boundary conditions are of great importance to capture the mechanics of the underlying microstructure. In this study, periodic boundary conditions are used. For simplicity, a 2D RVE is used to explain the principles and relevant equations. A typical example of a two-dimensional RVE, with boundary Γ, is depicted in Figure D.2.

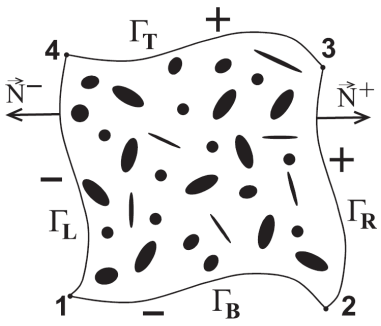

Figure D.2: Schematic representation of a two-dimensional RVE [21].

The deformation of the RVE is described by the macroscopic deformation gradient tensor $\mathbf{F}_{\mathrm{M}}$, and a microfluctuation field, denoted by $\vec{w}_{\mathrm{m}}$. A material vector $\vec{x}_{\mathrm{m}}$ in the deformed configuration can be related to the same material vector $\vec{X}_{\mathrm{m}}$ in the undeformed state as

$$\vec{x}_{\mathrm{m}} = \mathbf{F}_{\mathrm{M}} \cdot \vec{X}_{\mathrm{m}} + \vec{w}_{\mathrm{m}}. \tag{D.2}$$

The RVE boundaries are split in '+' and '-' parts, defined by outward unit normal vectors $\vec{\mathrm{N}}^{+}$ and $\vec{\mathrm{N}}^{-}$ in Figure D.2. Periodic boundary conditions are imposed by requiring periodicity of the microfluctuation field,

$$\vec{w}_{\mathrm{m}}^{+} = \vec{w}_{\mathrm{m}}^{-}. \tag{D.3}$$

The position vectors of the '+' and '-' sides of the RVE are defined by $\vec{x}_{\mathrm{m}}^{+}$ and $\vec{x}_{\mathrm{m}}^{-}$. The difference between these vectors is explained by applying the macroscopic deformation gradient tensor to the undeformed position vectors as follows

$$\vec{x}_{\mathrm{m}}^{+} - \vec{x}_{\mathrm{m}}^{-} = \mathbf{F}_{\mathrm{M}} \cdot (\vec{X}_{\mathrm{m}}^{+} - \vec{X}_{\mathrm{m}}^{-}). \tag{D.4}$$

The macroscopic first Piola–Kirchhoff stress tensor $\mathbf{P}_{\mathrm{M}}$ can be related to the volume average of the microscopic first Piola–Kirchhoff stress tensor $\mathbf{P}_{\mathrm{m}}$ as

$$\mathbf{P}_{\mathrm{M}} = \frac{1}{V_{0\mathrm{m}}} \int_{V_{0\mathrm{m}}} \mathbf{P}_{\mathrm{m}} dV_{0\mathrm{m}}. \tag{D.5}$$

Numerical implementation

Prescribing deformations to the RVE is done by prescribing displacements $\vec{u}$ for the corner nodes 1, 2, and 4 of the 2D sample as

$$\vec{u}_p = (\mathbf{F}_{\mathrm{M}} - I) \cdot \vec{X}_p, \qquad p = 1, 2, 4. \tag{D.6}$$

When using the expression above to prescribe the corner nodes, equation (D.4) can be rewritten in terms of displacement vectors. The boundary of the 2D RVE is fully prescribed by tying the displacement vectors of the top/bottom and left/right boundaries as

$$\begin{aligned} \vec{u}_{\mathrm{T}} &= \vec{u}_{\mathrm{B}} + \vec{u}_4 - \vec{u}_1, \\ \vec{u}_{\mathrm{R}} &= \vec{u}_{\mathrm{L}} + \vec{u}_2 - \vec{u}_1. \end{aligned} \tag{D.7}$$

In MSC Marc/Mentat, these constraints are implemented with servo links. Servo links allow prescription of nodal displacements in the form of linear functions with constant coefficients [12]. A one-dimensional servo link is defined as

$$u_{\mathrm{t}} = a_1 u_I + a_2 u_{II} + a_3 u_{III}, \tag{D.8}$$

tying node u_{t} to 3 other nodes. To implement the periodic boundary conditions according to equation D.7, three nodes are should be tied. Two nodes have coefficients of 1 ($a_1 = a_2 = 1$), the $\vec{u}_1$ node has a coefficient of -1 ($a_3 = -1$). Displacement u_{I} is the congruent node of u_{t}, on the opposite side of the RVE. u_{II} is either $\vec{u}_2$ or $\vec{u}_4$. Macroscopic deformation according to $\mathbf{F}_{\mathrm{M}}$ is prescribed on $\vec{u}_1$, $\vec{u}_2$ and $\vec{u}_4$ according to equation D.6. In case there is no material at the corners of the RVE, separate control nodes can be used to prescribe $\mathbf{F}_{\mathrm{M}}$ as in Figure D.3.

In 2D, each congruent node pair requires two servo links since the servo links are one-dimensional constraints. One link will prescribe the deformation in x, the other one the deformation in y. A 2D example of tying the top and right side nodes to the bottom and left side nodes is depicted in Figure D.3. The results of applying various deformation gradient tensors are shown in Figure D.4.

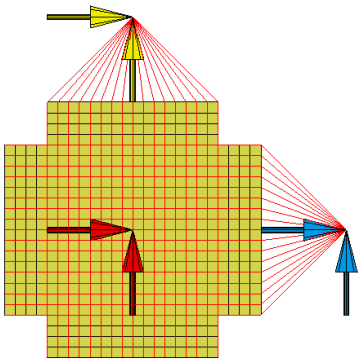

Figure D.3: 2D example of the application of periodic boundary conditions in MSC Marc/Mentat using servo links. Control nodes are used to prescribe $\mathbf{F}_{\mathrm{M}}$. Note that there are no nodes in the corners of the RVE because there is no material. Rigid body motion of the RVE is prevented by constraining all DOFs at the centre node.

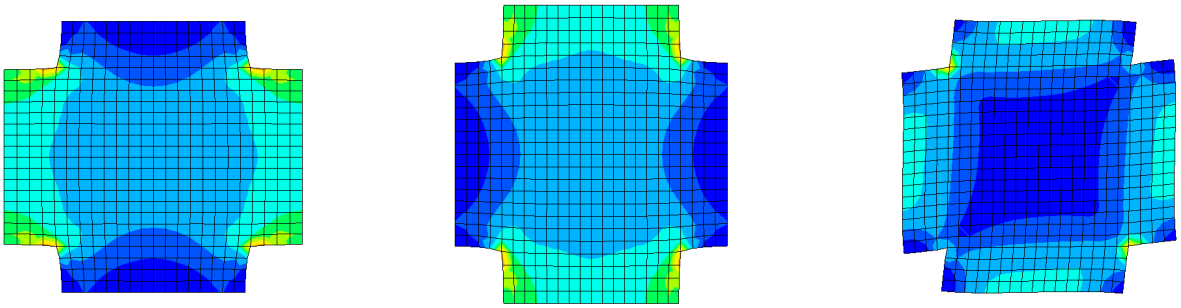

(a) $\underline{\mathbf{F}}_{\mathrm{M}} = \begin{bmatrix} 1.1 & 0 \\ 0 & 1 \end{bmatrix}$ (b) $\underline{\mathbf{F}}_{\mathrm{M}} = \begin{bmatrix} 1 & 0 \\ 0 & 1.1 \end{bmatrix}$ (c) $\underline{\mathbf{F}}_{\mathrm{M}} = \begin{bmatrix} 1 & 0.05 \\ 0.05 & 1 \end{bmatrix}$

Figure D.4: Resulting Von Mises stress fields corresponding to applied macroscopic deformation $\mathbf{F}_{\mathrm{M}}$.

After the simulations, the macroscopic stress can be calculated by numerically implementing equation (D.5) as

$$\underline{\mathbf{P}}_{\mathrm{M}} = \frac{1}{V_{0\mathrm{m}}} \sum_{p=1,2,4} \vec{f}_p \otimes \vec{X}_P. \tag{D.9}$$

Note that the stress tensor is represented by a matrix here, denoted by $\underline{\mathbf{P}}_{\mathrm{M}}$. $\vec{f}_p$ are the reaction forces at the prescribed nodes, and $\vec{X}_{\mathrm{P}}$ are the position vector of point p in the undeformed configuration. The resulting macroscale first Piola-Kirchhoff stress tensors calculated by using equation D.9 are provided below. For this example, the Young's modulus and Poisson's ratio are set to 70 Gpa and 0.3, respectively.

$$(a)\ \underline{\mathbf{P}}_{\mathrm{M}} = \begin{bmatrix} 7700 & 0 \\ 0 & 2600 \end{bmatrix} \qquad (b)\ \underline{\mathbf{P}}_{\mathrm{M}} = \begin{bmatrix} 2600 & 0 \\ 0 & 7700 \end{bmatrix} \qquad (c)\ \underline{\mathbf{P}}_{\mathrm{M}} = \begin{bmatrix} 275 & 1700 \\ 1700 & 275 \end{bmatrix} \tag{D.10}$$

D.2 Second-order homogenization

As described in section 2.3, classical first-order homogenization is not able to prescribe bending at the RVE level, and thus a higher-order implementation is desired. Previous work on the homogenization of structured, thin sheets uses a second-order RVE to prescribe bending at the microscale [15]. For convenience, Figure 2.7 of section 2.2.1 is depicted in this appendix as well. This appendix provides a more detailed but still brief description of the framework. A complete derivation of all provided equations can be found in the work of Coenen, Kouznetsova and Geers [10].

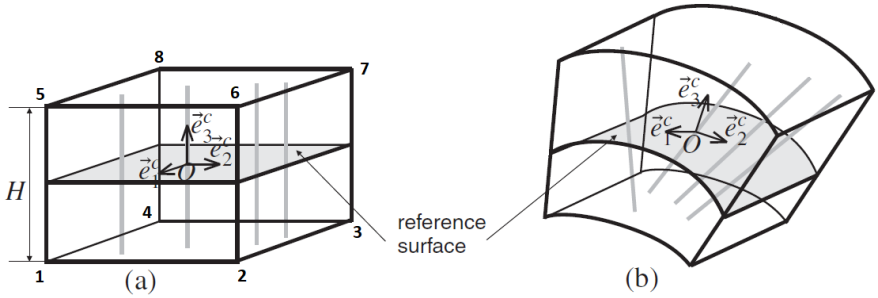

Figure D.5: RVE in the reference (a) and deformed configuration (b) [10].

The RVE is defined with a corotational basis at the center $\{\vec{e}_1^c, \vec{e}_2^c, \vec{e}_3^c\}$, such that the plane $(\vec{e}_1^c,\vec{e}_2^c)$ is tangent to the reference surface. The reference surface is located at half the RVE height for convenience, but can be located arbitrary between top and bottom surface. The third basis vector $\vec{e}_3^c$ is defined normal to this tangent plane. The deformation is described by the deformation gradient tensor $\mathbf{F}_\mathrm{M}$ and it's gradient ${}^3\mathbf{G}_\mathrm{M}$ $(\vec{\nabla}_{0\mathrm{M}}\mathbf{F}_\mathrm{M})$ as

$$\Delta\vec{x}_\mathrm{m} = \mathbf{F}_\mathrm{M}\cdot\Delta\vec{X}_\mathrm{m} + \frac{1}{2}\Delta\vec{X}_\mathrm{m}\cdot{}^3\mathbf{G}_\mathrm{M}\cdot\Delta\vec{X} + \vec{w}_\mathrm{m}. \tag{D.11}$$

At the macroscale, Kirchhoff-Love thin shell elements are used to describe the homogenized continuum, neglecting transverse shear and assuming plane stress. For further implementation at the RVE level, the deformations are split into an in-plane and an out-of-plane component. By only prescribing in-plane components, it is ensured that the plane stress condition holds. The in-plane component is defined as the projection on the $(\vec{e}_1^c,\vec{e}_2^c)$-plane and denoted by a superimposed symbol $\hat{}$. The out-of-plane component is the projection on the $\vec{e}_3^c$-direction and is denoted by a superimposed $\tilde{}$ symbol. The in-plane and out-of-plane deformations at the RVE can now be described as

$$\Delta\hat{\vec{x}}_\mathrm{m} = (\hat{\mathbf{F}}_\mathrm{M} + \zeta\hat{\mathbf{K}}_\mathrm{M})\cdot\Delta\hat{\vec{X}}_\mathrm{m} + \Delta\hat{\vec{w}}_\mathrm{m}, \tag{D.12}$$

$$\Delta\tilde{\vec{x}}_\mathrm{m} = \tilde{\mathbf{F}}_\mathrm{M}\cdot\Delta\hat{\vec{X}}_\mathrm{m} - \frac{1}{2}\vec{e}_3^c\hat{\mathbf{K}}_\mathrm{M} : \Delta\hat{\vec{X}}_\mathrm{m}\Delta\hat{\vec{X}}_\mathrm{m} + \Delta\tilde{\vec{w}}_\mathrm{m}. \tag{D.13}$$

In this equation, the out-of-plane component is denoted by ζ, with $\zeta\in[-H/2, H/2]$. Curvature tensor $\mathbf{K}_\mathrm{M}$ is related to components of ${}^3\mathbf{G}_\mathrm{M}$ as

$$\underline{\hat{\mathbf{K}}}_\mathrm{M} = \begin{bmatrix}\kappa_{11} & \kappa_{12}\\ \kappa_{21} & \kappa_{22}\end{bmatrix} = \begin{bmatrix}G_{311} & G_{312}\\ G_{321} & G_{322}\end{bmatrix}. \tag{D.14}$$

To prescribe the periodicity of the unit cell, the microfluctuations of the right and left nodes have to be equal, $\Delta\vec{w}_\mathrm{m}^L(\zeta) = \Delta\vec{w}_\mathrm{m}^R(\zeta)$. The same holds for the nodes at the bottom and top surface. Using this, and

using the in-plane deformations as described in equation (D.12) and (D.13), tying relations are prescribed to congruent node pairs as

$$\begin{aligned}\hat{\vec{u}}_{\mathrm{m}}^{R} &= \hat{\vec{u}}_{\mathrm{m}}^{L} + (\hat{\hat{\mathbf{F}}}_{\mathrm{M}} - \hat{\hat{\mathbf{I}}} + \zeta\hat{\hat{\mathbf{K}}}_{\mathrm{M}}) \cdot (\hat{\vec{X}}_{\mathrm{m}}^{R} - \hat{\vec{X}}_{\mathrm{m}}^{L}),\\ \hat{\vec{u}}_{\mathrm{m}}^{T} &= \hat{\vec{u}}_{\mathrm{m}}^{B} + (\hat{\hat{\mathbf{F}}}_{\mathrm{M}} - \hat{\hat{\mathbf{I}}} + \zeta\hat{\hat{\mathbf{K}}}_{\mathrm{M}}) \cdot (\hat{\vec{X}}_{\mathrm{m}}^{F} - \hat{\vec{X}}_{\mathrm{m}}^{B}),\end{aligned} \tag{D.15}$$

$$\begin{aligned}\tilde{\vec{u}}_{\mathrm{m}}^{R} &= \tilde{\vec{u}}_{\mathrm{m}}^{L} - \frac{1}{2}\vec{e}_3^{c}\hat{\hat{\mathbf{K}}}_{\mathrm{M}} : (\hat{\vec{X}}_{\mathrm{m}}^{R}\hat{\vec{X}}_{\mathrm{m}}^{R} - \hat{\vec{X}}_{\mathrm{m}}^{L}\hat{\vec{X}}_{\mathrm{m}}^{L}),\\ \tilde{\vec{u}}_{\mathrm{m}}^{T} &= \tilde{\vec{u}}_{\mathrm{m}}^{B} - \frac{1}{2}\vec{e}_3^{c}\hat{\hat{\mathbf{K}}}_{\mathrm{M}} : (\hat{\vec{X}}_{\mathrm{m}}^{F}\hat{\vec{X}}_{\mathrm{m}}^{F} - \hat{\vec{X}}_{\mathrm{m}}^{B}\hat{\vec{X}}_{\mathrm{m}}^{B}).\end{aligned} \tag{D.16}$$

The macroscopic engineering stress resultant $\hat{\hat{\mathbf{N}}}_{\mathrm{M}}$ and couple-stress resultant $\hat{\hat{\mathbf{M}}}_{\mathrm{M}}$ can be calculated by integrating Piola-Kirchhoff stress vector $\hat{\vec{p}}_{\mathrm{m}}$ over the undeformed surface $\tilde{\Gamma}_{\mathrm{m}}$ as

$$\hat{\hat{\mathbf{N}}}_{\mathrm{M}} = \frac{1}{A_{\mathrm{m}}}\int_{\tilde{\Gamma}_{\mathrm{m}}} \hat{\vec{p}}_{\mathrm{m}}\hat{\vec{X}}_{\mathrm{m}}\mathrm{d}\tilde{\Gamma}_{\mathrm{m}}, \tag{D.17}$$

$$\hat{\hat{\mathbf{M}}}_{\mathrm{M}} = \frac{1}{A_{\mathrm{m}}}\int_{\tilde{\Gamma}_{\mathrm{m}}} (\zeta\hat{\vec{p}}_{\mathrm{m}}\hat{\vec{X}}_{\mathrm{m}} - \frac{1}{2}\tilde{\vec{p}}_{\mathrm{m}} \cdot \vec{e}_3^{c}\hat{\vec{X}}_{\mathrm{m}}\hat{\vec{X}}_{\mathrm{m}})\mathrm{d}\tilde{\Gamma}_{\mathrm{m}}. \tag{D.18}$$

Numerical Implementation

For the numerical implementation, the top, bottom, right and left surface are defined as

$$\begin{aligned}\Gamma_T &= \{4,3,7,8\},\\ \Gamma_B &= \{1,2,6,5\},\\ \Gamma_R &= \{2,3,7,6\},\\ \Gamma_L &= \{1,4,8,5\},\end{aligned} \tag{D.19}$$

using the numbers as depicted in Figure D.5. The RVE is fixed at one point to prevent rigid body motion, both in the in-plane direction as in the out-of-plane direction. This can be done at an arbitrary point. Since the stent unit cell has material at the centre by definition, it is chosen to fix the RVE in the centre, $\vec{x}_{\mathrm{m}}^{O} = \vec{X}_{\mathrm{m}}^{O}$. The five in-plane deformations are prescribed as

$$\begin{aligned}\hat{\vec{u}}_{\mathrm{m}}^{i} &= (\hat{\hat{\mathbf{F}}}_{\mathrm{M}} - \hat{\hat{\mathbf{I}}} + \zeta^{1}\hat{\hat{\mathbf{K}}}_{\mathrm{M}}) \cdot \hat{\vec{X}}_{\mathrm{m}}^{i}, \qquad i = 1,2,4,\\ \hat{\vec{u}}_{\mathrm{m}}^{56} &= \hat{\vec{u}}_{\mathrm{m}}^{6} - \hat{\vec{u}}_{\mathrm{m}}^{5} = (\hat{\hat{\mathbf{F}}}_{\mathrm{M}} - \hat{\hat{\mathbf{I}}} + \zeta^{5}\hat{\hat{\mathbf{K}}}_{\mathrm{M}}) \cdot (\hat{\vec{X}}_{\mathrm{m}}^{6} - \hat{\vec{X}}_{\mathrm{m}}^{5}),\\ \hat{\vec{u}}_{\mathrm{m}}^{58} &= \hat{\vec{u}}_{\mathrm{m}}^{8} - \hat{\vec{u}}_{\mathrm{m}}^{5} = (\hat{\hat{\mathbf{F}}}_{\mathrm{M}} - \hat{\hat{\mathbf{I}}} + \zeta^{5}\hat{\hat{\mathbf{K}}}_{\mathrm{M}}) \cdot (\hat{\vec{X}}_{\mathrm{m}}^{8} - \hat{\vec{X}}_{\mathrm{m}}^{5}).\end{aligned} \tag{D.20}$$

When prescribing the control nodes as above, the tying equations provided in D.15 and D.16 can be written down in a more convenient way for implementation in a numerical environment as

$$\begin{aligned}\hat{\vec{u}}_{\mathrm{m}}^{R} &= \hat{\vec{u}}_{\mathrm{m}}^{L} + \frac{1}{2}(1-\eta)(\hat{\vec{u}}_{\mathrm{m}}^{2} - \hat{\vec{u}}_{\mathrm{m}}^{1}) + \frac{1}{2}(1+\eta)\hat{\vec{u}}_{\mathrm{m}}^{56},\\ \hat{\vec{u}}_{\mathrm{m}}^{T} &= \hat{\vec{u}}_{\mathrm{m}}^{B} + \frac{1}{2}(1-\eta)(\hat{\vec{u}}_{\mathrm{m}}^{4} - \hat{\vec{u}}_{\mathrm{m}}^{1}) + \frac{1}{2}(1+\eta)\hat{\vec{u}}_{\mathrm{m}}^{58},\end{aligned} \tag{D.21}$$

$$\begin{aligned}\tilde{\vec{u}}_{\mathrm{m}}^{R} &= \tilde{\vec{u}}_{\mathrm{m}}^{L} + \frac{1}{2}(1-\xi_2)(\tilde{\vec{u}}_{\mathrm{m}}^{2} - \tilde{\vec{u}}_{\mathrm{m}}^{1}) + \frac{1}{2}(1+\xi_2)(\tilde{\vec{u}}_{\mathrm{m}}^{3} - \tilde{\vec{u}}_{\mathrm{m}}^{4}),\\ \tilde{\vec{u}}_{\mathrm{m}}^{T} &= \tilde{\vec{u}}_{\mathrm{m}}^{B} + \frac{1}{2}(1-\xi_1)(\tilde{\vec{u}}_{\mathrm{m}}^{4} - \tilde{\vec{u}}_{\mathrm{m}}^{1}) + \frac{1}{2}(1+\xi_1)(\tilde{\vec{u}}_{\mathrm{m}}^{3} - \tilde{\vec{u}}_{\mathrm{m}}^{2}).\end{aligned} \tag{D.22}$$

Note that the equations use normalized coordinates $\eta = 2\zeta/H$ and $\xi_1, \xi_2 \in [-1, 1]$, which are the normalized coordinates in the $\vec{e}_1^c$ and $\vec{e}_2^c$ direction.

After running the simulation, the in-plane reaction forces $\hat{\vec{f}}_{\mathrm{m}}$ in the nodes and undeformed position vectors $\hat{\vec{X}}_{\mathrm{m}}$ can be used to calculate the macroscopic engineering stress resultant $\hat{\mathbf{N}}_{\mathrm{M}}$ and couple-stress resultant $\hat{\mathbf{M}}_{\mathrm{M}}$ as

$$\hat{\mathbf{N}}_{\mathrm{M}} = \frac{1}{A_{\mathrm{m}}} \sum_i \hat{\vec{f}}_{\mathrm{m}}^i \hat{\vec{X}}_{\mathrm{m}}^{i\star}, \tag{D.23}$$

$$\hat{\mathbf{M}}_{\mathrm{M}} = \frac{1}{A_{\mathrm{m}}} \sum_i \zeta^i \hat{\vec{f}}_{\mathrm{m}}^i \hat{\vec{X}}_{\mathrm{m}}^{i\star}, \tag{D.24}$$

$$\begin{aligned} \hat{\vec{X}}_{\mathrm{m}}^{i\star} &= \hat{\vec{X}}_{\mathrm{m}}^{i} - \hat{\vec{X}}_{\mathrm{m}}^{1}, \quad \text{for } i = 1, 2, 4, \\ \hat{\vec{X}}_{\mathrm{m}}^{i\star} &= \hat{\vec{X}}_{\mathrm{m}}^{6} - \hat{\vec{X}}_{\mathrm{m}}^{5}, \quad \text{for } i = \hat{56}, \\ \hat{\vec{X}}_{\mathrm{m}}^{i\star} &= \hat{\vec{X}}_{\mathrm{m}}^{8} - \hat{\vec{X}}_{\mathrm{m}}^{5}, \quad \text{for } i = \hat{58}, \end{aligned} \tag{D.25}$$

which can be derived from equation D.17 and D.18 respectively.

E Study on the application of curvature

As explained in section 2.3.1, bending can be applied using five in-plane displacements. To fully understand the framework and to investigate the limitations when applying larger curvatures, a thorough study is done on the homogeneous unit cell as depicted in Figure E.1.

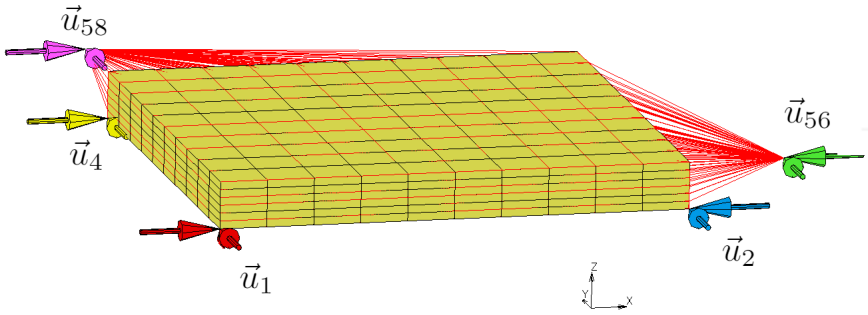

Figure E.1: The homogeneous unit cell that is used to investigate the framework. The boundary conditions to presribe the in-plane displacements are depicted by colored arrows. The servo link implementation of the tying equations is depicted by the red lines. Both in-plane dimensions are 10 mm, the out of plane height is 1 mm.

Pure bending in 2D

Pure bending is applied to the homogeneous unit cell to study the framework. To further simplify the problem, bending is first studied in 2D, using a plane strain assumption in the third direction. In 2D, only three in-plane deformations are prescribed, namely $\hat{\vec{u}}^1_{\mathrm{m}}$, $\hat{\vec{u}}^2_{\mathrm{m}}$ and $\hat{\vec{u}}^{56}_{\mathrm{m}}$. The neutral line is defined at half the height of the sheet. The curvature is applied such that the angle spanned by the neutral line is 30°. To satisfy the pure bending assumption, the length change of the neutral line should be 0. Geometric calculations are performed to calculate both the curvature and the deformation tensor that prescribe this pure bending. A schematic of the problem considered is depicted in Figure E.2.

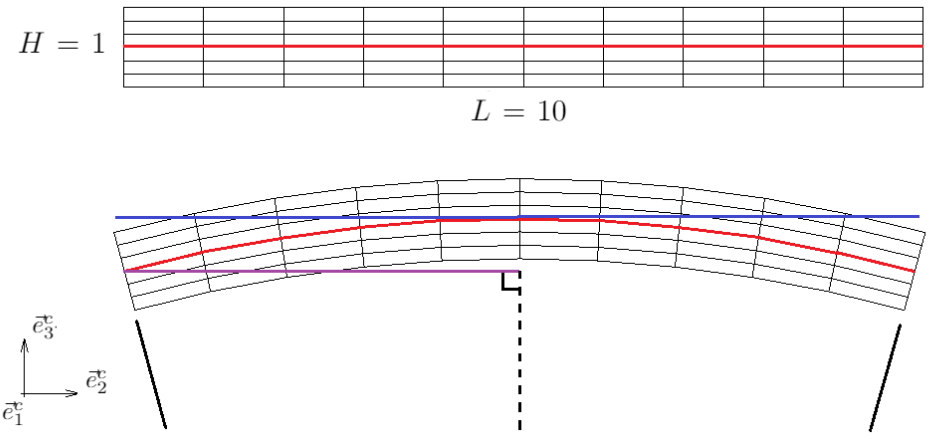

Figure E.2: Schematic representation of the bending problem considered. The neutral line is drawn in red. The ($\vec{e}^c_1$,$\vec{e}^c_2$)-plane defined tangent to the reference surface at the center is drawn in blue. Note that in the undeformed configuration, the ($\vec{e}^c_1$,$\vec{e}^c_2$)-plane coincides with the neutral line. In the deformed configuration, the projection of the neutral line on the ($\vec{e}^c_1$,$\vec{e}^c_2$)-plane is depicted in purple. The angle between the dashed line and the black line is half the total angle, 15°.

Since plane strain is assumed in the $\vec{e}^c_1$ direction, the only prescribed displacement is in the $\vec{e}^c_2$ direction.

Hence, both the deformation and curvature can be represented by a scalar. The curvature can be calculated as

$$r = \frac{L}{\theta} = \frac{10}{\frac{30}{360} \cdot 2\pi} = \frac{60}{\pi} = 19.10, \qquad \kappa = \frac{1}{r} = 0.0524. \tag{E.1}$$

The in-plane deformation is defined as the projection of the deformed configuration on the ($\vec{e}_1^c$,$\vec{e}_2^c$)-plane [10]. In other words, the projection of the red line in Figure E.2 on the blue line, depicted by the purple line. F is calculated as

$$\mathrm{F} = \frac{\text{length purple line}}{\text{length undeformed configuration}} = \frac{\sin 15 \cdot r}{5} = 0.9886. \tag{E.2}$$

Rigid body motion is fixed in the centre of the unit cell. Prescribing F and κ according to

$$\begin{aligned} \hat{\vec{u}}_{\mathrm{m}}^{i} &= (\hat{\mathbf{F}}_{\mathrm{M}} - \hat{\mathbf{I}} + \zeta^1 \hat{\mathbf{K}}_{\mathrm{M}}) \cdot \hat{\vec{X}}_{\mathrm{m}}^{i}, \qquad i = 1, 2, 4, \\ \hat{\vec{u}}_{\mathrm{m}}^{56} &= \hat{\vec{u}}_{\mathrm{m}}^{6} - \hat{\vec{u}}_{\mathrm{m}}^{5} = (\hat{\mathbf{F}}_{\mathrm{M}} - \hat{\mathbf{I}} + \zeta^5 \hat{\mathbf{K}}_{\mathrm{M}}) \cdot (\hat{\vec{X}}_{\mathrm{m}}^{6} - \hat{\vec{X}}_{\mathrm{m}}^{5}), \\ \hat{\vec{u}}_{\mathrm{m}}^{58} &= \hat{\vec{u}}_{\mathrm{m}}^{8} - \hat{\vec{u}}_{\mathrm{m}}^{5} = (\hat{\mathbf{F}}_{\mathrm{M}} - \hat{\mathbf{I}} + \zeta^5 \hat{\mathbf{K}}_{\mathrm{M}}) \cdot (\hat{\vec{X}}_{\mathrm{m}}^{8} - \hat{\vec{X}}_{\mathrm{m}}^{5}), \end{aligned} \tag{E.3}$$

results in the following values for $\hat{\vec{u}}_{\mathrm{m}}^{1}$, $\hat{\vec{u}}_{\mathrm{m}}^{2}$ and $\hat{\vec{u}}_{\mathrm{m}}^{56}$:

$$\hat{\vec{u}}_{\mathrm{m}}^{1} = 0.1878, \qquad \hat{\vec{u}}_{\mathrm{m}}^{2} = -0.1878, \qquad \hat{\vec{u}}_{\mathrm{m}}^{56} = 0.1480. \tag{E.4}$$

The resulting deformation is depicted in Figure E.3. The contours are plot in a cylindrical coordinate system with the origin at the centre of the radius of curvature $\{0,-\frac{60}{\pi}\}$. Plotting σ_{22} in MSC Marc/Mentat thus shows the stress in the local axial direction of the sheet, corresponding with $\sigma_{\theta\theta}$ in the radial coordinate system. This value should be positive for the upper side, 0 at the neutral line, and negative at the bottom side, which is indeed the case. It has to be noted that the stress is not exactly 0 at the neutral line, which might be caused by discretization or side effects. The stress value at the neutral line is about 1% of the highest stress value.

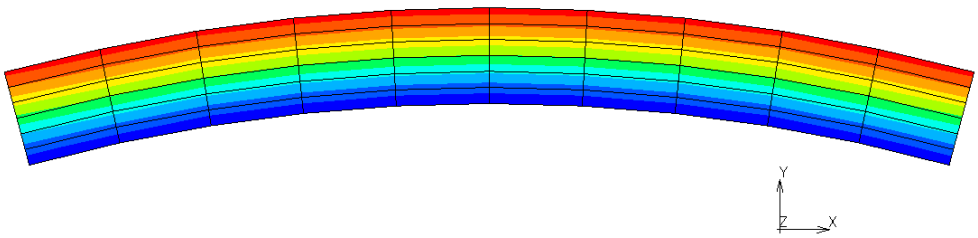

Figure E.3: The deformation when bending is applied to the 2D homogeneous sheet. The contours represent the $\sigma_{\theta\theta}$ stress field.

Following the framework, $\hat{\mathbf{M}}_{\mathrm{M}}$ and $\hat{\mathbf{N}}_{\mathrm{M}}$ can be calculated by using the reaction forces $\hat{\vec{f}}_{\mathrm{i}}$ and undeformed position vectors $\hat{\vec{X}}_{\mathrm{m}}$ as

$$\hat{\mathbf{N}}_{\mathrm{M}} = \frac{1}{A_{\mathrm{m}}} \sum_i \hat{\vec{f}}_{\mathrm{m}}^{i} \hat{\vec{X}}_{\mathrm{m}}^{i\star} = \frac{1}{100}(3166 \cdot -5 - 3166 \cdot 5 + 3070 \cdot 10) = -9.6 \text{ N/mm}, \tag{E.5}$$

$$\hat{\mathbf{M}}_{\mathrm{M}} = \frac{1}{A_{\mathrm{m}}} \sum_i \zeta^i \hat{\vec{f}}_{\mathrm{m}}^{i} \hat{\vec{X}}_{\mathrm{m}}^{i\star} = \frac{1}{100}(-\frac{1}{2} \cdot 3166 \cdot -5 - \frac{1}{2} \cdot -3166 \cdot 5 + \frac{1}{2} \cdot 3070 \cdot 10) = 312 \text{ N}. \tag{E.6}$$

The analytical solution for the reaction moment M can be calculated as

$$M = \frac{EI}{r} = \frac{70 \cdot 10^3 \cdot \frac{10}{12}}{19.10} = 3050 \text{ Nmm}. \tag{E.7}$$

The analytical solution should be divided by the unit cell size in the bending direction to compare the results with the couple-stress resultant. This results in $3050/10 = 305$ N, which closely matches the numerical result. Theoretically, the value found for $\hat{\hat{\mathbf{N}}}_{\mathrm{M}}$ should be 0 in a pure bending case. Since this is not the case, the beam might undergo a slightly different deformation. Simulations are performed on a range of bending angles $\alpha \in [5°, 120°]$ to investigate this side effect and the method's suitability for bending over larger angles. Further, the mesh is refined to a 100 by 12 grid using 2D quad elements to reduce discretization errors. The resulting couple-stress is provided in Figure E.4.

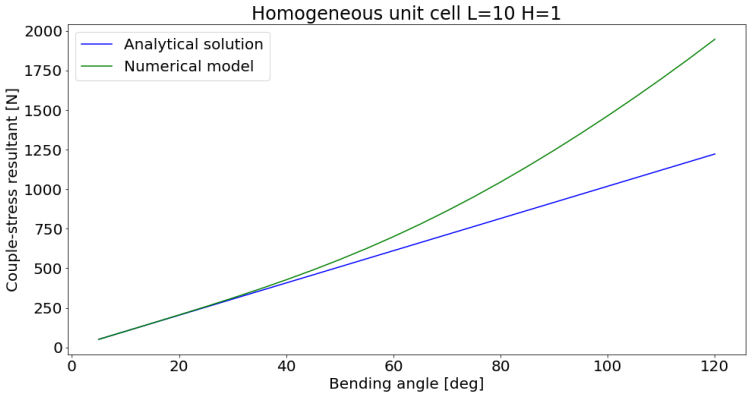

Figure E.4: The couple stress resultant $\hat{\hat{\mathbf{M}}}_{\mathrm{M}}$ for the 2D homogeneous bending case.

As can be observed, the the couple-stress resultant deviates more from the analytical solution for larger bending angles. The deformed mesh at a bending angle of 120° is depicted in Figure E.5.

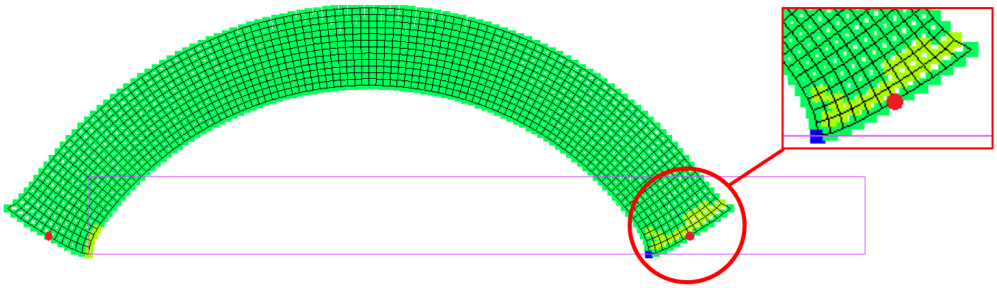

Figure E.5: The deformed mesh at the applied bending angle of 120°. The contour of the starting mesh is depicted in purple.

As can be observed from Figure E.5, the deformations near the corners of the sample are irregular. The root cause of this anomaly is that, in the applied displacements, the in-plane length change of the sample is neglected when applying the curvature. In other words, it is assumed that the horizontal distance between the red dots in Figure E.5 is not changing. As can be observed in the figure, this distance is undoubtedly shorter than in the undeformed sample. To take this into account in the boundary conditions, the equations

to apply the in-plane deformations $\hat{\vec{u}}^i_{\mathrm{m}}$ as stated in (E.3) are updated to

$$\begin{aligned}
\hat{\vec{u}}^i_{\mathrm{m}} &= (\hat{\hat{\mathbf{F}}}_{\mathrm{M}} - \hat{\hat{\mathbf{I}}} + \hat{\hat{\mathbf{F}}}_{\mathrm{M}}\zeta^1\hat{\hat{\mathbf{K}}}_{\mathrm{M}}) \cdot (\hat{\vec{X}}^i_{\mathrm{m}} - \hat{\vec{X}}^1_{\mathrm{m}}), \qquad i = 1, 2, 4, \\
\hat{\vec{u}}^{56}_{\mathrm{m}} &= \hat{\vec{u}}^6_{\mathrm{m}} - \hat{\vec{u}}^5_{\mathrm{m}} = (\hat{\hat{\mathbf{F}}}_{\mathrm{M}} - \hat{\hat{\mathbf{I}}} + \hat{\hat{\mathbf{F}}}_{\mathrm{M}}\zeta^5\hat{\hat{\mathbf{K}}}_{\mathrm{M}}) \cdot (\hat{\vec{X}}^6_{\mathrm{m}} - \hat{\vec{X}}^5_{\mathrm{m}}), \\
\hat{\vec{u}}^{58}_{\mathrm{m}} &= \hat{\vec{u}}^8_{\mathrm{m}} - \hat{\vec{u}}^5_{\mathrm{m}} = (\hat{\hat{\mathbf{F}}}_{\mathrm{M}} - \hat{\hat{\mathbf{I}}} + \hat{\hat{\mathbf{F}}}_{\mathrm{M}}\zeta^5\hat{\hat{\mathbf{K}}}_{\mathrm{M}}) \cdot (\hat{\vec{X}}^8_{\mathrm{m}} - \hat{\vec{X}}^5_{\mathrm{m}}),
\end{aligned} \tag{E.8}$$

with the updated part marked in blue. The deformed sample when using this updated formulation is depicted in Figure E.6.

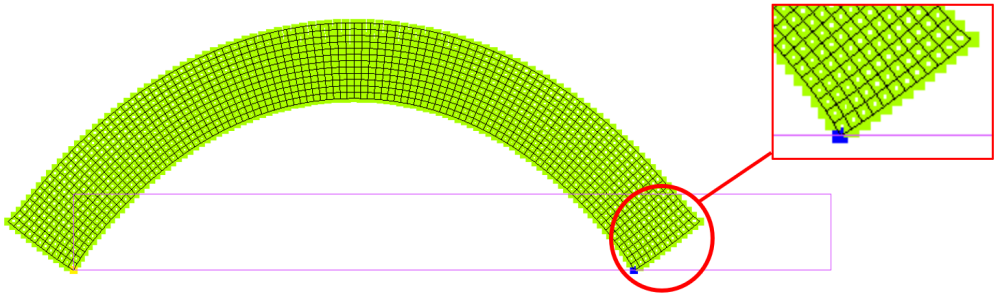

Figure E.6: Deformed sample using the updated displacement formulation. The applied bending angle is 120°.

As can be observed, the side effects are still present, but less significant than in the original formulation. It can be concluded that the updated formulation results in a more realistic deformation at the edges of the sample. The remaining effects are most likely present because the method only prescribes the deformation in $\vec{e}^c_2$ direction. The deformation in the out-of-plane direction $\vec{e}^c_3$ is left unconstrained to ensure plane stress in this direction. Apparently, it is a cheaper operation in terms of work performed to deform the end of the beam a bit in the out-of-plane direction, increasing its local thickness at the ends while doing so, than to perform a perfect bending operation. This also causes the stresses in the local $\varepsilon_{\mathrm{rr}}$ direction to be not perfectly axisymmetric, as shown in Figure E.3.

Using the updated displacements, the couple-stress resultant is calculated as depicted in Figure E.7a. The same is done for a homogeneous sample with half the thickness, as depicted in Figure E.7b, which shows even more improvement compared to the old formulation. A visual representation of the deformed sample with half the thickness is depicted in Figure E.8.

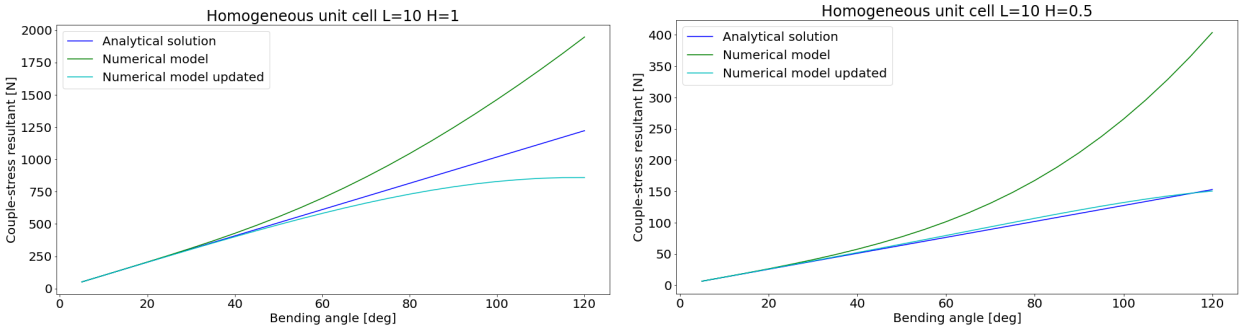

(a) (b)

Figure E.7: The couple stress resultant $\hat{\hat{\mathbf{M}}}_{\mathrm{M}}$ for the 2D homogeneous bending case using the updated formulation.

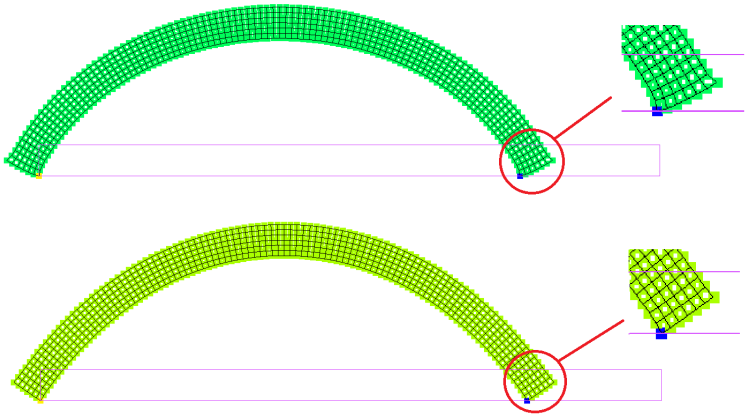

Figure E.8: The deformed mesh of a homogeneous unit cell with the applied bending angle of 120° using the original formulation (top), and the updated formulation (bottom).

The steps described above are repeated for the 3D unit cell. The mesh refinement for the 3D model was $20 * 20 * 6$ elements in length, width and height respectively. A visual representation of the bent unit cell is depicted in Figure E.9. The couple stress resultant of this simulation was exactly the same as for a $20 * 6$ 2D unit cell.

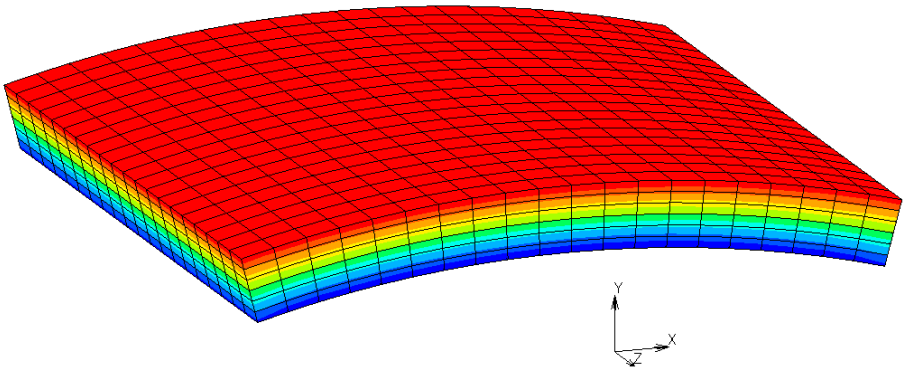

Figure E.9: The deformation of the 3D unit cell with an applied bending angle of 30°. The contours represent the $\sigma_{\theta\theta}$ stress field.

Periodicity microfluctuations

Besides investigating the couple-stress for the bending case, the microfluctuations at the edges are studied. Microfluctuations are created by adding a stiff inclusion in the unit cell, making it heterogeneous instead of homogeneous. A horizontal displacement is added to the unit cell in addition to the applied curvature of 30° to amplify the microfluctuations. The result is depicted in Figure E.10.

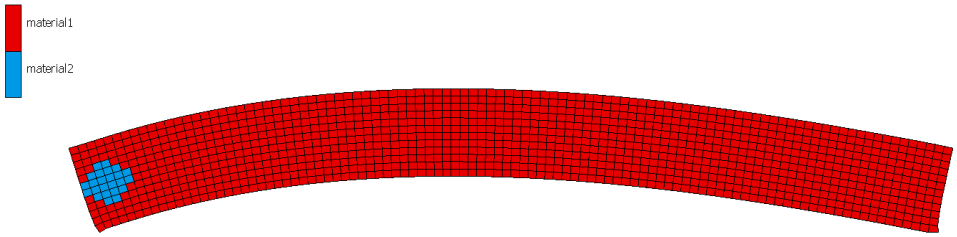

Figure E.10: The deformed sample with an applied bending angle of 30°. A stiff inclusion and an extra horizontal deformation are applied to amplify the microfluctuations.

As can be observed, the deformation seems to match the other side of the RVE. However, when measuring the displacements, it can be concluded that the mesh is not perfectly periodic. The is caused by the fact that the microfluctuations are coupled in a local Cartesian coordinate system, which is defined in the undeformed configuration. Since the locally defined coordinate system does not change with the applied curvature during the simulation, microfluctuations are not connected perfectly. A numerical implementation of changing local coordinate systems with each increment in MSC Marc/Mentat is challenging, if not impossible. The mismatch in periodicity becomes even clearer for bigger curvatures, as depicted in Figure E.11.

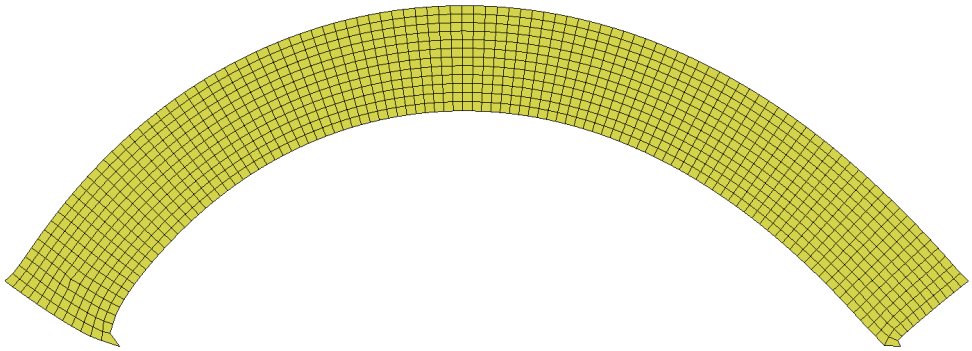

Figure E.11: The deformed sample using a 120° bending angle and a local stiff inclusion

In the literature, it is stated that the resulting deformation of the entire 3D RVE is, in general, not geometrically periodic due to macroscopic higher-order deformation modes (e.g. bending) [10]. Therefore, the mismatch in periodicity is not directly a problem to calculate the macroscopic properties accurately. However, it should be kept in mind when implementing the framework because it can lead to local stress concentrations in the numerical implementation.

Developments in bending load case

To investigate the application of curvature for a unit cell with brick periodicity, this type of periodicity is implemented on the homogeneous unit cell. A top view of this updated unit cell is depicted in Figure E.12b.

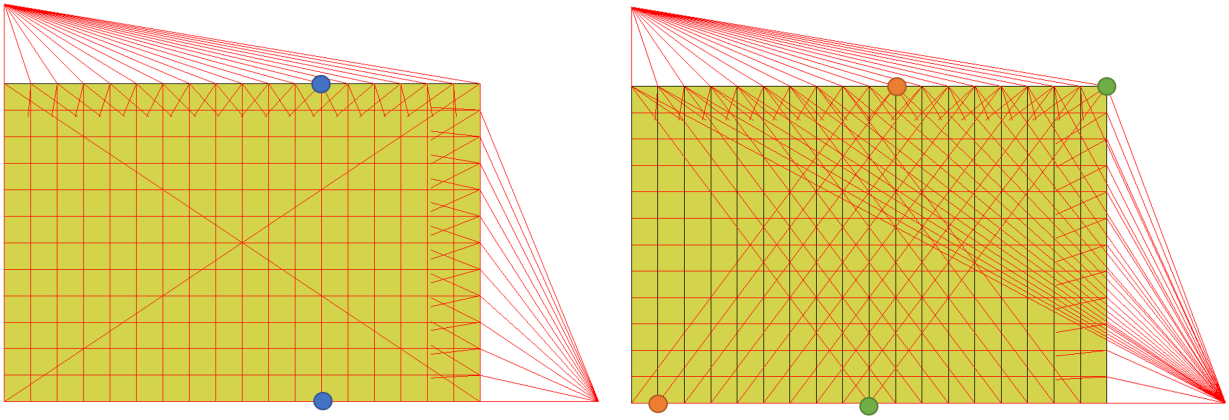

(a) (b)

Figure E.12: Top view of a homogeneous unit cell having regular periodicity (a) and brick periodicity (b). Examples of connected nodes are depicted by the colored circles.

Bending to an angle of 30° is applied to the unit cells, using the methodology described previously. The deformed unit cell, including a visual representation of connected nodes of both the regular and brick periodicity, is depicted in Figure E.13.

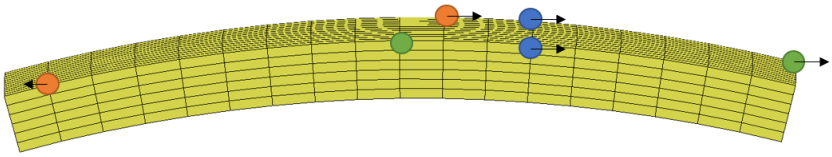

Figure E.13: The deformed homogeneous unit cell. The tied nodes in regular periodicity (blue) and brick periodicity (orange and green). The displacement of the nodes is depicted with the black arrows.

The natural in-plane displacement vectors in pure bending are equal for the connected nodes with regular periodicity, as depicted in blue. This is not the case for the connected nodes in the brick periodicity. In brick periodicity, for nodes located at the top surface, this difference is accounted for by the term $\frac{1}{2}\hat{\tilde{u}}^{56}_{\mathrm{m}}$ as stated in the tying equations in section 2.3.1. The problem is that, for bending, this term does not exactly represent the difference in displacement along the whole top surface. The only nodes at the top surface for which it holds that the difference in in-plane displacement is exactly equal to $\frac{1}{2}\hat{\tilde{u}}^{56}_{\mathrm{m}}$ are depicted in green. The fact that for the orange nodes it is a different value can be explained by the fact that $\sin(\alpha) \neq \sin(\frac{1}{9}\alpha) + \sin(\frac{8}{9}\alpha)$, where α is half the total bending angle, in this case 15°.

A method is developed which corrects for this difference, which improves the resulting macroscopic properties. The resulting couple-stress, using this improved method, is depicted by the orange line in Figure E.14. Using the original tying equations for brick periodicity results in the couple-stress depicted by the green line. The unit cell with regular periodicity is depicted in blue.

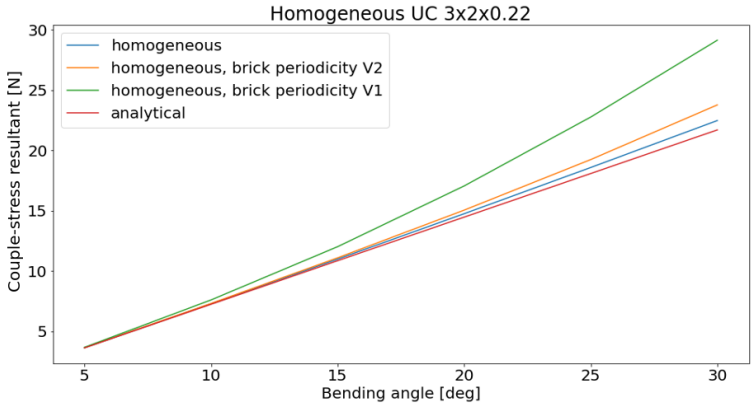

Figure E.14: The couple-stress resultant $\hat{\hat{\mathbf{M}}}_{\mathrm{M}}$ for a bending angle $\alpha \in [5, 30]$ deg.

This updated method requires knowing the applied curvature beforehand to prescribe a unique tying constraint for each set of connected nodes. The in-plane tying equation for the orange node is as in (E.9). A similar procedure can be repeated for the out-of-plane displacement, prescribing a calculated out-of-plane displacement between congruent nodes.

$$\hat{\hat{u}}^{T}_{\mathrm{m}} = \hat{\hat{u}}^{B}_{\mathrm{m}} + \hat{\hat{u}}^{58}_{\mathrm{m}} + 0.726\hat{\hat{u}}^{56}_{\mathrm{m}} \tag{E.9}$$

In this equation, the constant 0.726 is calculated based on the applied curvature and the position vectors of the orange nodes. This method of applying the tying equations requires more effort in model creation because each node pair requires a unique tying constraint. As can be observed in Figure E.14, this method is closer to the analytical solution and homogeneous solution with regular periodicity than the original tying equations. However, a perfect match with the regular periodicity result is not achieved, so side effects are still present. Since the reaction forces for bending in the stent unit cell are expected to be low, these side effects might have a significant influence on the result.

In addition to the brick periodicity, the parallelepiped shape of the stent unit cell complicates the application of bending as well. The resulting couple-stress is depicted in Figure E.15.

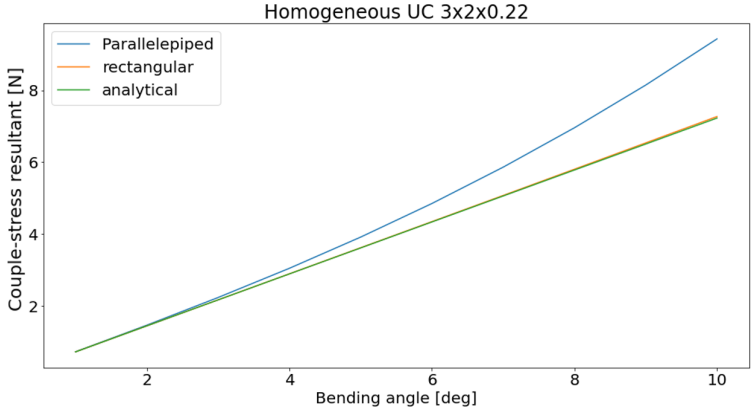

Figure E.15: The couple-stress resultant $\hat{\hat{\mathbf{M}}}_{\mathrm{M}}$ for a homogeneous parallelepiped unit cell with regular periodicity.

As can be observed, the couple-stress resultant of the parallelepiped model does not match the one of the rectangular-shaped unit cell. Even for small angles between 1 and 10 degrees, the error is significant. When brick periodicity is implemented for this model, the difference will be even higher. The root cause of the

error is comparable with what has been shown for the brick periodicity. In the parallelepiped model, the distance to the bending axis is not equal for all nodes. In the deformed configuration, the green nodes in Figure E.16a have a different distance to the bending axis than the orange nodes. In other words, the tying equations should be specific for each congruent node pair, as is the case for the brick periodicity.

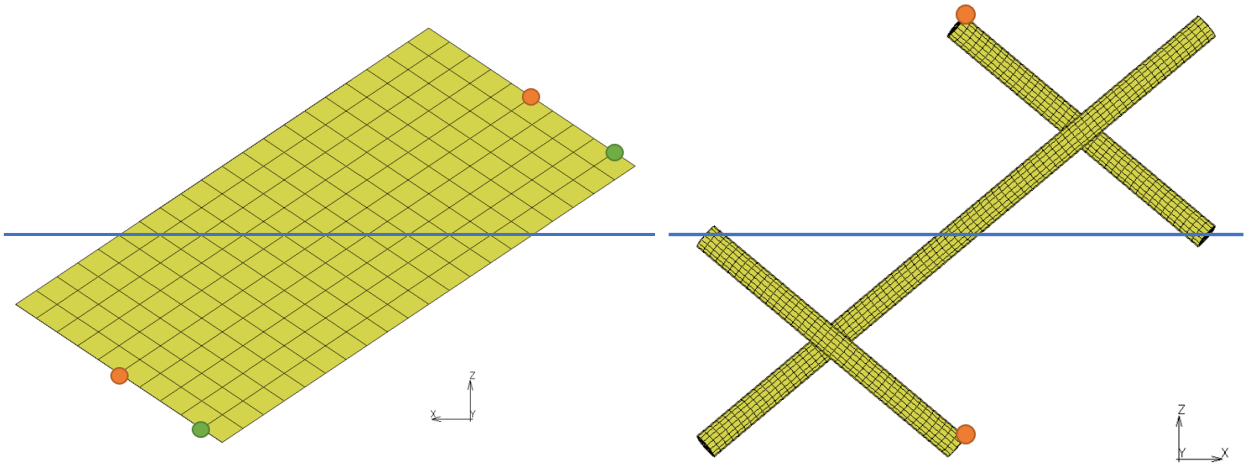

(a) (b)

Figure E.16: Top view of the homogeneous parallelepiped unit cell (a) and the stent unit cell (b). In both figures, the bending axis is depicted in blue. Examples of congruent node pairs are depicted by the colored circles.

Since the stent unit cell contains a lot of empty space and the material is concentrated around the wires centerlines, the difference in distance to the bending axis will be less. For this reason, the side effects are expected to be less severe, as shown by the blue line in Figure E.15. However, even minor side effects might significantly affect the final solution.

F Derivation of tying equations

First-order tying equations

Since the shape of the stent unit cell is not trivial, the implementation should be treated carefully. First-order periodic boundary conditions are used as the starting point for the derivation of the tying equations:

$$\begin{aligned} \vec{x}_{\mathrm{T}} &= \vec{x}_{\mathrm{B}} + \vec{x}_4 - \vec{x}_1, \\ \vec{x}_{\mathrm{R}} &= \vec{x}_{\mathrm{L}} + \vec{x}_2 - \vec{x}_1. \end{aligned} \tag{F.1}$$

These tying equations can can be rewritten in terms of displacements as

$$\begin{aligned} \vec{u}_{\mathrm{T}} &= \vec{u}_{\mathrm{B}} + \vec{u}_4 - \vec{u}_1, \\ \vec{u}_{\mathrm{R}} &= \vec{u}_{\mathrm{L}} + \vec{u}_2 - \vec{u}_1. \end{aligned} \tag{F.2}$$

These tying equations are suitable for a 2D, rectangular-shaped RVE. When looking at the top view of the stent unit cell in Figure F.1a, the shape is a parallelogram.

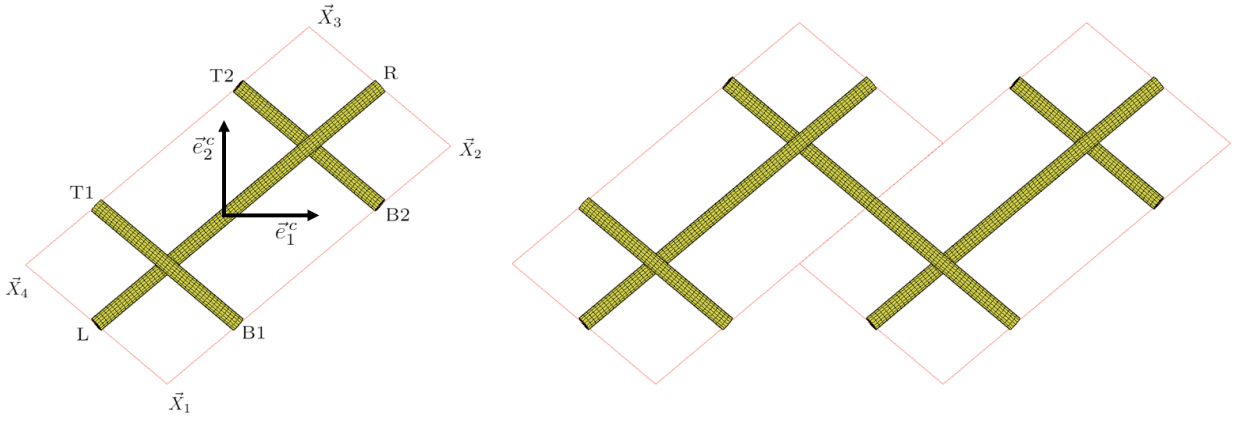

(a) (b)

Figure F.1: Top view of the defined unit cell, including the position vectors $\vec{X}_1$ till $\vec{X}_4$, and local coordinate system $\{\vec{e}_1^c, \vec{e}_2^c, \vec{e}_3^c\}$ (left). Two adjacent stent unit cells (right).

Since no displacements are applied in out-of-plane direction because of the thin shell assumption at the macroscale, three control nodes at $\vec{X}_1$, $\vec{X}_2$ and $\vec{X}_4$ are sufficient to apply the first-order macroscopic generalized strains. When looking at the wire ends denoted by 'R' and 'L', the distance between these nodes is still equal to $\vec{x}_2 - \vec{x}_1$, as is the case for a rectangular RVE. Likewise, the distance between 'T1' and 'B1' is still equal to $\vec{x}_4 - \vec{x}_1$. Equations (F.1) and (F.2) still hold, thus these equations can be used for a parallelogram shape as well. However, what should be taken into account is that 'T1' should be connected to 'B2' instead of 'B1', as depicted in Figure F.1b. Correspondingly, 'T2' should be connected to 'B1'. This is referred to as 'brick periodicity'. This results in

$$\begin{aligned} \vec{u}_{\mathrm{T1}} &= \vec{u}_{\mathrm{B2}} + \vec{u}_4 - \vec{u}_1 - \frac{1}{2}(\vec{u}_2 - \vec{u}_1), \\ \vec{u}_{\mathrm{T2}} &= \vec{u}_{\mathrm{B1}} + \vec{u}_4 - \vec{u}_1 + \frac{1}{2}(\vec{u}_2 - \vec{u}_1), \\ \vec{u}_{\mathrm{R}} &= \vec{u}_{\mathrm{L}} \quad + \vec{u}_2 - \vec{u}_1. \end{aligned} \tag{F.3}$$

The distance between $\vec{x}_{\mathrm{T1}}$ and $\vec{x}_{\mathrm{B2}}$ along the $(\vec{x}_2 - \vec{x}_1)$-direction is described by $-\frac{1}{2}(\vec{x}_2 - \vec{x}_1)$. In terms of displacement vectors, this can be rewritten as $-\frac{1}{2}(\vec{u}_2 - \vec{u}_1)$, and can be implemented in the tying equation.

For $\vec{x}_{\mathrm{T2}}$ and $\vec{x}_{\mathrm{B1}}$, the distance is described as $\frac{1}{2}(\vec{x}_2 - \vec{x}_1)$. When expressed in displacements, this results in $\frac{1}{2}(\vec{u}_2 - \vec{u}_1)$.

Second-order tying equations

With the tying equations provided in (F.3), all first-order deformations can be applied. The equations become challenging when applying curvature, which is of second-order type. The framework developed by Coenen et al. is used as a starting point [10]. In this framework, the deformations of the RVE are split into an in-plane and an out-of-plane component, denoted by a superimposed $\hat{}$ and $\tilde{}$ respectively. The tying equations for a rectangular-shaped RVE are defined as

$$\begin{aligned}\hat{\vec{u}}^T_{\mathrm{m}} &= \hat{\vec{u}}^B_{\mathrm{m}} + \frac{1}{2}(1-\eta)(\hat{\vec{u}}^4_{\mathrm{m}} - \hat{\vec{u}}^1_{\mathrm{m}}) + \frac{1}{2}(1+\eta)\hat{\vec{u}}^{58}_{\mathrm{m}},\\ \hat{\vec{u}}^R_{\mathrm{m}} &= \hat{\vec{u}}^L_{\mathrm{m}} + \frac{1}{2}(1-\eta)(\hat{\vec{u}}^2_{\mathrm{m}} - \hat{\vec{u}}^1_{\mathrm{m}}) + \frac{1}{2}(1+\eta)\hat{\vec{u}}^{56}_{\mathrm{m}},\end{aligned} \tag{F.4}$$

$$\begin{aligned}\tilde{\vec{u}}^T_{\mathrm{m}} &= \tilde{\vec{u}}^B_{\mathrm{m}} + \frac{1}{2}(1-\xi_1)(\tilde{\vec{u}}^4_{\mathrm{m}} - \tilde{\vec{u}}^1_{\mathrm{m}}) + \frac{1}{2}(1+\xi_1)(\tilde{\vec{u}}^3_{\mathrm{m}} - \tilde{\vec{u}}^2_{\mathrm{m}}),\\ \tilde{\vec{u}}^R_{\mathrm{m}} &= \tilde{\vec{u}}^L_{\mathrm{m}} + \frac{1}{2}(1-\xi_2)(\tilde{\vec{u}}^2_{\mathrm{m}} - \tilde{\vec{u}}^1_{\mathrm{m}}) + \frac{1}{2}(1+\xi_2)(\tilde{\vec{u}}^3_{\mathrm{m}} - \tilde{\vec{u}}^4_{\mathrm{m}}).\end{aligned} \tag{F.5}$$

In these equations, ξ_1, ξ_2 and η are the normalized coordinates in $\vec{e}^c_1, \vec{e}^c_2$ and $\vec{e}^c_3$ respectively, having a value between -1 and 1. Note that in (F.5), the terms apart from $\tilde{\vec{u}}^T_{\mathrm{m}}$, $\tilde{\vec{u}}^B_{\mathrm{m}}$, $\tilde{\vec{u}}^R_{\mathrm{m}}$ and $\tilde{\vec{u}}^L_{\mathrm{m}}$ are only relevant when the out-of-plane displacements in corner nodes 1, 2, 3, and 4 are not equal. Since the RVE is constrained in the center, this is only the case for twisting. In the case of pure bending, the out-of-plane displacements in the corners are equal, and all terms vanish from the equation, resulting in

$$\begin{aligned}\tilde{\vec{u}}^T_{\mathrm{m}} &= \tilde{\vec{u}}^B_{\mathrm{m}},\\ \tilde{\vec{u}}^R_{\mathrm{m}} &= \tilde{\vec{u}}^L_{\mathrm{m}}.\end{aligned} \tag{F.6}$$

Following the same reasoning as for the first-order equations, the in-plane equations also hold for a parallelepiped shaped RVE. To include the brick periodicity, the term that should be added depends on the normalized out-of-plane coordinate η. When $\eta = 1$, $\frac{1}{2}\hat{\vec{u}}^{56}_{\mathrm{m}}$ should be added when tying T2 to B1. When $\eta = -1$, it should be $\frac{1}{2}(\vec{u}_2 - \vec{u}_1)$. In-between, a combination of both components is applied, which depends linearly on η. Taking this into account, the updated expressions are

$$\begin{aligned}\hat{\vec{u}}^{T1}_{\mathrm{m}} &= \hat{\vec{u}}^{B2}_{\mathrm{m}} + (1-\eta)(\frac{1}{2}\hat{\vec{u}}^4_{\mathrm{m}} - \frac{1}{4}\hat{\vec{u}}^2_{\mathrm{m}} - \frac{1}{4}\hat{\vec{u}}^1_{\mathrm{m}}) + (1+\eta)(\frac{1}{2}\hat{\vec{u}}^{58}_{\mathrm{m}} - \frac{1}{4}\hat{\vec{u}}^{56}_{\mathrm{m}}),\\ \hat{\vec{u}}^{T2}_{\mathrm{m}} &= \hat{\vec{u}}^{B1}_{\mathrm{m}} + (1-\eta)(\frac{1}{2}\hat{\vec{u}}^4_{\mathrm{m}} + \frac{1}{4}\hat{\vec{u}}^2_{\mathrm{m}} + \frac{3}{4}\hat{\vec{u}}^1_{\mathrm{m}}) + (1+\eta)(\frac{1}{2}\hat{\vec{u}}^{58}_{\mathrm{m}} - \frac{1}{4}\hat{\vec{u}}^{56}_{\mathrm{m}}),\\ \hat{\vec{u}}^R_{\mathrm{m}} &= \hat{\vec{u}}^L_{\mathrm{m}} + \frac{1}{2}(1-\eta)(\hat{\vec{u}}^2_{\mathrm{m}} - \hat{\vec{u}}^1_{\mathrm{m}}) + \frac{1}{2}(1+\eta)\hat{\vec{u}}^{56}_{\mathrm{m}}.\end{aligned} \tag{F.7}$$

Following the reasoning leading to (F.6), and based on studies done on the bending load case as described in Appendix E, simplified assumptions are made or the out-of-plane component. The simplified out-of-plane tying equations are

$$\begin{aligned}\tilde{\vec{u}}^{T1}_{\mathrm{m}} &= \tilde{\vec{u}}^{B2}_{\mathrm{m}},\\ \tilde{\vec{u}}^{T2}_{\mathrm{m}} &= \tilde{\vec{u}}^{B1}_{\mathrm{m}},\\ \tilde{\vec{u}}^R_{\mathrm{m}} &= \tilde{\vec{u}}^L_{\mathrm{m}}.\end{aligned} \tag{F.8}$$